GDAŃSK UNIVERSITY OF TECHNOLOGY

The author of the doctoral dissertation: Worku Firomsa Kabeta
Scientific discipline: Civil Engineering, Geodesy and Transport

DOCTORAL DISSERTATION

Title of doctoral dissertation: Centrifuge Modelling of Tapered Pile Installation Effects in Sand

Title of doctoral dissertation (in Polish): Efekty instalacji w piasku pali zwężających się z głębokością na podstawie badań w wirówce geotechnicznej

Supervisor *signature*
prof. dr hab. inż. Lech Bałachowski
Auxiliary supervisor *signature*
dr inż. Jakub Konkol

Gdańsk, 2025

POLITECHNIKA GDAŃSKA

STATEMENT

The author of the doctoral dissertation: Worku Firomsa Kabeta

I, the undersigned, declare that I am aware that in accordance with the provisions of Art. 27 (1) and (2) of the Act of 4th February 1994 on Copyright and Related Rights (Journal of Laws of 2021, item 1062), the university may use my doctoral dissertation entitled: *Centrifuge Modelling of Tapered Pile Installation Effects in Sand*, for scientific or didactic purposes.[1]

Gdańsk,..... .....

signature of the PhD student

Aware of criminal liability for violations of the Act of 4th February 1994 on Copyright and Related Rights and disciplinary actions set out in the Law on Higher Education and Science(Journal of Laws 2021, item 478), as well as civil liability, I declare, that the submitted doctoral dissertation is my own work.

I declare, that the submitted doctoral dissertation is my own work performed under and in cooperation with the supervision of prof. dr hab. inż. Lech Bałachowski and the auxiliary supervision of dr inż. Jakub Konkol.

This submitted doctoral dissertation has never before been the basis of an official procedure associated with the awarding of a PhD degree.

All the information contained in the above thesis which is derived from written and electronic sources is documented in a list of relevant literature in accordance with Art. 34 of the Copyright and Related Rights Act.

I confirm that this doctoral dissertation is identical to the attached electronic version.

Gdańsk,..... .....

signature of the PhD student

I, the undersigned, agree/~~do not agree~~* to include an electronic version of the above doctoral dissertation in the open, institutional, digital repository of Gdańsk University of Technology.

Gdańsk,..... .....

signature of the PhD student

**delete where appropriate*

[1] Art 27. 1. Educational institutions and entities referred to in art. 7 sec. 1 points 1, 2 and 4–8 of the Act of 20 July 2018 – Law on Higher Education and Science, may use the disseminated works in the original and in translation for the purposes of illustrating the content provided for didactic purposes or in order to conduct research activities, and to reproduce for this purpose disseminated minor works or fragments of larger works.

2. If the works are made available to the public in such a way that everyone can have access to them at the place and time selected by them, as referred to in para. 1, is allowed only for a limited group of people learning, teaching or conducting research, identified by the entities listed in paragraph 1.

GDAŃSK UNIVERSITY OF TECHNOLOGY

DESCRIPTION OF DOCTORAL DISSERTATION

The Author of the doctoral dissertation: Worku Firomsa Kabeta

Title of doctoral dissertation: Centrifuge Modelling of Tapered Pile Installation Effects in Sand

Title of doctoral dissertation in Polish: Efekty instalacji w piasku pali zwężających się z głębokością na podstawie badań w wirówce geotechnicznej

Language of doctoral dissertation: English

Supervisor: prof. dr hab. inż. Lech Bałachowski

Auxiliary supervisor*: dr inż. Jakub Konkol

Date of doctoral defense: <day, month, year>

Keywords of doctoral dissertation in Polish: Badania modelowe, wirówka geotechniczna, efekty instalacji pala, mobilizacja naprężeń, przemieszczenia gruntu

Keywords of doctoral dissertation in English: Centrifuge modeling, Tapered pile, Installation effects, Stress mobilization, Soil displacement

Summary of doctoral dissertation in Polish: Analiza wpływu instalacji w piasku pali zwężających się z głębokością na podstawie wyników badań modelowych w wirówce geotechnicznej w płaskim stanie odkształcenia. Badania wykonano w zagęszczonym piasku Fontainebleau przy przyśpieszeniu 25g wykorzystując trzy modele ścian: prosty i dwa trapezoidalne o kącie nachylenia powierzchni bocznej 0.75° and 1.5°. Modele wciskano z powierzchni gruntu z prędkością 0.1mm/s do głębokości 224mm mierząc siłę pionową na głowicy. Czujniki rejestrowały zmiany naprężeń poziomych w gruncie oraz naprężeń kontaktowych na powierzchni bocznej ściany. Analiza obrazu metodą PIV pozwoliła na wyznaczenie pól przemieszczeń I odkształceń.
Instalacja pali zwężających się z głębokością wywołuje wyższy poziom składowej poziomej naprężenia w gruncie i składowej normalnej naprężenia kontaktowego w prównaniu do ściany prostej. Zaobserwowano re-mobilizację naprężeń w gruncie w przypadku ściany zwężającej się z głębokością i rosnącą wraz z nachyleniem powierzchni ściany. Analizy metodą PIV ujawniły większy zasięg oddziaływania ściany o powierzchni nachylonej, przy większych przemieszczeniach poziomych w strefie przypowierzchniowej i mniejszych w sąsiedztwie podstawy. Analizy numeryczne pokazały mechanizm zniszczenia. Wyniki analiz MES potwierdziły istotne znaczenie wpływu instalacji ściany na jej nośność. Wyniki potwierdziły istotny wpływ geometrii ściany na jej nośność.

Summary of doctoral dissertation in English: This study investigates the behavior of tapered piles during installation and subsequent loading using centrifuge modeling in plane-strain conditions. Centrifuge tests were conducted at 25g using three model walls, a straight wall, and two tapered walls with 0.75° and 1.5° taper angles installed in dense Fontainebleau sand. The models were pushed into the sand at 0.1 mm/s to a depth of 224 mm. The load cell at the model wall head recorded the total axial force. Stress sensors measured horizontal and interface stresses, while Particle Image Velocimetry (PIV) tracked soil displacements and strain fields.
Tapered piles induced higher horizontal stress in the soil and greater normal stress along the shaft compared to the straight pile. Stress re-mobilization was observed in tapered models after wall passes sensor level, varying with taper angle. PIV revealed that the installation of tapered piles affected a larger soil zone, with greater horizontal displacement near the surface and reduced displacement at the base. Numerical analysis using the Finite Element Method and Limit Analysis assessed load-displacement behavior and failure mechanisms. FEM underestimated experimental values due to the exclusion of installation effects. Results show the significant influence of taper geometry on pile behavior and emphasize the need to account for installation effects in design.

Acknowledgments

First and foremost, I would like to thank God Almighty for granting me the strength, patience, and perseverance to complete this PhD journey. His grace and guidance have sustained me through every challenge.

I would also like to express my deepest gratitude to my supervisor, prof. dr hab. inż. Lech Bałachowski, for his continuous guidance, encouragement, and support throughout this journey. His insights and expertise have been invaluable to the development of this dissertation. I sincerely thank my auxiliary supervisor, dr inż. Jakub Konkol, for his valuable advice, feedback, and support during the progression of this research. His contributions greatly helped shape the direction and quality of this work.

My sincere thanks also go to all the staff members of the Department of Geotechnical and Hydraulic Engineering at Gdańsk University of Technology for their support and cooperation. I am especially grateful to the staff of the Geotechnical Centrifuge Laboratory at Gustave Eiffel University and to the GEOLAB EU–Horizon 2020 project, whose facilities and support enabled me to carry out essential parts of this research.

Finally, I would like to express my heartfelt gratitude to my family for their unwavering love, patience, and encouragement, which gave me the strength to pursue my dreams. In particular, I am deeply thankful to my beloved wife, Hinsene Lemma, and my precious child, Wedu Worku, whose constant support and understanding have been a continuous source of strength and inspiration throughout this journey.

I also wish to thank my colleagues, lab mates, and friends for their stimulating conversations, laughter, and emotional support during both the rewarding and challenging moments of this PhD.

Abstract

The growing demand for efficient and sustainable infrastructure has increased interest in optimizing deep foundation systems, particularly pile foundations. This study investigates the behavior of tapered piles during installation and subsequent loading using centrifuge modeling in plane-strain conditions. A series of centrifuge tests at 25g were conducted at the GERS-CG centrifuge facility (Gustave Eiffel University, France) using model walls (representing 2D plane strain model piles) installed in dense Fontainebleau sand (NE34). Three wall models, a straight wall and two tapered walls with 0.75° and 1.5° taper angles, were tested in a transparent container under plane-strain conditions. All models had the same volume, with an average breadth of 16 mm and a width-to-breadth ratio of 12.5. They were installed by continuous pushing at 0.1 mm/s to a final embedment of 224 mm, corresponding to a slenderness ratio of 14. The load cell at the model wall head recorded the total axial force during installation, followed by static loading. Stress mobilized in the soil during installation and static loading was measured using five stress sensors placed at different depths and distances from the walls. In addition, three stress sensors were attached to the model wall to measure soil–wall contact stress during installation and subsequent loading.

The evolution of horizontal stress in the soil mass and normal stress on the wall surface were measured during monotonic installation and subsequent static compression loading. Installation in sand induced additional horizontal stress in the surrounding soil and increased normal stress at the wall–soil interface. The maximum horizontal stress in the soil mass occurred just before the wall base passed the sensor level, typically near a depth of one wall breadth (1B) above the sensing point. For the straight wall, a continuous decrease in horizontal stress was recorded after the wall base passed the sensor level. In contrast, the tapered walls exhibited re-mobilization of horizontal stress, with the extent of re-mobilization dependent on

the taper angle. They also induce higher normal stress at the pile shaft and higher horizontal stress in the soil mass.

Particle Image Velocimetry (PIV) was employed to analyze soil displacements and strain fields at different embedment depths. Both horizontal and vertical displacement contours, as well as volumetric and shear strain fields, were examined around the penetrating walls. PIV analysis revealed distinct displacement and strain contour patterns depending on wall type and penetration depth. The soil zone affected by installation was significantly larger for tapered walls than for the straight wall. Horizontal displacements near the ground surface are higher for tapered walls compared to straight ones. However, near the model base, horizontal displacements were significantly reduced for tapered walls.

The behavior of bored tapered wall models was investigated numerically using the Finite Element Method (FEM) and Limit Analysis. FEM was used to evaluate the load-displacement behavior, while Limit Analysis was employed to estimate the failure loads and mechanisms for each model. Numerical analysis of the load-displacement behavior and failure mechanisms of model walls showed the significant influence of taper geometry on bearing capacity. Numerical predictions underestimated experimental results and are due to the exclusion of installation effects in the models. The installation effects concerning the shaft and the base of the wall were estimated. These installation effects increase with taper angle. Although the analysis was conducted under plane-strain conditions, the results can be qualitatively extended to monotonically installed tapered piles.

Table of contents

List of tables

List of figures

List of abbreviations

CPT	Cone penetration test
FRP	Fibre-reinforced polymer
ICP	Imperial College Pile
NE34	Fontainebleau sand
S	Straight wall with 0.00^0 taper angle
SLT	Static Loading Test
T1	Tapered wall with 0.75^0 taper angle
T2	Tapered wall with 1.50^0 taper angle

List of symbols

d	Distance from the wall axis
d_{50}	A cumulative 50% point of diameter
D_r	Relative density
e_{max}	Maximum void ratio
e_{min}	Minimum void ratio
e_0	Void ratio after spin-up
f_s	Unit shaft friction
h	Vertical distance from the wall base
K	Lateral earth pressure coefficient
K_0	At rest lateral earth pressure coefficient
q_c	Cone resistance
B	Wall breadth
D	Pile diameter
Q	Total bearing capacity
Q_b	Base resistance
Q_S	Shaft resistance
q_b	Unit base resistance
q_S	Unit shaft resistance
β	Shaft friction coefficient
δ	Interface friction angle
γ_d	Dry unit weight
ϕ	Angle of internal friction
ϕ'_{cv}	Constant volume effective friction angle
σ'_{h0}	Initial horizontal stress
σ'_n	Normal stress
$\sigma'_{n\ moving}$	Normal stress during wall penetration
$\sigma'_{n,stationary}$	Normal stress during wall penetration pause
$\sigma'_{n,SLT}$	Normal stress during SLT
σ'_{v0}	Initial vertical effective stress

CHAPTER ONE

1. Introduction

1.1 Background of the study

Pile foundations are essential in civil engineering to provide stability and support for structures such as buildings, bridges, and offshore platforms. They transfer structural loads to the underlying soil (Baziar et al., 2018; Carswell et al., 2015). The performance of these pile foundations depends on several conditions, including soil type (Peiffer et al., 1993; Xiao & Zhao, 2019), loading conditions (Bekki et al., 2024; Lee & Do, 2021), and installation methods (Paik & Salgado, 2004).

Pile installation often induces significant soil disturbances, altering soil structure and properties such as density, shear strength, and pore water pressure (Li et al., 2022; Shublaq, 1992). This disturbance significantly impacts pile behavior, including bearing capacity. The extent of soil disturbance depends on pile shape, size, installation method, and soil properties (Randolph et al., 1979).

Tapered piles have a cross-section that gradually decreases from top to bottom. The concept was first introduced by Rybnikov (1990). It was further developed through analytical and experimental studies by Kodikara and Moore (1993) and later by El Naggar and Wei (1999), whose model tests provided key insights into their axial performance. These and subsequent studies (Fahmy & El Naggar, 2017; Naggar & Sakr, 2000) confirmed that tapered piles offer enhanced load-bearing capacity while reducing material usage compared to cylindrical piles with constant cross-sections. Tapered piles can also be used as compaction piles to densify loose sandy soils and improve ground performance (Robinsky & Morrison, 1964). During installation, the tapered geometry induces significant radial displacement of the surrounding

soil, which increases relative density (Zil'berberg & Sherstnev, 1990; Kabeta, 2023). This makes tapered piles effective in improving bearing capacity and reducing settlement (Paik et al., 2013; Shabanpour & Ghazavi, 2022). However, their practical application remains limited due to a lack of detailed understanding about behavior during installation and under static loading conditions.

To address this knowledge gap, this research investigates the installation effects of tapered piles with varying taper angles using rigorous physical modelling with centrifuge and numerical approaches. Centrifuge testing replicates in-situ stress conditions at a reduced scale to analyze soil-pile interactions under realistic conditions (Schofield, 1980). The experiments presented in this thesis were conducted at Gustave Eiffel University (France) as part of the EU GeoLab project (grant agreement No. 101006512).

1.2 Motivation of the study

The increasing demand for more efficient and sustainable infrastructure has driven interest in optimizing foundation systems, particularly pile foundations. Tapered piles provide an alternative solution in onshore and offshore construction due to their enhanced load-bearing capacity and reduced material requirements (El Naggar & Wei, 1999; Naggar & Sakr, 2000; Horvath & Trochalides, 2004; Suits et al., 2011; Tavasoli & Ghazavi, 2020; Shafaghat & Khabbaz, 2022). Despite these advantages, their application in practice remains limited due to the lack of a comprehensive understanding of their behavior during installation and under static loading. Current design practices are predominantly based on cylindrical pile behavior, which prevents engineers from fully utilizing the benefits of tapered piles (Manandhar & Yasufuku, 2012; Nasrollahzadeh & Hataf, 2022). Moreover, installation-induced soil disturbances such as changes in stress state, density, and deformation significantly influence the load-displacement response of piles (Anusic et al., 2019; Haque et al., 2016; Shublaq, 1992). These

effects are complex in tapered piles due to their varying geometry (Cao et al., 2015; Paik & Salgado, 2004).

1.3 Objectives of the study

This research aimed to investigate the behavior of tapered piles during installation and loading in plane-strain conditions using centrifuge modeling. Tapered walls, also called plane strain piles, are considered in this study. The research aims to improve the understanding of soil-pile interaction for tapered piles and provide valuable insights for improving foundation design.

The following specific objectives were addressed to achieve this general objective.

1. To develop physical models for simulating the behavior of tapered piles in dense sand under plane-strain conditions.
2. To investigate the effects of taper angle on the load-displacement behavior and bearing capacity of piles installed in dense sand.
3. To analyze stress redistribution and mobilization around tapered piles during installation and subsequent static loading.
4. To evaluate soil deformation and strain patterns during pile installation using Particle Image Velocimetry (PIV).
5. To perform numerical simulations to validate and complement experimental observations.

1.4 Scope of the study

This research mainly investigates the effects and load-bearing behavior of tapered walls installed in sand using centrifuge modeling. The scope is limited to the controlled modeling of pile–soil interaction under plane strain conditions to analyze stress redistribution and deformation mechanisms associated with pile installation. The study considers the behavior of displacement piles in dense sand during continuous installation and under axial vertical loading in drained conditions.

The physical modeling was conducted at the GERS-CG centrifuge facility at Gustave Eiffel University (Nantes, France), using dense Fontainebleau sand (NE34). One straight model wall and two trapezoidal walls with taper angles of 0.75° and 1.5° were used to evaluate the influence of geometry on installation-induced soil response. The piles were scaled at a 1:25 ratio and tested in a transparent-sided container. Plane strain piles were installed by continuous pushing at a constant rate, followed by static loading. Stress mobilization in the surrounding soil was monitored using sensors embedded at different depths and distances from the model wall. Additionally, soil displacement and strain patterns were captured using Particle Image Velocimetry (PIV).

The study also incorporates numerical modeling to further investigate the behavior of tapered walls. Finite Element Method (FEM) simulations were conducted using OPTUMG2, while Limit Analysis was performed using LimitState GEO.

1.5 Thesis outlines

This thesis is structured into eight chapters, each focusing on different aspects of the research on the behavior of tapered piles during installation and under loading. The outline of the thesis is as follows:

Chapter 1: Introduction

This chapter provides an overview of the study, including its background, motivation, and research objectives. It also outlines the scope and significance of the study in improving pile foundation design in civil engineering applications.

Chapter 2: Principal tools for physical modelling in geotechnical engineering

This chapter presents common physical modeling techniques for investigating soil-structure interaction. It includes 1g model testing, calibration chamber tests, and centrifuge modeling, emphasizing their principles and applications. The chapter also presents some common image-

based analysis techniques for capturing soil deformation and failure mechanisms during physical tests. Methods such as X-ray imaging, Digital Image Correlation (DIC), and Particle Image Velocimetry (PIV) are reviewed based on their applications in analyzing soil displacement and strain in model tests.

Chapter 3: Pile classification, bearing capacity, and installation-induced effects

This chapter provides an overview of pile foundations, focusing on classification, bearing capacity, and installation-induced effects. It begins by categorizing piles based on installation methods, load transfer mechanisms, and pile geometry. The chapter then discusses the bearing capacity of piles, distinguishing between shaft and base resistance. An introduction to tapered piles, including their behavior in the sand and relevant analytical and empirical approaches, was presented. Finally, the chapter examines the geotechnical effects of pile installation, including stress redistribution, soil displacement, and the mobilization of shaft and base resistance**.**

Chapter 4: Research methodology

This chapter outlines the research methodology employed to investigate the installation effects of tapered piles in sandy soils. It begins with an introduction to the approach, followed by a detailed description of experimental testing using a geotechnical centrifuge. Key aspects include the centrifuge facility, scaling laws, physical models, experimental setup, and testing procedures. The chapter then describes the use of Particle Image Velocimetry (PIV) for image-based analysis, highlighting the GeoPIV-RG technique, image preprocessing, and extraction of displacement and strain fields. Finally, it presents the numerical modelling approach used in the study, covering Finite Element Modeling and Limit Analysis to simulate and analyze pile behavior.

Chapter 5: Stress distributions and load–settlement behavior

This chapter presents results from centrifuge model tests to evaluate stress mobilization and load–settlement behavior of model walls during installation and loading. It details the observed responses of model walls installed in sand, including their load–settlement behavior during both the installation and static loading phases. The chapter analyzes stress mobilization on the wall surface and within the surrounding soil mass at different stages: installation, post-installation, and loading. A comparative evaluation of walls with different taper angles is provided based on contact stress and soil stress distribution.

Chapter 6: Soil displacement and strain fields

This chapter presents the results of soil displacement and strain field analyses during the installation of model walls, based on image-based Particle Image Velocimetry (PIV) analysis. It includes both horizontal and vertical soil displacements induced by wall installation. The chapter also examines strain fields, focusing on shear and volumetric strain distributions. Additionally, it provides interpretations of the observed displacement and strain patterns and includes an analysis of individual soil particle movements captured through high-resolution image sequences. Comparative insights with previous studies are also discussed.

Chapter 7: Numerical analysis of load-settlement and failure mechanism

This chapter presents the results of numerical simulations conducted to evaluate the load–displacement behavior and failure mechanisms of model walls. It begins with Finite Element Method (FEM) analyses, including load–displacement responses, a parametric study to assess influencing factors, and the modeling of tapered wall geometries. Limit Analysis is also employed to estimate collapse loads and identify failure mechanisms. The chapter further includes a comparative analysis of the numerical results, with a focus on bearing capacity and the estimation of installation effects.

Chapter 8: Conclusions and recommendations

This chapter presents the conclusions drawn from the experimental and numerical investigations conducted in this study. The key findings are summarized in relation to the research objectives, highlighting the influence of pile tapering on installation effects and load-displacement behavior in sandy soils.

CHAPTER TWO

2. Principal tools for physical modelling in geotechnical engineering

2.1 Introduction

Physical modelling in geotechnics enables researchers to replicate soil behavior and soil-structure interaction under controlled laboratory conditions. It provides the advantage of controlled boundary conditions, stress states, and loading sequences that are often difficult to observe or isolate in the field. The main tools used in physical modelling include 1g model testing, calibration chamber testing, and centrifuge modelling.

2.2 1g model testing

1g model tests are small-scale physical models performed under Earth's natural gravitational field (1g). These tests are typically carried out in a rigid container using reconstituted soil samples and scaled-down structural elements. They are often used to observe deformation mechanisms, surface settlement, and soil failure in geotechnical systems such as foundations, retaining walls, and slopes under different loading and boundary conditions (Al Heib et al., 2020; Fang et al., 2023; Lee et al., 2011). However, a major limitation of 1g testing is the inability to reproduce the stress conditions that occur in full-scale field situations. Soil behavior, particularly in granular materials, is stress-dependent, and without proper modelling of stress ranges, results usually may not reflect realistic prototype responses.

2.3 Calibration chamber tests

Calibration chamber testing is one of the techniques for studying soil behavior under controlled laboratory conditions. These tests are especially useful for evaluating penetration resistance and soil–structure interaction. A typical calibration chamber consists of a rigid cylindrical container where uniform soil samples are reconstituted using methods such as dry pluviation, moist tamping, or vibration (Figure 2.1).

Vertical stress is typically applied using membranes filled with water or air and horizontal confining stress is introduced through flexible membranes or pressurized sidewalls to simulate in-situ stress conditions. The main advantage of calibration chambers is its ability to produce homogeneous and repeatable soil specimens under well-defined and complex boundary conditions such as constant stress, zero lateral/vertical strain, or controlled lateral stiffness (Foray, 1991).

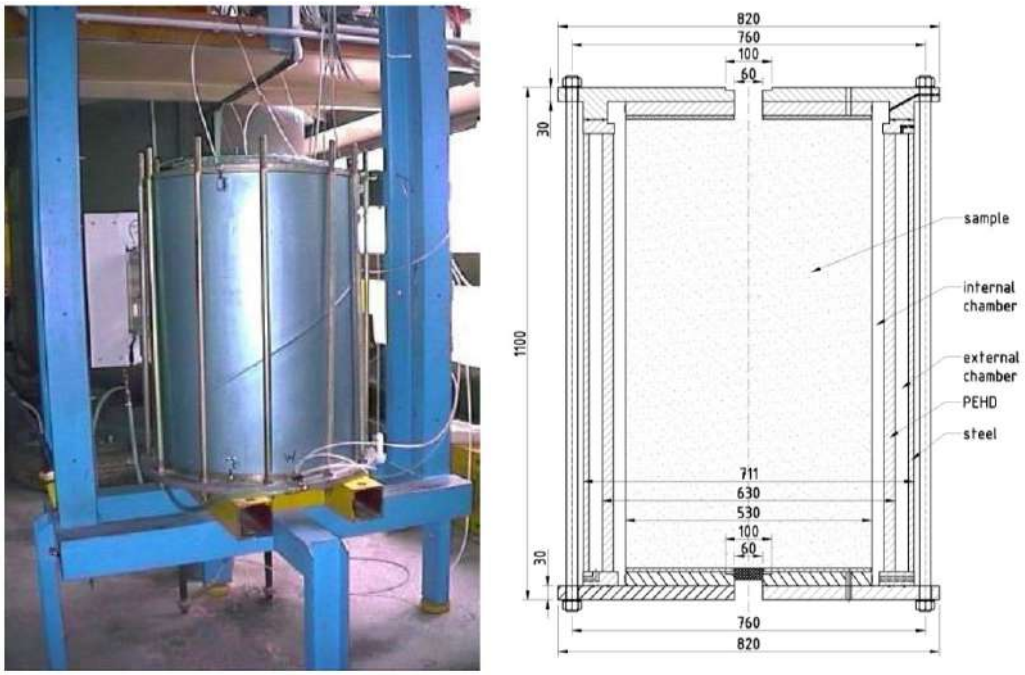

Figure 2.1: Calibration chamber at Gdańsk University of Technology (Bałachowski & Kurek, 2008)

White and Bolton (2004) used plane strain calibration chamber tests to investigate the mechanisms of displacement pile installation in sand. Boccalini et al. (2015) used a plane strain calibration chamber with transparent walls to observe soil displacement during pile installation. Despite their many advantages, calibration chambers have limitations. These include size effects related to the ratio of chamber diameter to model. They can simulate deep in-situ soil conditions, including overconsolidated soil mass. Some problems with transmission of vertical stress can, however, occur in the central part of the chamber and near its walls. Stress disturbances can also occur at the corners where vertical and horizontal membranes meet.

2.4 Centrifuge modelling

2.4.1 Introduction

Centrifuge modelling allows small-scale physical models to be tested under high gravity fields, typically at N times Earth's gravity, to replicate prototype stress conditions. This technique is useful for studying stress-dependent behavior in soils, such as stiffness changes, shear strength mobilization, and failure mechanisms (Taylor, 1995). A beam-type centrifuge is commonly used in such investigations. In this configuration, the model is mounted on a rotating arm and subjected to centrifugal acceleration, generating body forces proportional to radial distance and angular velocity. A schematic of the beam centrifuge at the University of Gustave Eiffel is shown in Figure 2.2.

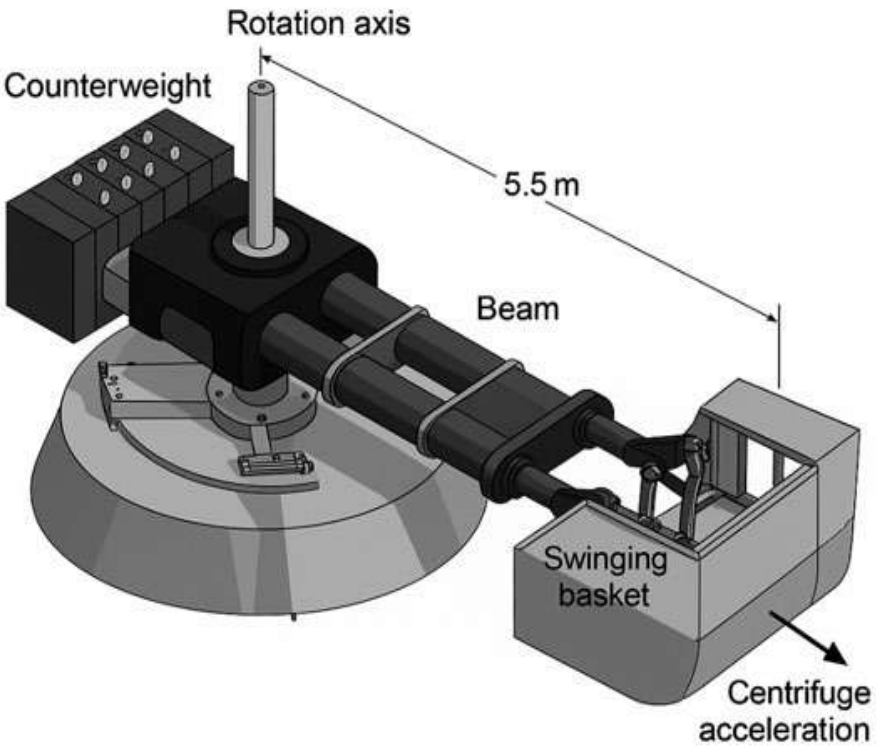

Figure 2.2: Schematic of a beam-type centrifuge at the University of Gustave Eiffel (Li, Blanc, et al., 2022)

2.4.2 Principles and Scaling Laws

The principles of centrifuge modeling depend on replicating the stress field of a full-scale (prototype) system within a reduced scale by subjecting it to a centrifugal acceleration of N times Earth's gravity (Ng), where N is the gravity scaling factor (Schofield, 1980; Taylor, 1995).

Under this condition, geometric dimensions are scaled down, and the stress distribution within the soil remains equivalent to the prototype. This enables rigorous physical modelling, where both the same strains and stresses are conserved in the model and the prototype. For example, length scales by 1/N, displacement by 1/N, and force by $1/N^2$, whereas stress and strain remain the same between the model and prototype. The common scaling laws adopted by centrifuge testing are summarized in Table 2.1. Some physical phenomena, particularly those influenced

by soil-structure interaction and grain size, do not scale perfectly. As a result, the distortion in physical modelling may arise (Garnier et al., 2007).

Table 2.1: Selected scaling laws in centrifuge modelling (Garnier et al., 2007)

Parameter	**Model/Prototype Scale (at N-g)**
Length	1/N
Stress	1
Strain	1
Acceleration	N
Force	$1/N^2$
Displacement	1/N
Time (diffusion processes)	$1/N^2$
Time (dynamic processes)	1/N

2.5 Grain size and boundary effects in physical modelling

Scale effects may arise, especially when the dimensions of the model approach the size of individual soil particles (Bolton & Lau, 1988; Foray, 1991; Foray et al., 1998; Bałachowski, 2006, 2007; Zhuang & Yu, 2018). These grain-scale effects are related to the localization of deformation in the soil mass and the formation of the shear band within the interface. The thickness of this shear band remains the same around the small model and the prototype. Thus, the dilatancy within the shear band has a higher influence on the behavior of the model than for the prototype.

2.5.1 Scale effects on shaft resistances

Shaft friction is sensitive to scale effects, especially in dense and dilative sands. This is due to the localized nature of shear transfer and the complex interaction between the soil and the pile-soil interface. Foray et al. (1998) highlighted that radial stiffness at the interface increases inversely with pile diameter, leading to overestimating shaft friction in small-scale models, especially under low-stress levels. Bałachowski (2006) demonstrated that the scale effect for the shaft friction, defined as the ratio of shear stress mobilized in a small-scale model to that in a prototype, is significantly influenced by the ratio of pile diameter to shear band thickness (D/e). This scale effect can exceed unity for dilative interfaces (dense sand and rough plate) and can be less than one for contractive behavior within the interface (loose quartz sand or carbonate sand with smooth plate surface). In case of dense quartz sand and rough pile surface D/e ratio should be larger than 15 to minimize the grain size effect in lateral friction. Similarly, this ratio should exceed 3 to avoid the grain size effect for loose quartz sand and smooth pile.

2.5.2 Grain scale effects on base resistance

Base resistance is generally less susceptible to grain scale effects than the shaft friction due to the high-stress level near the tip. Early work by Bolton and Lau (1988) conducted model tests on footings in granular soils and showed that scale effects on base resistance are due to stress level variations.

Several studies have shown that size effects in penetration resistance become negligible when the ratio of pile base diameter to mean grain size (B/d_{50}) exceeds a critical threshold. Bolton and Lau (1988), Foray et al. (1998), and Bałachowski (2007), suggest that $B/d_{50} \geq 10–20$ is sufficient to minimize such effects. Zhuang and Yu (2018) emphasize that $B/d_{50} \geq 30$ is required under low-stress or shallow-depth conditions.

2.5.3 Boundary effects

The limited size of calibration chambers can introduce significant boundary effects. These effect depends on several factors, including the ratio of chamber diameter to model diameter, applied boundary conditions, relative density, and stress level.

These effects arise due to the confinement imposed by the rigid or semi-rigid container walls, which constrain lateral soil movement and alter the natural development of failure mechanisms, leading to overestimation of soil stiffness and strength (Tsai et al., 2021). To mitigate these effects, studies have proposed minimum spacing requirements. Lunne et al. (1991) reported that chamber size effects become negligible when the chamber-to-penetrometer diameter ratio exceeds 30 in loose sand and 70 in dense quartz sand. Craig (1994) recommends a minimum distance of five times the pile diameter (5D) from the model pile to the container wall to reduce boundary interference in pile testing. Similarly, Gui et al. (1998) recommended that the distance from the model pile to the side boundary should be greater than 10 times the pile diameter ($s/B > 10$) to minimize boundary effects on penetration resistance.

Additionally, vertical boundary effects must also be considered. If the distance between the cone or pile tip and the bottom of the container is too small, it can restrict downward soil movement, leading to increases in measured resistance or stress concentrations. To allow the failure mechanism to fully develop without interference from the bottom boundary, adequate vertical clearance is required. Gui et al**.** (1998) recommend that the distance from the pile tip to the bottom boundary be at least 10 times the pile diameter ($s/B \geq 10$) to minimize bottom boundary effects.

In some calibration chamber setups, flexible boundaries with imposed lateral stiffness, typically implemented using pressurized rubber membranes are used to reduce boundary constraints (Foray, 1991; Balachowski, 2006; Kluger et al., 2021).

2.5.4 Grain crushing effects

Grain crushing is another phenomenon that influences soil behavior during pile installation and penetration testing. It refers to the breakage of soil particles when the applied stress exceeds the crushing strength of the grains (Hyodo et al., 2017; Vesic & Clough, 1968; Yamamuro et al., 1996; Balachowski, 2008). Crushing increases the compressibility of sand and alters its mechanical properties, such as internal friction angle and dilatancy (Ciantia et al., 2019; Tovar-Valencia et al., 2023). Yang et al. (2010) observed that grain crushing occurs near the pile tip and shaft, where stress concentrations are highest. Their study revealed that the formation of compacted shear zones around the pile tip results from particle breakage. This reduces radial effective stress and interface friction angle, affecting the interface shear behavior. Consequently, it may lead to an underestimation of pile shaft resistance in model tests. In quartz sands, the phenomenon is becoming important at mean stress higher than 2-3 MPa. The analysis of calibration chamber penetration tests by Yang et al. (2010) shows that the threshold stress for intensive grain crushing in Fontainebleau sand corresponds to q_c=5MPa.

2.6 Image-based analysis in physical modelling

2.6.1 Introduction

Image-based analysis techniques have emerged as powerful tools in geotechnical physical modelling for non-intrusive and high-resolution observation of soil deformation, displacement fields, and failure mechanisms. These techniques offer a unique advantage over conventional instrumentation by allowing full-field visualization of soil behavior during loading or installation processes. Initially developed in disciplines such as fluid mechanics, and their adoption in geotechnical engineering has grown substantially in recent decades for studying soil–structure interaction.

Among the most widely used image-based techniques in geotechnics are X-ray Computed Tomography (X-ray CT), Digital Image Correlation (DIC), and Particle Image Velocimetry (PIV). Each offers unique benefits and is selected based on the scale of the model, material transparency, resolution requirements, and experimental objectives.

2.6.2 X-ray Imaging

X-ray imaging is a non-destructive technique that enables internal visualization of geomaterials by exploiting differential attenuation of X-rays through materials of varying densities. In geotechnical engineering, X-ray CT and micro-CT are employed to observe deformation patterns, void structure, and failure development within soils and around structural elements. The X-ray imaging setup used to capture soil deformation and internal structure during pile installation is shown in Figure 2.3.

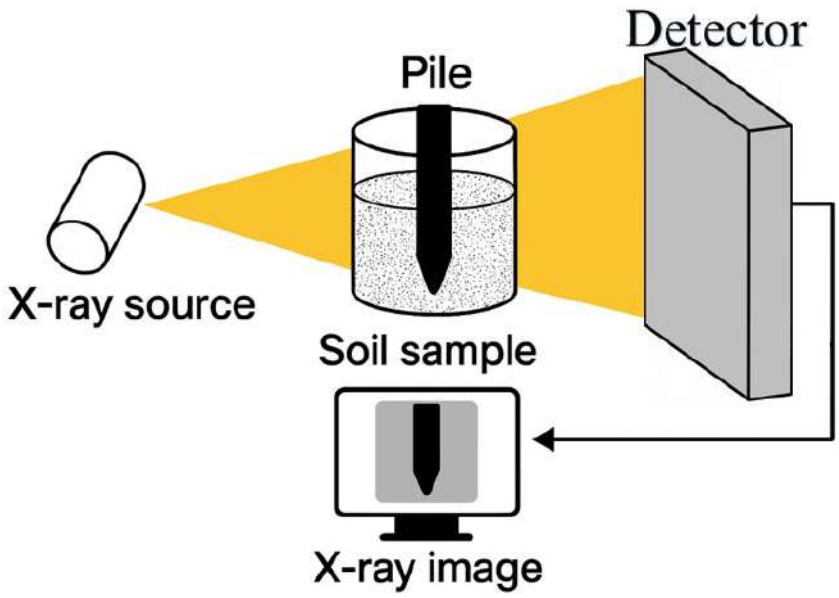

Figure 2.3: X-ray imaging system for soil deformation analysis

The application of X-ray techniques in physical modelling dates back to the early 1960s, with Robinsky and Morrison (1964) using radiography to investigate sand displacement and compaction around model friction piles.

Several subsequent studies have employed X-ray methods to investigate soil behavior under various loading and boundary conditions. For example, Otani et al. (2000) and Shi et al. (1999) used X-ray CT to identify shear zones and internal deformation in loaded soil. Nguyen et al. (2019) and Yu et al. (2021) applied X-ray CT to study changes in pore morphology and compressibility. Watanabe et al. (2012) and Takano et al. (2015) further advanced the method by integrating it with DIC for strain visualization.

For investigating pile–soil interaction, Doreau-Malioche et al. (2019) used X-ray tomography with DIC to investigate mechanisms at the soil–pile interface under axial loading. Their result shows that X-ray scans revealed insights into soil fabric evolution during pile loading. Inside the shear band surrounding the pile, contact orientation anisotropy developed, with contacts reoriented toward 60°-90° relative to the pile axis in both compression and tension. The coordination number near the pile shaft was lower than in the outer regions which indicate dilatancy and contact loss due to large shear strains. They observed that pile loading induces significant microstructural rearrangements in the soil and influences macroscopic shaft resistance.

King et al. (2019) utilized X-ray computed tomography (CT) to investigate 3D soil displacement and strain localization in a physical model of a piled embankment. Results showed the progressive development of arching and shear bands between piles, revealing the spatial distribution of vertical displacement and shear strains in dense and medium-dense sands.

Kido et al. (2022) used X-ray micro-computed tomography (CT) to investigate the bearing mechanism of open and closed-ended piles. Pile-loading tests were conducted on model ground with varying bearing layer thicknesses, and the deformation of soil around the pile tip was captured using X-ray CT. The results showed that for open-ended piles, when the bearing layer thickness was small, significant downward displacement of internal soil occurred, which reduce density and lower base resistance. However, when the bearing layer thickness exceeded

three times the pile diameter, both open and closed-ended piles achieved similar bearing capacities.

X-ray imaging has also been applied in related soil–structure interaction studies, such as reinforcement pullout tests (Kido et al., 2021, 2022) and shown its capability to capture internal deformation and strain localization in dense sand.

Despite these advancements, X-ray imaging is generally limited to small-scale experiments due to equipment constraints and resolution demands. Its application in centrifuge modeling remains rare due to space limitations and complexity. Moreover, interpreting volumetric CT data requires sophisticated image processing tools.

2.6.3 Digital Image Correlation (DIC)

DIC is a non-contact, full-field optical measurement technique that tracks the movement of a speckle pattern applied to the soil surface across sequential digital images. By comparing a reference image with deformed states, it generates high-resolution displacement and strain fields, making it well-suited for geotechnical model testing (Chen et al., 2017; Leśniewska et al., 2014).

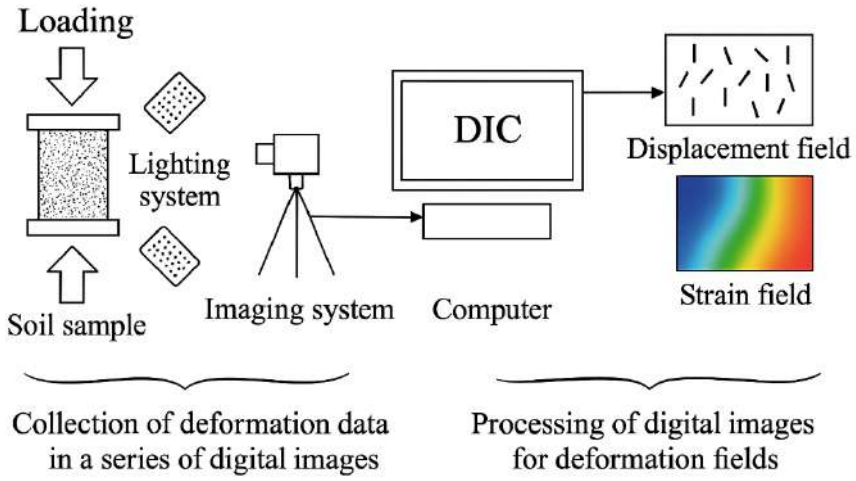

Figure 2.4: Schematic of the Digital Image Correlation (DIC) process (Bhandari et al., 2023)

The overall procedure for applying Digital Image Correlation (DIC) in geotechnical testing is illustrated in Figure 2.4. This process begins with image acquisition, where a speckle-patterned soil sample is subjected to loading, and images are continuously recorded by an imaging system under controlled lighting. The captured digital images are then processed using DIC software to extract full-field displacement and strain data. As shown in Figure 2.4, the output includes displacement vectors and strain maps that provide insights into deformation patterns and failure mechanisms in the soil.

2.6.4 Particle Image Velocimetry (PIV)

2.6.4.1 Introduction

PIV is a high-resolution optical technique originally adapted from fluid mechanics to quantify deformation and velocity fields in granular materials. It works by tracking the movement of natural texture or seeded particles across successive digital images using cross-correlation of sub-regions known as interrogation windows (White & Take, 2002). In geotechnical engineering, PIV was used as one of the tools for image-based analysis. A simplified schematic of a typical PIV setup used in geotechnical physical modelling is shown in Figure 2.5.

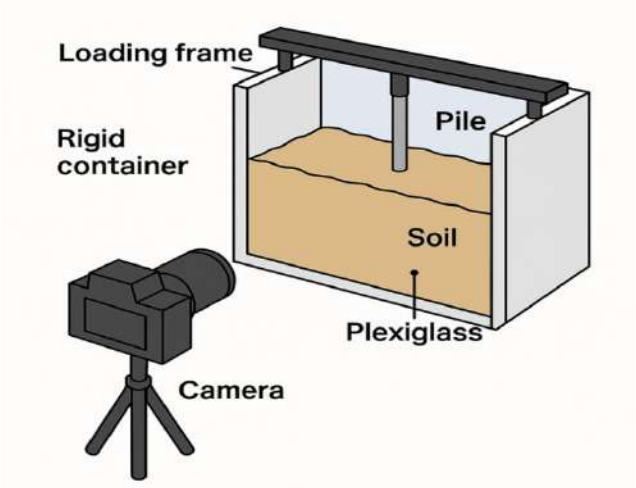

Figure 2.5: Typical PIV setup in geotechnical model testing

2.6.4.2 Principles of Image-Based Analysis with PIV

The main principle of PIV lies in correlating sub-regions of digital images taken at successive stages of deformation. Each image is divided into a mesh of square patches, and a cross-correlation algorithm is applied between corresponding interrogation windows to compute displacement vectors. To change pixel displacements into real-world measurements, image-to-object space transformation is applied. Sub-pixel accuracy is typically achieved using interpolation methods applied to the correlation peak (Raffel et al., 2018). Figure 2.6 illustrates the fundamental concept of sub-region matching through cross-correlation.

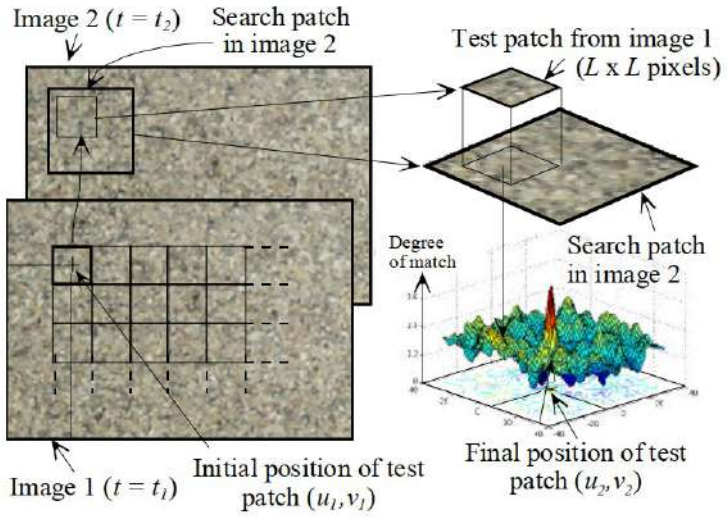

Figure 2.6: PIV Principle, Adapted from (White & Take, 2002).

The accuracy of displacement measurements depends on the quality of image correlation, the size of the interrogation windows, and the ability to resolve sub-pixel displacements. To further enhance performance under complex deformation conditions, Stanier et al. (2016) proposed GeoPIV-RG which is an advanced implementation of the traditional GeoPIV method (White et al., 2003). This version integrates subset shape functions, reliability-guided correlation, and automatic reference image updating. These improvements reduce correlation loss and random walk errors which enables more reliable tracking of soil movements even during large deformations.

2.7 Summary

Physical modelling remains a keystone technique in geotechnical engineering for investigating soil–structure interaction under controlled conditions. Among the available methods, 1g model testing, calibration chamber experiments, and centrifuge modelling each has specific advantages and limitations. 1g model testing does not reproduce the in-situ stress conditions for modeling stress-dependent soil responses. Calibration chamber testing allows controlled penetration studies and interface analysis. It is effective for investigating soil response to penetration and interface shear behavior. However, it is restricted to uniform boundary conditions and simplified geometries.

Centrifuge modelling enables simulations under high-g levels for small-scale models to replicate the stress fields of full-scale prototypes. This tool is commonly used for studying stress-dependent behaviours such as soil densification, stress redistribution, and grain crushing during pile installation. Image-based analysis techniques such as X-ray imaging, Digital Image Correlation (DIC), and Particle Image Velocimetry (PIV) have been used in physical modelling to investigate soil deformation and failure mechanisms.

CHAPTER THREE

3. Pile classification, bearing capacity, and installation-induced effects

3.1 Pile classifications

Piles can be classified in various ways depending on their geometry, material, function, and method of installation. However, when considering the installation effects, particularly in granular soils such as sand, the most common classifications are those based on the method of installation, the mechanism of load transfer, and pile shape. These classifications determine how the pile interacts with the surrounding soil during and after installation, affecting stress distribution, soil displacement, densification, overconsolidation, and pore pressure changes.

3.1.1 Classification based on installation method

Pile foundations can be broadly classified based on the method of installation into displacement piles and non-displacement piles. Displacement piles such as driven, jacked, pushed-in, screw piles or helical ones are known to generate higher soil disturbance during installation, which contributes positively to pile performance by increasing lateral effective stress and relative density in non-cohesive soils (Henke & Grabe, 2008). In contrast, non-displacement piling methods, such as bored piles, often lead to stress relaxation and reduced shaft resistance (Zarrabi & Eslami, 2016).

The installation of displacement piles in non-cohesive soils causes significant lateral and vertical soil displacement and leads to stress redistribution, densification, and often enhanced shaft resistance. These effects have been extensively validated through experimental investigations (Lehane & White, 2005; Anusic et al., 2019; Yang et al., 2014; Jardine et al.,

2013). *Driven piles*, installed using dynamic impact or vibratory hammers, generate significant soil movement and lateral stress increase. Their effectiveness in granular soils has been demonstrated in numerous studies. However, their high noise and vibration levels may restrict their use in urban or vibration-sensitive areas (Herrera, 2021).

To address such limitations, silent piling techniques, including press-in or pushed-in technology, have been developed (White, 2002; Black, 2012; Yaseen Sharif et al., 2022; Cerfontaine et al., 2023). It involves the gradual insertion of piles into the ground using static loading without noise and vibration. This method minimizes soil disturbance, noise, and vibration, making it well-suited for testing environments and urban construction near sensitive structures (White et al., 2002; Rockhill et al., 2003).

Jacked piles, installed using static hydraulic force, are driven into the ground without dynamic impact or vibration. This installation method minimizes noise and environmental disturbance, making it suitable for urban areas with vibration-sensitive infrastructure. Despite the low-vibration nature of the installation, the continuous static force applied induces lateral and vertical soil displacement and stress changes.

Another type of displacement pile is the *screw pile*, which is installed through continuous rotation without pre-drilling and displace soil laterally as it penetrates. This installation method causes substantial soil deformation and densification around the shaft and increases radial stress and enhancing shaft resistance (Krasinski, 2015). Several studies have extensively studied the installation effects of screw piles. For example, Meng et al. (2015) performed field tests to measure horizontal soil movements and pore pressures around piles with screw-shaped shafts, and showed that soil disturbance was concentrated within a limited zone that stabilized within days after installation.

Helical piles are another type of displacement piles that consist of a central steel shaft with one or more helices or helical plates attached at intervals. These are installed by rotating the shaft into the ground using hydraulic torque motors, which causes minimal soil removal and results in an installation process that relies on both shaft friction and end-bearing resistance developed through the helices (Perko, 2009). The performance of helical piles depends on several factors, including the installation torque used (Tsuha et al., 2010) and installation method (Schiavon et al., 2020).

In contrast, non-displacement piles, such as bored cast-in-situ piles or drilled shafts**,** are installed by first removing soil to create a borehole, which is then filled with concrete or other material. These methods generally cause less soil disturbance but often lead to stress relaxation and lower shaft resistance, particularly in cohesionless soils (Coduto et al., 2016). While suitable for use in vibration-sensitive areas, their performance is more dependent on construction quality and ground conditions (Samyukta & Babu, 2022).

3.1.2 Classification by load transfer mechanism

Pile foundations can be classified based on how the applied load is transmitted to the surrounding soil through three mechanisms: end bearing, shaft friction, or a combination of both. End-bearing piles transfer the majority of the load directly to a strong underlying stratum such as rock or dense sand, usually located at or near the pile tip. During installation, especially for displacement piles, significant stress concentration develops in the soil beneath the tip, which enhances the mobilization of base resistance (Poulos & Mattes, 1969).

On the other hand, friction piles derive their load-carrying capacity mainly through shear resistance developed along the pile–soil interface. These piles are effective in cases where a firm bearing layer is not available within practical depths, such as in deep deposits of soft or loose soils. The skin friction is mobilized progressively along the shaft length, and its development depends on factors such as soil type, pile material and surface roughness, and the

pile installation method (Tavenas, 1971). In practical applications, combined end-bearing and friction mechanisms are used. In such piles, both base resistance and shaft friction contribute to the total load capacity (Bowles & Guo, 1996).

3.1.3 Classification based on pile shape

Pile foundations can be classified based on their geometric shape into the following types:

Straight-shaft piles

These piles have a uniform cross-sectional area along their entire length and are the most widely used type in both bored and driven applications. They are typically circular or square in cross-section (Choi et al., 2015), although other shapes like H-piles and X-piles are also used (Lu et al., 2017; Salah et al., 2025).

Tapered piles

Tapered piles, which gradually decrease in diameter from head to base. The degree of this diameter decrease is defined by the taper angle. These piles can be circular, square, and X-shaped in cross-section (Shabanpour & Ghazavi, 2022). Tapered piles have higher bearing capacity and lower installation resistance than cylindrical piles (Rybnikov, 1990; Suits et al., 2011).

Bulbous (under-reamed) piles

Bulbous or under-reamed piles have one or more enlarged sections (bulbs), typically near the pile base. These enlargements increase the contact area at the base of the pile and improve the pile capacity to resist uplift and compressive loads (Alhassani, 2021). The bulbs provide enhanced anchorage and improved shaft resistance.

Stepped piles

Stepped piles are composed of shaft segments with varying diameters arranged in a stepwise manner. Stepped profiles are often produced using segmental precast units or staged boring techniques. Ismael (2010) conducted static lateral loading on circular step-tapered bored piles and the results show that increasing the diameter in the upper segment improved the lateral load capacity by 60%.

Conical end pile

Conical end piles feature a tapered tip that enables penetration into dense soils. The conical shape allows for smoother soil displacement in layered or dense sand deposits, leading to reduced installation resistance (Liu et al., 2020).

Enlarged base pile

Enlarged base piles are characterized by a widened base formed at the bottom of a straight shaft. This geometry enhances base resistance and is effective in transferring structural loads to deeper, more competent soil layers (Ibrahim & Karkush, 2023). Experimental and numerical studies by (Neely, 1990; Sokolov et al., 2021) have shown that the performance of belled piles under axial loads is higher than that of uniform-diameter piles. However, their use is limited in gravelly or boulder-rich strata where forming the bell shape becomes technically challenging.

Open-ended piles

Open-ended piles, also known as pipe piles, are hollow cylindrical piles with an open bottom that allows soil to enter the pile during installation. They are commonly used in both onshore and offshore applications, where deep penetration is required or where pile driving through dense strata is necessary. During installation, the soil enters the inner cavity, which reduces driving resistance compared to closed-ended piles (Paik et al., 2003). The load transfer

mechanism of open-ended piles involves both the external shaft friction and the internal friction along the soil plug that forms inside the pile (Paik et al., 2003) .

The degree of plugging, ranging from fully unplugged to fully plugged, influences the axial capacity of these piles (Liu et al., 2019). In unplugged conditions, only the annular cross-section contributes to end bearing, whereas in plugged conditions, the entire cross-sectional area at the base mobilizes resistance, similar to a closed-ended pile (Kodsy & Iskander, 2022; Wiesenthal & Henke, 2025). A summary of different pile types based on geometry is shown in Figure 3.1.

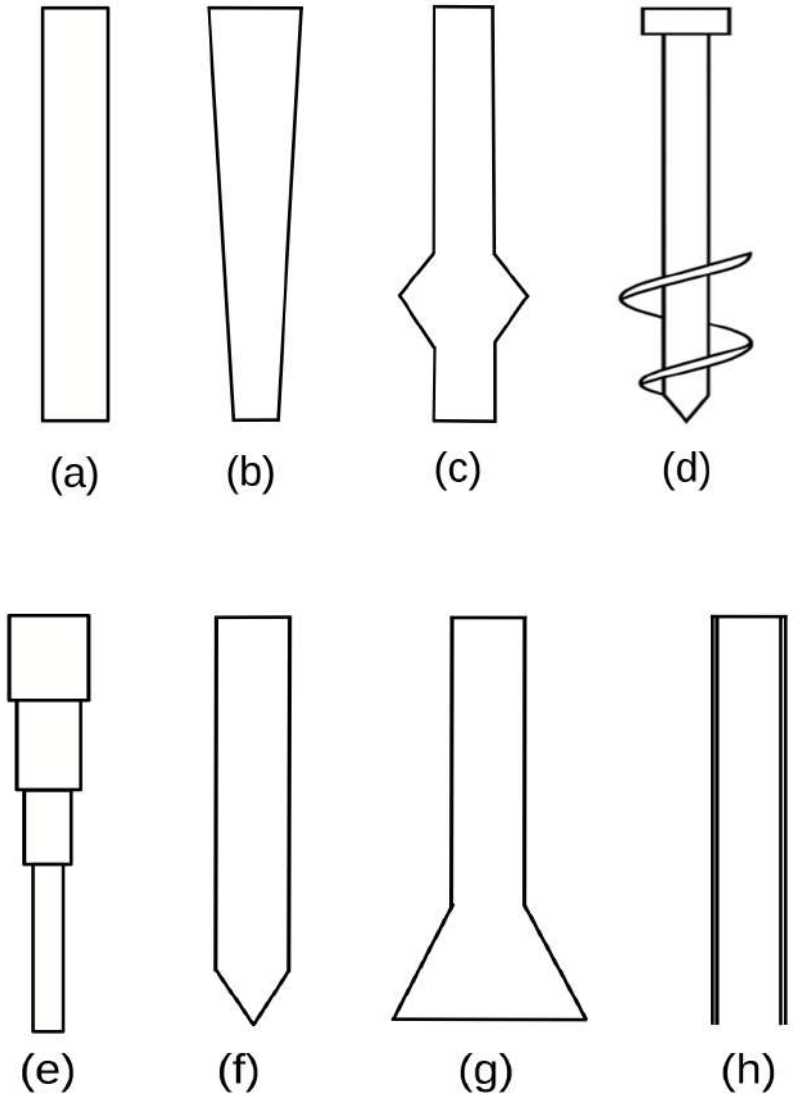

Figure 3.1: Types of pile foundations based on shaft geometry: (a) Cylindrical (Straight-Shaft) Pile, (b) Tapered Pile, (c) Bulbous (Under-Reamed) Pile, (d) Helical Pile e) Stepped Pile, (f) Conical Pile. g) Enlarged base pile h) open-ended pile (not scaled)

3.2 Bearing capacity of piles

The total bearing capacity of a pile under axial compression load is typically composed of two components: the shaft resistance (also known as skin friction) and the base resistance (end bearing). The ultimate load-carrying capacity (Q_{ult}) of a pile in compression can be expressed as:

$$Q_u = Q_S + Q_b \tag{3.1}$$

Where: Q_u is the total ultimate axial capacity of the pile, Q_S is the total shaft resistance, and Q_b is base resistance. In the case of tension piles, the base resistance is negligible, and the tensile capacity is provided primarily by shaft resistance. The ultimate tensile capacity can be expressed as:

$$Q_u = Q_S \tag{3.2}$$

The mobilized shaft resistance in tension may differ from that in compression due to reduced interface friction.

3.2.1 Shaft resistance

Shaft resistance is mobilized by shear stresses developed at the pile–soil interface due to relative displacement during axial loading.

$$Q_S = \int_0^L f_s(z).p(z)dz \tag{3.3}$$

Where $f_s(z)$ is unit shaft resistance at depth z, $p(z)$ is pile perimeter at depth z, L is total embedded length of the pile and z is depth variable from 0 at the ground surface to L at the pile tip. The pile perimeter p(z) decreases with depth in case of tapered piles, while it remains constant for classical straight ones.

For uniform in cross-section pile, $p(z)$ = πD (for circular piles), the equation becomes:

$$Q_S = \pi D \int_0^L f_s\,(z)\,dz \tag{3.4}$$

The β-method is a commonly used empirical approach for estimating the shaft resistance of piles in drained conditions. The method assumes that the shaft resistance is proportional to the effective vertical stress acting at a given depth along the pile shaft.

$$f_s = \beta . \sigma_v' \tag{3.5}$$

Where β is an empirical coefficient that depends on soil type and density, stress level, and pile installation method, and σ_v' is the vertical effective stress.

β is related to fundamental soil–structure interaction parameters through the following expression:

$$\beta = K tan\delta_{cv'} \tag{3.6}$$

Where:

- K is the lateral earth pressure coefficient during pile loading at failure, and
- $\delta_{cv'}$ is the pile–soil interface friction angle at large displacement, i.e. at constant volume conditions.

In case of bored piles, the coefficient K can be roughly approximated using Jaky's expression $K_0 = 1 - \sin\phi'$ in the absence of detailed site-specific data, where ϕ′ is the effective internal friction angle of the soil.

More detailed numerical analysis by Loukidis and Salgado (2008) showed that the mobilized lateral earth pressure coefficient (K) depends on both the initial coefficient at rest K_0 and the relative density of soil (D_r). As shown in Figure 3.2, the ratio K/K_0 increases with increasing relative density and decreases with increasing K_0. This shows that the potential for lateral stress build-up decreases with increasing K_0; in heavily overconsolidated sands (K_0=2.0), the normalized mobilized stress K/K_0 is significantly lower than in normally consolidated sands

(K_0=0.4 to 0.5). However, within the narrow K_0 range of 0.4–0.5, typical of normally consolidated sands, the variation in K is important and should not be neglected for practical purposes, especially in dense and very dense sands. Similarly, the β coefficient for non-displacement piles is higher at small stress level (Figure 3.3).

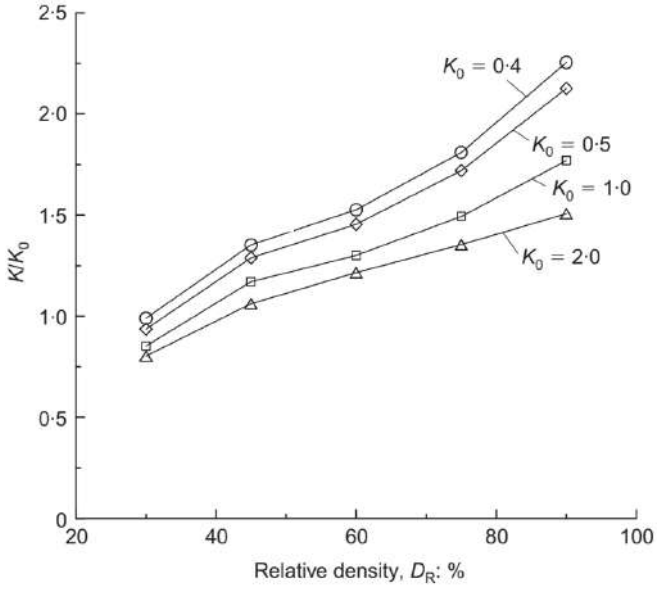

Figure 3.2: Variation of normalized lateral earth pressure coefficient (K/K_0) with relative density D_R for different values of initial K_0 (Loukidis & Salgado, 2008)

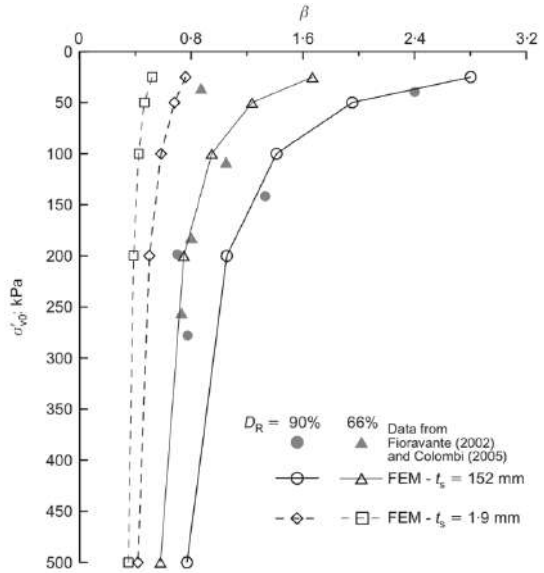

Figure 3.3: Variation of shaft resistance coefficient (β) with effective overburden stress (Loukidis & Salgado, 2008)

K value may vary depending on the pile installation method. The variation of the lateral earth pressure coefficient K with embedment ratio L/D and internal friction angle ϕ' for driven pile is shown in Figure 3.4. The value of K increases with increasing L/D and ϕ'. $\delta cv'$ is soil–pile friction angle and appears to be in the range from $0.5\phi'$ to $0.8\phi'$(Das, 2007).

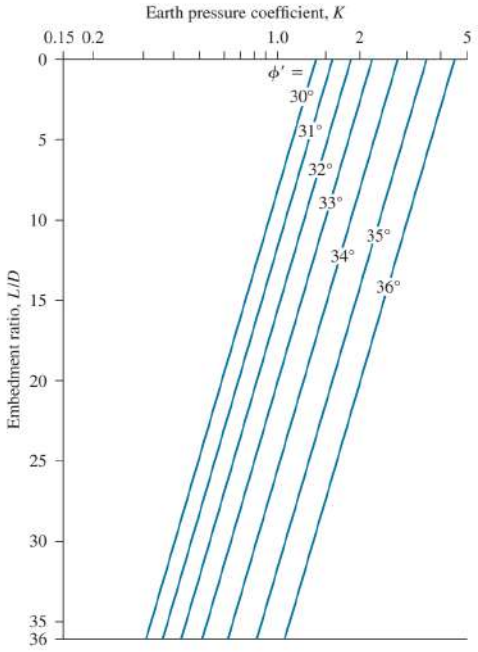

Figure 3.4: Variation of lateral earth pressure coefficient (K) with embedment ratio (L/D) and internal friction angle (ϕ') (Das & Sivakugan, 2019)

The mobilization of shaft resistance was analogized to interface direct shear tests under constant normal stiffness (CNS) conditions by Boulon (1989), Foray et al. (1998), and Lehane and White (2005). The pile-soil interface behaves as a thin shearing zone confined by the surrounding soil, which resists volumetric changes during shearing (Figure 3.5). During axial loading, dilation within this shear zone leads to an increase in lateral stress acting on the pile shaft. This behavior is similar to that observed in CNS shear tests, where constrained dilation results in increased normal stress and shear resistance.

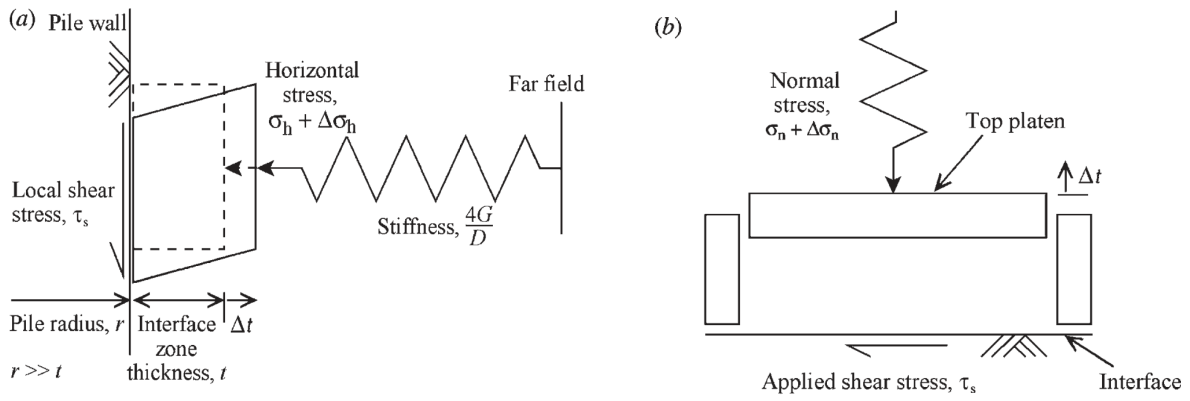

Figure 3.5: Analogy between shaft friction mobilization at a pile–soil interface and a constant normal stiffness (CNS) direct shear test (Lehane & White, 2005).

3.2.2 Base resistance

The base resistance is typically estimated using bearing capacity theory expressed as:

$$Q_b = q_b . A_b \tag{3.7}$$

Where q_b is the unit base resistance, and A_b is the base area of the pile.

The unit base resistance q_b for cohesionless soil is estimated using the bearing capacity expression.

$$q_b = N_q . \sigma_v' \tag{3.8}$$

Where N_q is a bearing capacity factor dependent on the internal friction angle of the soil below the pile base, and σ_v' is the effective vertical stress at the pile tip level. The coefficient N_q is a dimensionless bearing capacity factor.

Meyerhof (1976) proposed a theoretical and empirical relationship between N_q and the effective friction angle of the soil (ϕ'). It is suggested that N_q increases exponentially with ϕ', based on both limit equilibrium theory and field pile load test data.

$$N_q = e^{\pi . tan\emptyset'} . tan^2(45 + \frac{\emptyset'}{2}) \tag{3.9}$$

Coyle and Castello (1981) developed field-representative method to estimate Nq, based on driven pile load test results in cohesionless soils. Their approach introduces the embedment ratio L/D (pile length over diameter) as a parameter affecting base resistance, in addition to ϕ′.

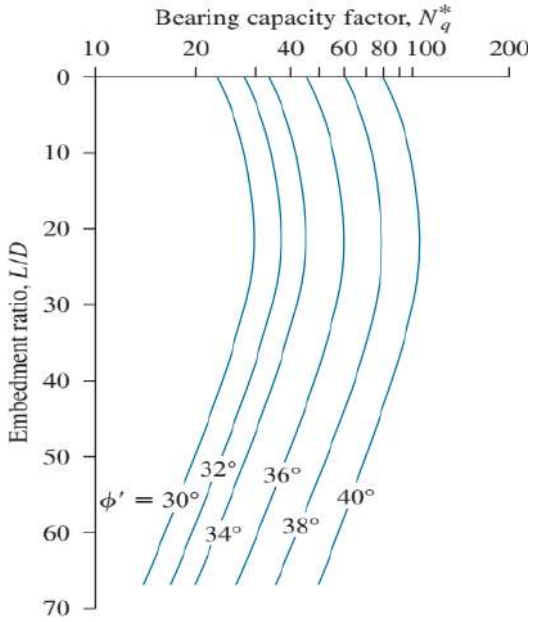

Figure 3.6: Variation of Nq with L/D (Coyle and Castello, 1981)

In case of an elongated, base shape different from a cylindrical or square one, the unit base resistance is reduced, and an additional shape coefficient should be applied in equation 3.7. This coefficient is related to the ratio of base width to base breadth (W/B). Below critical depth, the shape coefficient is equal to 1, i.e., no reduction of unit base resistance is assumed. For (W/B) greater than 10, plane strain conditions can be assumed. The theoretical solution for base resistance in plane strain conditions in Fontainebleau dense sand for different pile embedment was proposed by Gui and Muhunthan (2006). Their analysis considered stress-dependent strength and surface roughness effects. They determined depth-dependent bearing capacity factors (N_q) under both plane strain and axisymmetric conditions. Table 3.2 shows N_q values for various friction angles (ϕ) and interface roughness ratios (δ/ϕ) for L/B=8, the maximum embedment ratio given in this paper.

Table 3.1: Bearing capacity factor (Nq) under axisymmetric and plane strain conditions for embedment ratio (L/B) equal 8 (Gui & Muhunthan, 2006)

δ/ϕ	Axisymmetric (N_q)			Plane Strain (N_q)		
	$\phi=30^0$	$\phi=35^0$	$\phi=40^0$	$\phi=30^0$	$\phi=35^0$	$\phi=40^0$
0.00	104.3	198.9	359.7	20.2	27.5	38.6
0.25	139.3	282.8	522.3	25.5	37.7	57.4
0.50	174.2	360.7	710.7	30.7	48.6	80.2
0.75	210.9	432.2	892.4	36.1	60.0	104.9
1.00	236.2	485.7	1031.3	40.9	70.7	129.5

The base resistance varies significantly between axisymmetric and plane strain conditions. Gui and Muhunthan (2006) showed that for the same soil properties, N_q values are higher under axisymmetric conditions due to the different stress distributions and failure mechanisms. At $\phi=40^\circ$, for instance, when the interface is perfectly smooth ($\delta/\phi=0$), the N_q value under axisymmetric conditions is 9.3 times higher than that under plane strain. As the interface roughness increases, this difference decreases. For a perfectly rough interface ($\delta/\phi=1.0$), the Nq under axisymmetric conditions is approximately 8 times higher than in plane strain. This indicates that the base resistance increases with pile roughness in both cases, and it is more pronounced in plane strain. Under axisymmetric conditions ($\phi = 40°$), increasing δ/ϕ from 0 to 0.5 doubles the N_q value, and raising it to 1.0 increases N_q by about 2.9 times. In plane strain, N_q increases by 2.1 times for $\delta/\phi = 0.5$ and by about 3.4 times for $\delta/\phi = 1.0$. Thus, although the absolute increase is greater in axisymmetric cases, the effect of interface roughness is more pronounced under plane strain conditions.

3.3 Behavior of tapered piles in sand

3.3.1 Introduction

Tapered piles are characterized by a gradual decrease in diameter from head to base. The taper angle, typically denoted as α, is defined as the inclination of the pile shaft (Figure 3.7a). Linear tapering is most common due to its ease of fabrication. Tapered piles may also be stepped or hybrid in form. A comparative schematic of tapered, stepped, and hybrid piles is presented in Figure 3.7.

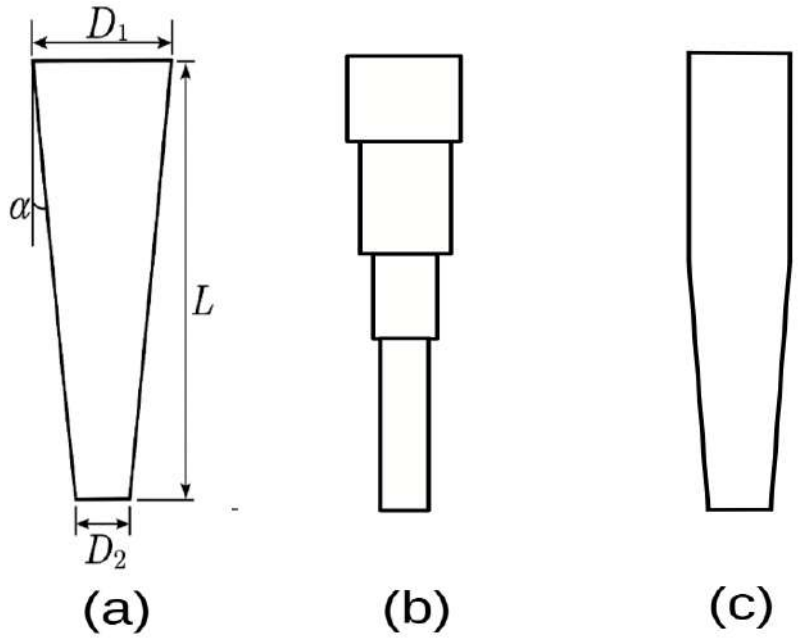

Figure 3.7: Schematic diagram of a) tapered, b) stepped, and c) hybrid piles (not scaled). L is Pile length, D_1 is head diameter, D_2 is base diameter, and α is taper angle.

Tapered piles have also been used as compaction piles in early applications using natural tapered timber piles (Christin et al., 2013; Stuedlein et al., 2016). These piles driven into loose granular soils and causes lateral displacement and densification of the surrounding soil mass, which improves bearing capacity and reduces settlement (Zil'berberg & Sherstnev, 1990). Similarly, precast concrete tapered piles have been used for ground improvement (Shabanpour

& Ghazavi, 2022; Tavasoli & Ghazavi, 2020). One of the practical applications is at the John F. Kennedy International Airport, where tapered piles have been used since the 1940s to support terminals and transit systems, with taper angles ranging from 0.2° in timber piles to 1.6° in steel Tapertube piles (Horvath et al., 2004; Horvath & Trochalides, 2004).

3.3.2 Analytical and empirical approaches for tapered piles

The unique geometry of tapered piles necessitates specific design approaches that differ from those used for cylindrical piles. Standard design codes such as API (2014) and Eurocode 7 are generally developed for piles with uniform cross-sections and are not directly applicable to tapered geometries. To address this question, El Naggar and Wei (1999) introduced a taper correction coefficient K_t to modify the determination of shaft resistance of displacement piles according to the beta (β) method. They proposed average unit shaft resistance along the tapered pile in the following form:

$$\tau_f = K_t . K \bar{\sigma}_{v0} tan(\delta_{cv}) \qquad 3.10$$

where K is the lateral earth pressure coefficient at failure, $\bar{\sigma}_{v0}$ is the average effective vertical stress along the shaft, δ_{cv} is the constant volume pile–soil interface friction angle, and K_t is the taper correction coefficient, defined as:

$$K_t = \frac{unit\ shaft\ friction\ of\ tapered\ pile}{unit\ shaft\ friction\ of\ straight\ pile}$$

The proposal was supported by Naggar and Sakr (2000) using centrifuge tests to investigate the relationship between taper angle, effective vertical stress, and the taper correction coefficient (K_t). K_t increases nonlinearly with taper angle and decreases with increasing effective vertical stress (Figure 3.8).

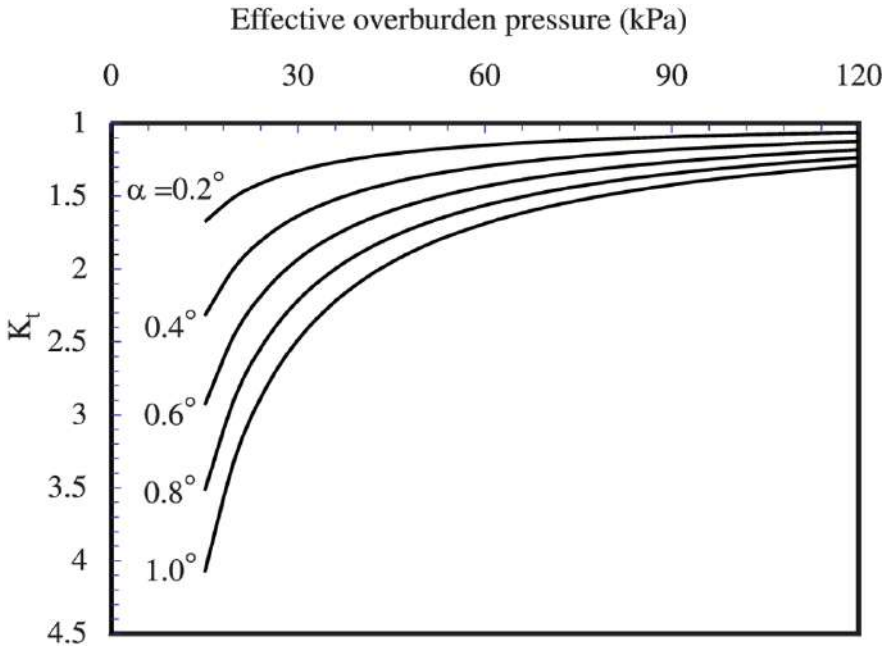

Figure 3.8: Variation of taper correction coefficient (K_t) with effective overburden pressure for different taper angles (Naggar & Sakr, 2000)

Further developments in empirical methods for non-displacement piles were made by Lee et al. (2009), who proposed a design method based on Cone Penetration Test (CPT) data. Their method estimated the base and shaft resistances of tapered piles. The base resistance q_b and shaft friction q_s were defined as:

$$q_b = c_b . q_{c\,avg} \tag{3.11}$$

$$q_{si} = c_{si} . q_{ci} \tag{3.12}$$

where $q_{c\,avg}$ is the average cone tip resistance, q_{ci} is the local cone tip resistance at depth i, and c_b and c_{si} are CPT correlation factors for base and shaft resistances, respectively. Different research proposed the values of c_b and c_s for non-displacement piles in sand. For example, Aoki and Velloso (1975) proposed the value of c_b as 0.28-0.30 and c_s as 0.002.

To account for taper effects, Lee et al. (2009) introduced taper influence factors TF_b and TF_S to modify the base and shaft resistances:

$$q_b = TF_b . c_b . q_{c\,avg} \tag{3.13}$$

$$\tau_s = TF_s . c_{si} . q_{ci} \quad (3.14)$$

The taper effect factor for base resistance (TF_b) was expressed as:

$$TF_b = \left[\frac{1}{c_b} - \left(\frac{1}{c_b} - 1\right) B_R^{0.12}\right] I_{b,D_R} I_{b,K_0} \quad (3.15)$$

where B_R is the diameter ratio between pile base and head, and I_{b,D_R}, and I_{b,K_0} are taper influence factors related to relative density D_R and lateral earth pressure coefficient K_0:

$$I_{b,D_R} = 1.41 - 0.0074 D_R$$

$$I_{b,K_0} = 1 + 0.884\ (K_0 - K_{0,NC})$$

The taper effect factor for shaft resistance is given by:

$$\begin{cases} TF_S = [1.3 + 0.33(\alpha - 1)\ (5.945 - 0.057 D_R)] I_{s,K_0} & for\ \alpha > 1^0 \\ TF_S = [1 + 0.3\alpha\ ] I_{s,K_0} & for\ \alpha \leq 1^0 \end{cases} \quad (3.16)$$

Where $I_{s,K_0} = 1 - 0.33\ (K_0 - K_{0,NC})$ and α is the taper angle. K_0 is the coefficient of lateral earth pressure at rest, and $K_{0,NC}$ represents the at-rest earth pressure coefficient for normally consolidated soils.

More recently, Paik et al. (2013) advanced the empirical framework by proposing modified taper effect factors for base and shaft resistance, explicitly considering the soil relative density and in situ earth pressure coefficient for non-displacement piles. Their approach introduced the following expressions:

$$TF_b = 1 + [0.0005 (D_R)^{1.5} \ln(K_0) + 0.359]\alpha \quad (3.17)$$

$$TF_s = 1 + [6.3 - 22.6 \ln(K_0)] \frac{\alpha}{D_R} \quad (3.18)$$

where D_R is the relative density of sand, α is the taper angle of the pile and K_0 is the earth pressure coefficient at rest.

3.3.3 Literature on tapered piles

Field tests

Rybnikov (1990) conducted field investigations to evaluate the bearing capacity of bored-cast-in-place tapered piles under vertical compressive loading. The study compared the performance of two tapered piles with cylindrical piles of the same length that were installed in cohesive non-saturated soils. The tests revealed that tapered piles exhibited a 20–30% higher specific bearing capacity compared to cylindrical piles due to the wedge effect, which enhanced shaft friction. The most effective taper angle was determined to be 2.4° which achieve the optimal balance between material efficiency and bearing capacity.

Zil'berberg and Sherstnev (1990) conducted a field study on the construction and performance of compaction-tapered piles. The study examined the economic and structural advantages of using tapered piles of 3m length a top section of 70 × 70 cm, and a bottom section of 10 × 10 cm in comparison to traditional prismatic piles. Field tests were conducted under static loading conditions shows tapered piles has 2.5 to 3 times higher bearing capacity compared to cylindrical piles. The study highlighted the compaction effect of tapered piles, which improved soil densification around the pile shaft, thereby increasing load resistance. The results confirmed the economic benefits of tapered piles, reducing material consumption, reinforcement requirements, and installation time, making them an efficient and cost-effective alternative in weak soil conditions.

Horvath et al., (2004) conducted a case study on the performance of tapered driven piles at John F. Kennedy International Airport over 50-year under static load testing. The study showed that tapered piles significantly improved axial-compressive capacity, with service-load capacities exceeding 1780 kN and ultimate capacities reaching 4450 kN.

Khan et.al (2008) conducted full-scale static load tests to evaluate the axial compressive capacity of drilled concrete tapered piles in cohesive-frictional soil. The study compared four tapered piles (0.95° to 1.91°) with two straight-sided piles, all of which were cast-in-place. The load-bearing capacity was up to 50% higher than straight piles of equal volume. The research introduced a taper coefficient (K_t) to quantify the effect of tapering on shaft resistance, which correlated well with experimental results. The findings confirmed that tapered piles exhibit stiffer load-settlement responses, resist plunging failure, and achieve greater axial capacity, making them a viable alternative to straight-sided piles in similar soil conditions.

Tavasoli and Ghazavi (2020) conducted field tests to evaluate the drivability and performance of tapered, cylindrical, and semi-tapered (hybrid) steel piles in poorly graded sand. The study included tapered piles (2.5 m long, top diameter 0.212 m, bottom 0.115 m), cylindrical piles (0.162 m), and semi-tapered (hybrid) piles combining tapered and cylindrical sections. The piles were driven using a 2.95 kN hammer with a drop height of 1 m. The results revealed that tapered piles required 36% fewer hammer blows compared to cylindrical piles, showing improved penetration efficiency by 25–60%. Additionally, semi-tapered piles showed intermediate performance between tapered and cylindrical piles, confirming the material efficiency and drivability advantages of tapered piles in sandy soils.

Experimental studies

Robinsky et al. (1964) conducted experiments on model piles to evaluate the effect of shape and volume on the capacity of model piles in loose and medium-dense sand. The study compared the performance of tapered piles with straight-sided piles of the same volume installed in Ottawa sand. The result shows that tapered piles required 50–64% less material than straight piles to achieve the same bearing capacity. Tapered piles transferred 80–85% of the load through shaft friction, while straight piles relied more on point resistance, transmitting only 45–65% of the load through the shaft.

Naggar and Sakr (2000) performed a series of centrifuge tests at 10g to evaluate the axial compressive performance of tapered piles compared to cylindrical piles in loose sand. Twelve model piles with varying taper angles were tested, including both instrumented and non-instrumented specimens. The results showed that tapered piles achieved up to 88% higher bearing capacity than cylindrical piles of the same length and average diameter. Shaft resistance accounted for the majority of the load, especially in piles with greater taper angles. Skin friction values for tapered piles were approximately twice those of cylindrical piles, and stiffness increased by up to 90%.

Suits et al. (2003) used centrifuge modelling to compare the axial performance of tapered and cylindrical piles driven into loose sand. Twelve open-ended model piles with varying geometries were installed at 1g, and the loading tests were conducted at 10 g. Their results showed that tapered piles mobilized significantly higher shaft resistance, up to 185% greater than cylindrical piles.

Sakr (2004) used centrifuge modelling to investigate the axial performance of fibre-reinforced polymer (FRP) composite tapered piles embedded in dense sand. They tested cylindrical and tapered piles with taper angles of 0.53°, 0.71°, and 1.13. Testing was done under two confining pressure levels simulating pile segments at 4 m and 8 m depths. The results showed that axial capacity increased with taper angle, with the steepest tapered pile (1.13°) achieving up to 156% higher capacity than the cylindrical pile under low pressure, and up to 233% higher under high pressure.

Paik et al. (2007, 2011) investigated the axial behavior of non-displacement tapered piles compared to cylindrical piles in medium and dense sand using model tests in a calibration chamber. The tapered piles had a length of 900 mm, with a top diameter of 71 mm and a bottom diameter of 46 mm, while cylindrical piles had a uniform diameter of 60 mm. The results showed that tapered piles exhibited higher shaft resistance than cylindrical piles, as shaft

friction continuously increased with settlement, whereas cylindrical piles reached ultimate resistance at 4% pile diameter settlement.

Shabanpour and Ghazavi (2022) conducted a series of centrifuge tests at 30g to compare the axial behavior of uniform and tapered piles with circular, square, and X-shaped cross-sections. A total of 12 static tests, six under compression and six under tension, were performed using fully instrumented model piles driven into dry silica sand. The results show that tapered piles exhibited at least 40% greater compressive capacity than their uniform counterparts of equal volume and length. Under tensile loading, tapered piles showed uplift capacity of about 15% more than that of a similar uniform pile.

3.4 Installation-induced effects

3.4.1 Stress redistribution

The installation of displacement piles significantly changes the in-situ stress conditions of the surrounding soil. As the pile penetrates the ground, it displaces soil both horizontally and vertically, increasing radial stresses. These change in stress due to pile installation depends on the position of the soil element with respect to pile movement (Jardine et al., 2013)

Contact stresses

Lehane and White (2005) conducted a series of centrifuge experiments using instrumented displacement piles to investigate lateral contact stress development in sand. Their study investigated the effects of different installation methods on stress mobilization and shaft friction. They have also compared lateral effective stresses recorded while the pile was moving during installation (σ_{hm}) with stresses recorded during stationary pauses (σ_{hc}) at various depths. Figure 3.9 shows the lateral stresses measured at various normalized depths (h/B) during both the moving (σ_{hm}) and stationary (σ_{hc}) stages of installation.

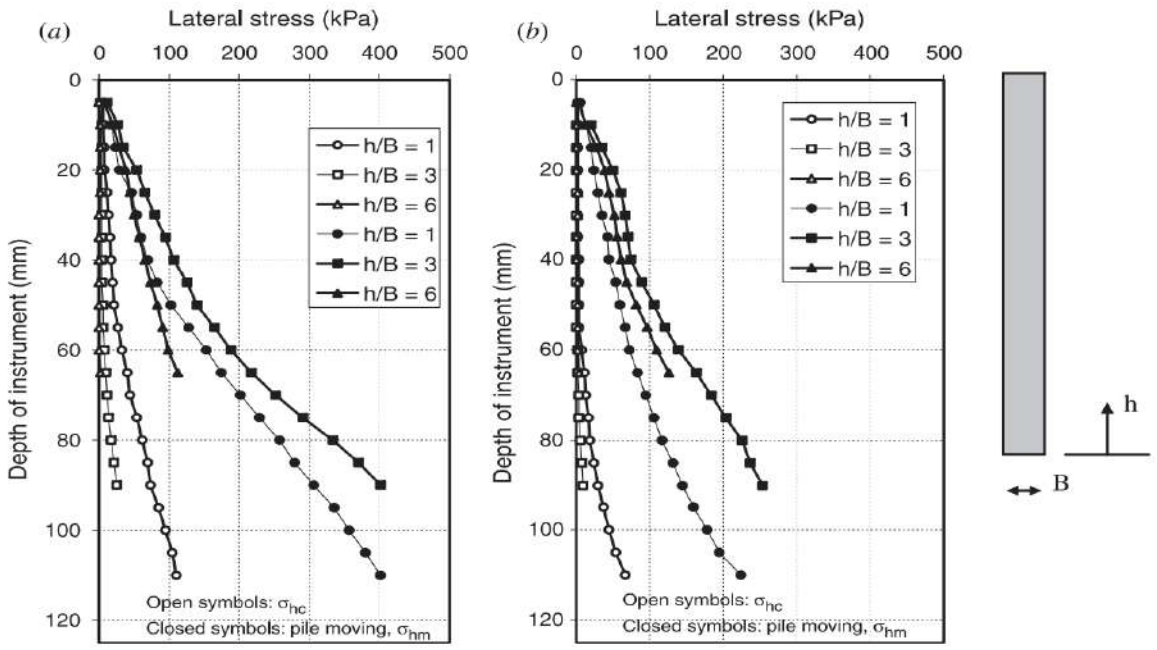

Figure 3.9: Lateral stress development during pile installation using (a) jacking and (b) pseudo-dynamic (Lehane & White, 2005)

They have also computed the ratios of lateral stress increases measured during installation ($\Delta\sigma_{hi}$) against normalized depth (h/B) for different shapes of the models (width to breadth ratio W/B). Figure 3.10 shows the lateral stress change ($\Delta\sigma_{hi}$) measured for each 2 mm penetration increment during jack installation. The results indicate that for an elongated cross-section (W/B = 6) of the model, the increase in lateral stress during pile penetration is more than twice lower than in the case of a square section, with a higher normal stiffness of the interface. One can expect that the lateral stress increase in plane strain conditions is lower than for axisymmetric or prismatic one. This effect of pile shape attenuates with penetration (h/B).

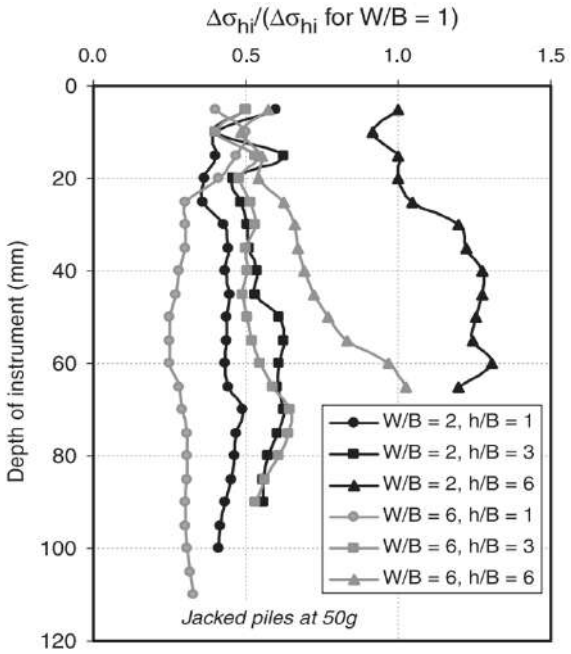

Figure 3.10: Installation-induced stress increase for different pile aspect ratios (W/B) normalized by the stress increment for W/B=1 (Lehane & White, 2005)

Stresses in the soil mass

Installation-induced stress change has been extensively studied through a range of physical modeling techniques. Allard (1990) conducted a centrifuge test to investigate the stress fields from impact-driven pile installation in dry sand. Using pressure transducers embedded in the soil mass, he measured radial and vertical stress in the soil as the pile penetrated. The results showed that stress redistribution occurred as sharp, localized peaks when the pile tip approached the sensor depth, followed by rapid decay as it passed (Figure 3.11).

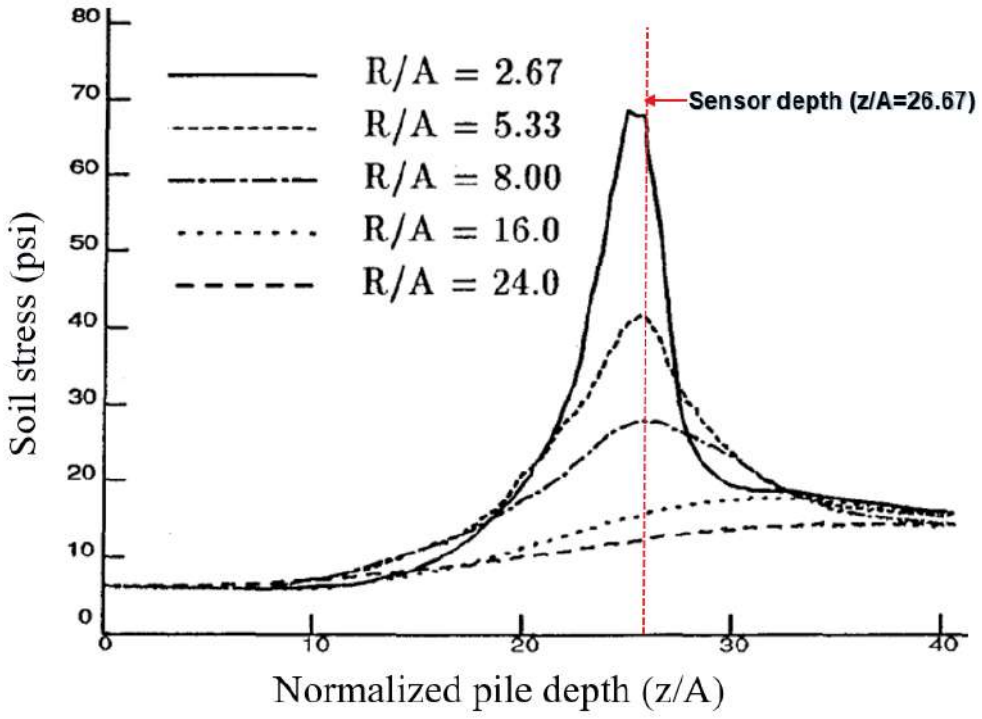

Figure 3.11: Radial stress distribution with normalized pile depth: z is penetration depth, R is radial distance of soil element, and A is pile diameter (Allard, 1990)

Jardine et al. (2013a, 2013b) performed a series of instrumented calibration chamber tests using Mini-ICP piles and measured effective vertical, radial, and circumferential stresses. The results showed that radial and vertical stresses increase as the pile tip approaches, reaching maximum values near the pile shaft and tip, and then decline rapidly as the pile passes below a given sensor depth. This confirms that stress development is governed by the relative position of the pile tip (h/R) and the distance from the pile axis (r/R). They also showed that radial effective stress increases were up to 95% higher at r/R = 3 than those recorded in stationary phases at the same location. Stress changes are significant, especially within the zone within 2–3 pile radii from the shaft. Measured radial stress variations with depth at different distances from the pile are shown in Figure 3.12, and their normalized values are shown in Figure 3.13.

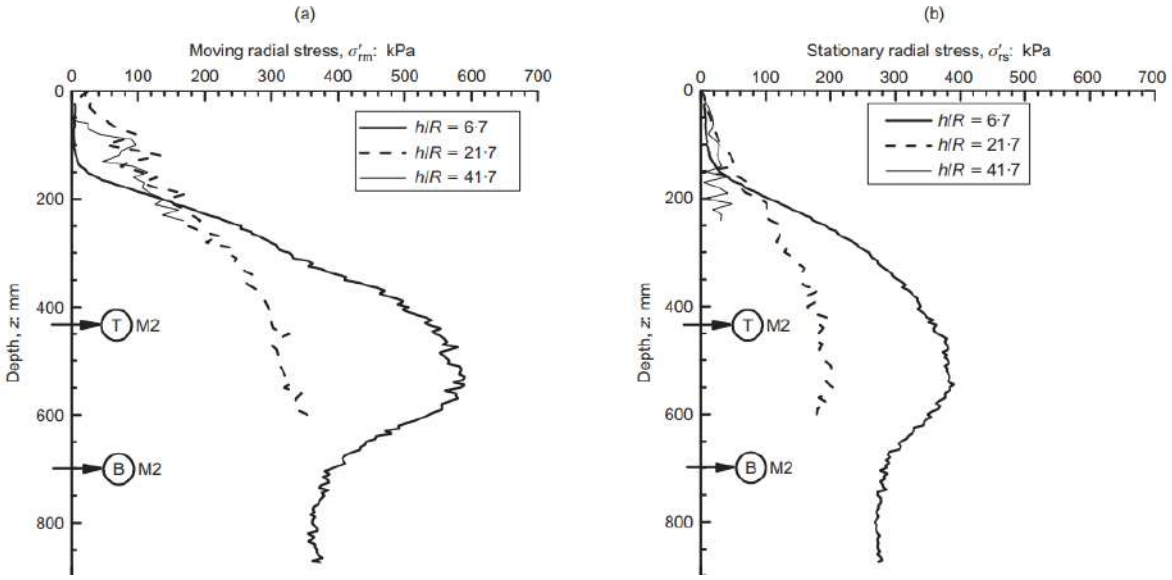

Figure 3.12: Radial effective stress measured during pile a) moving and b) stationary (Jardine et al., 2013)

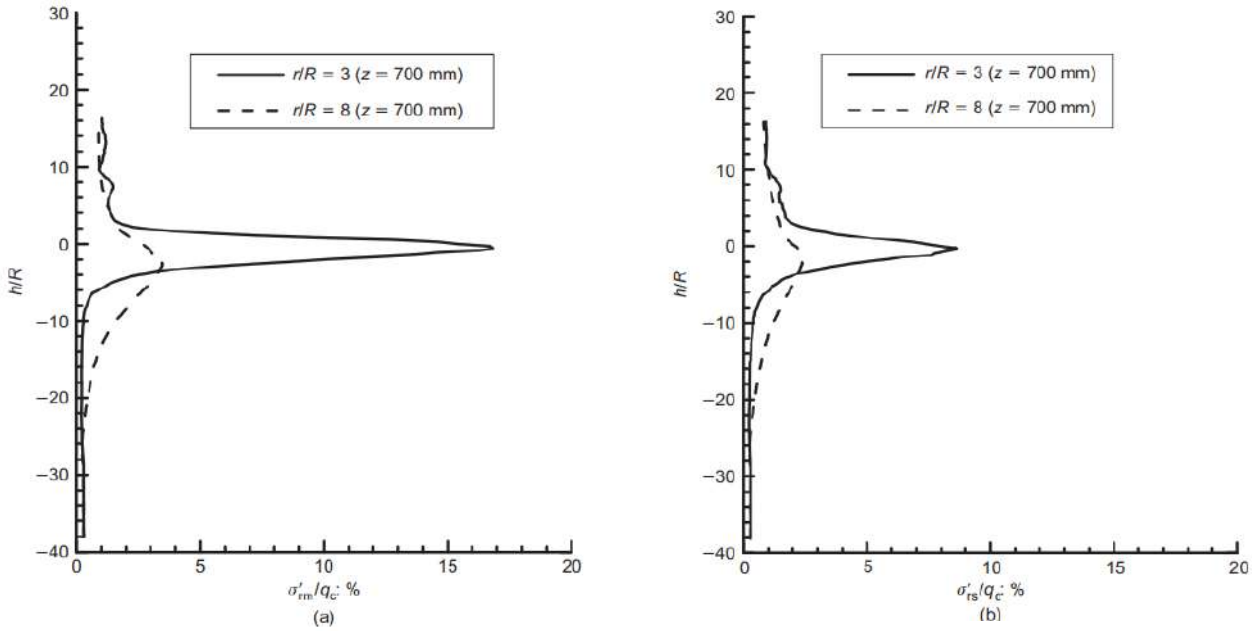

Figure 3.13: Normalized radial effective stress measured during pile a) moving and b) stationary (Jardine et al., 2013)

Yang et al. (2014) conducted centrifuge model tests to further investigate the stress mobilization around displacement piles during installation in dense Fontainebleau sand. They measured total radial stresses at various radial distances (r/R) and depths (h/R) relative to the pile. They observed high stress concentrations near the pile tip during installation, with the

maximum radial stress in the soil mass exceeding 16% of cone resistance (q_c) at h/R = 0.5 and r/R = 2. The stress increases were most pronounced at mid-depth of the shaft ($-5 < h/R < 3$) (Figure 3.14).

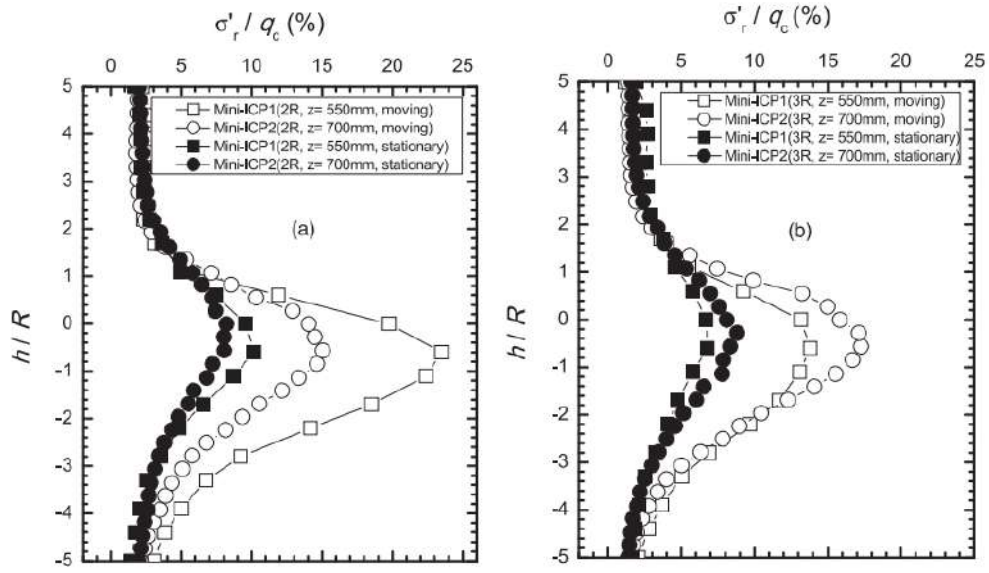

Figure 3.14: Radial stress change along pile depth during jack installation in dense sand (Yang et al., 2014)

D'Arezzo et al. (2015) investigated the evolution of horizontal stresses during the jacked installation of a displacement pile in quartz sand using a centrifuge test at 50g. They used pressure gauges placed both within the soil mass and along a pre-installed instrumented square pile. Figure 3.17 illustrates the variation of the normalized horizontal stress increment ($\Delta\sigma_h/q_b$) against the normalized depth of the pile tip (h/R). Symbols represent null gauges on the pile (NG-P_{147}, NG-P_{97}) mounted on the pile at 147 mm and 97 mm from the pile tip, respectively, and in the soil (NG-S_{90}, NG-S_{150}) embedded in the soil at 90 mm and 150 mm below the ground surface, respectively.

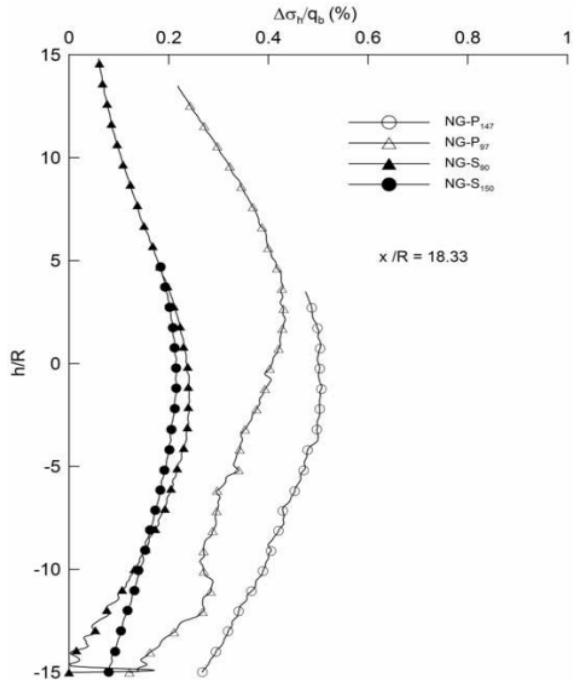

Figure 3.15: Increment of horizontal stress ($\Delta\sigma_h$) and the pile base stress (q_b) versus the normalised depth of the pile tip (h/R) (d'Arezzo et al., 2015).

The results showed that the maximum horizontal stress increment was approximately 0.5% of the pile base stress. Their results revealed that horizontal effective stress increases occurred sharply as the pile tip approached each sensor depth ($h/R \approx 0$), followed by a rapid decline as it passed, which is consistent with Jardine et al. (2013) and Yang et al. (2014). Additionally, the study found that the peak pressures recorded by gauges installed on the measurement pile were substantially greater than those recorded within the surrounding soil.

Yang et al. (2020) conducted a numerical analysis of radial stress behavior during pile installation in dense sand. Figure 3.16 shows the variation of radial stress with normalized distance r/R at h/R=0.5, and compares the numerical results with calibration chamber experiments of Jardine et al. (2013). The results confirm that radial stress peaks very close to the pile shaft and decays rapidly with distance. Both the numerical simulations and experimental data demonstrate strong near-field stress concentrations.

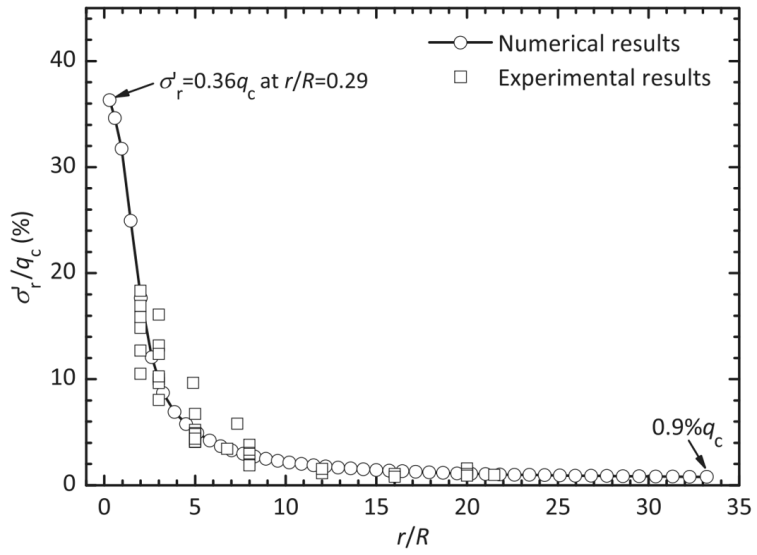

Figure 3.16: Variation of radial stress with normalized radial distance r/R at h/R=0.5 (Yang et al., 2020).

Talesnick and Omer (2024) measured stress around a monotonically installed model pile and cone penetrometer using pressure sensors. The installation was performed under drained conditions in dry sand at a constant penetration rate of 0.1 mm/s. Results showed that vertical stresses increased significantly ahead of the pile tip and decreased radially outward, while horizontal stresses increased near the shaft, indicating radial compaction. After the base has passed the sensor level, the horizontal stress decays to the level prior to the penetration end.

3.4.2 Soil displacement

Robinsky & Morrison (1964) experimentally observed that radial displacement of sand during pile driving leads to significant densification and lateral stress increase around the pile, with the densified zone typically extending up to 3 to 5 pile radius from the shaft.

More recent advancements in image-based techniques, including DIC and PIV, have been used for detail visualization and quantification of soil displacement patterns. For instance Arshad et al. (2014) conducted a series of cone penetration tests in silica sand using DIC within a half-circular calibration chamber to study the deformation mechanisms around the cone. The chamber was equipped with transparent observation windows and high-resolution cameras to

capture soil movements during penetration. The tests involved three types of silica sand with varying particle crushability and were performed at different relative densities and surcharge pressures. They have identified four distinct displacement zones during penetration: (I) vertical compression beneath the cone, (II) a crushed particle band along the cone shaft, (III) a transition zone of displacement vector rotation, and (IV) radial displacement zone, see Figure 3.17. Soil elements just beneath the cone tip (zone I) exhibited maximum normalized vertical displacement increments of up to 0.68 r_c for the least crushable sand, where r_c is the cone radius. In the transition zone (zone III), radial and vertical displacement increments ranged from 0.12 to 0.16 r_c , while in the outer region (zone IV), displacements decreased to less than 0.02 r_c .

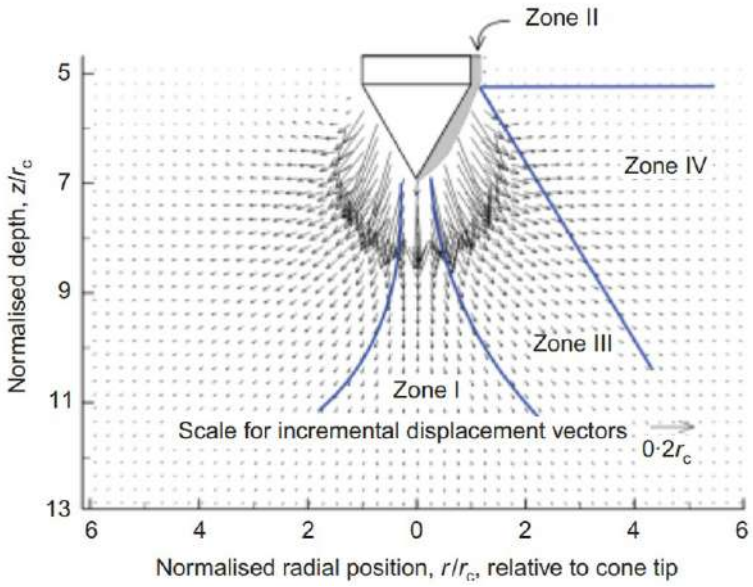

Figure 3.17: Characterization of displacement zones near cone during a penetration (Arshad et al., 2014)

Tehrani et al. (2018) employed calibration chamber to study cone penetration in layered silica sands. They investigated the effect of interface between different sand layers on cone resistance and soil deformation. Using DIC, they measured soil displacement and strain fields near the cone tip during penetration. Figure 3.18 shows normalized radial displacement profiles at a horizontal distance of r =1d_c from the shaft axis, where *dc* is the cone diameter.

They considered different soil layer profiles: T1a-LOD, representing loose sand over dense sand; T2a-DOL, representing dense sand over loose sand; T3-MDOD, representing medium-dense sand over dense sand; and T4-DOMD, representing dense sand over medium-dense sand. The peak normalized radial displacements approach 0.1 to 0.15d_c. In the loose-over-dense profile (T1a-LOD), an increase in radial displacement occurs below the interface depth ($z_{interface} \approx 12.3d_c$). No significant change in the normalized radial displacement profile is observed for other soil profiles.

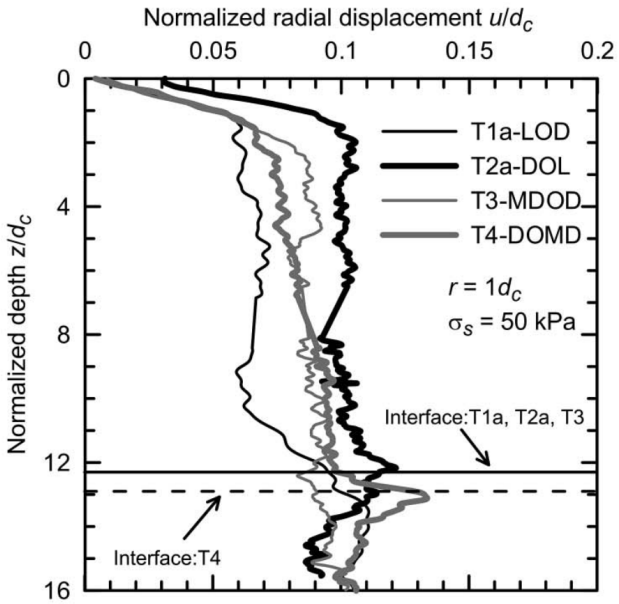

Figure 3.18: Normalized soil radial displacement for different soil layer profiles (Tehrani et al., 2018)

Tovar-Valencia et al. (2021) also used DIC in a calibration chamber to examine the effects of pile base geometry on deformation patterns and base resistance mobilization during model pile penetration tests in dense and medium-dense sands. They analyzed soil displacement and strain fields during and after the installation of two model piles (one with a flat base and another with a conical base having a 60° apex angle). They observed that the conical base has a different deformation pattern below the pile with strain concentration in a narrower vertical zone compared to the flat base. They also observed that both jacked and preinstalled piles with

conical bases developed lower base resistance than those with flat bases under identical conditions. The study also quantified that, at relative displacements of 10% of the pile diameter, the resistance ratio for conical to flat base piles ranged between 0.64 and 0.78, increasing to 0.70–0.84 at greater displacements.

Particle Image Velocimetry (PIV) has also become a standard tool for visualizing soil displacement fields in the model pile**.** White and Bolton (2004) conducted a series of plane-strain calibration chamber tests using PIV to investigate displacement and strain paths around a jacked model pile in sand. Soil movement was primarily downward beneath the pile tip and radiated laterally outward, forming distinct zones of compression and extension. The measured horizontal displacement in the far field was 25 μm at a distance of 5B from the pile centerline. This was obtained from PIV analysis of an image taken when the pile penetrates in soil about 1.5 mm depth. Figure 3.19 shows net displacement ratios ($2\Delta x/B$ and $2\Delta z/B$) for a single vertical column of soil elements located at a horizontal offset of 1.15B from the pile centerline. The results, obtained from tests in Dog's Bay carbonate sand (T2-DBS-44) and Leighton Buzzard silica sand (T4-LBS-34), show a steady-state deformation pattern during pile movement. The vertical displacement ratios ($2\Delta z/B$) were generally higher than the horizontal ratios ($2\Delta x/B$), particularly in the carbonate sand, indicating greater downward soil flow. In contrast, horizontal displacement ratios for silica and carbonate sands were quite similar.

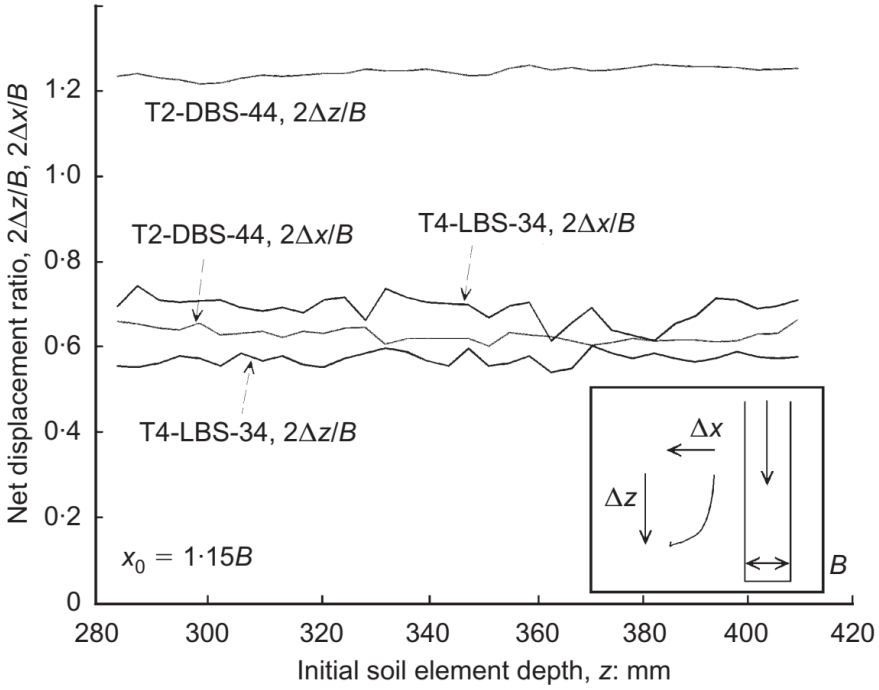

Figure 3.19: Displacement trajectories for the column of soil elements (White & Bolton, 2004).

Liu et al. (2020) used PIV to compare soil movement during penetration of flat-ended and cone-ended piles during pile installation. The results showed that the maximum vertical displacement near the pile shaft was approximately 0.58R for flat-ended piles and decreased to 0.48R for 60° cone tips, where R is the pile radius.

Zhang et al. (2005) applied PIV to measure soil displacements in both 1g and centrifuge (100g) model tests involving uniform clay. Their study aimed to examine the effect of gravity level on soil deformation patterns. The tests were conducted using a plane-strain model setup with a rigid footing penetrating normally and overconsolidated kaolin clay. High-resolution images were captured through a transparent viewing window during and after footing penetration, and the displacement fields were obtained using cross-correlation techniques. The results showed that at 100g, displacement patterns were consistent in form with those observed at 1g, but the magnitude and spatial scale of deformation were significantly reduced. PIV enabled visualization of shear bands and localized failure zones, and the results revealed sharper, more localized deformation under higher gravity.

3.4.3 Influence of installation mode on pile bearing capacity

Fioravante (2002) conducted centrifuge tests to evaluate shaft resistance development in non-displacement piles in sand. The shaft friction depends on the interface roughness. Rough piles mobilized higher shaft resistance due to soil dilation, while smooth piles showed lower resistance due to interface sliding and soil contraction.

Gavin and Lehane (2003) investigated factors affecting the shaft capacity of open-ended (pipe) piles in sand. They found that the local shaft resistance developed during installation of the shaft of a pipe pile depends on the cone resistance (q_c), relative position of the pile toe (h/R), and the mode of pile penetration during installation. Extending their work, Gavin and Lehane (2007) investigated factors affecting the mobilization of the base resistance of piles in sand. Their results showed that pile base movement begins when the residual base stress induced during installation is exceeded. Once this happens, a stiff, linear load-displacement response is observed.

Paik and Salgado (2004) used chamber tests to compare the effects of driving versus jacking on the behavior of open-ended pipe piles in sand. Their findings showed that jacked piles developed higher shaft and base resistances.

Blanc and Thorel (2016) investigated the cyclic axial behavior of jacked displacement piles in Fontainebleau sand at a relative density of 92% sand using centrifuge model tests at 23g. El Haffar et al. (2017) further investigated the influence of installation methods on axial pile capacity in dense Fontainebleau NE34 sand using centrifuge tests. They compared the compression test result of piles installed by jacking and wish-in-place. Their results show jacked piles provide higher resistance (three times) than wish in place piles.

Ezzeddine (2024) investigated the effect of installation method on shaft resistance of pile using centrifuge and numerical simulations. She compared monotonic jacking and stroke-based

cyclic jacking in medium dense sand. The result shows that cyclic strokes mobilized higher shaft resistance due to enhanced densification and friction mobilization along the pile–soil interface. Her study also found that continuous jacking produced more uniform mobilized friction across the sand mass and cyclic strokes induced localized high-friction zones. The pullout capacity is higher for the monotonic installation.

3.5 Summary

Installation-induced effects such as stress redistribution, soil densification, and displacement play a significant role in pile performance. The radial and vertical effective stresses around a pile change considerably during penetration, influencing the mobilization of shaft and base resistance. These effects are particularly significant in dense sands, where installation leads to localized densification and lateral stress increase.These support the conclusion that displacement pile installation induces highly non-uniform stress redistribution patterns, and that proper modeling of these effects is important for accurate design and prediction of shaft resistance in dense sands. For a given relative density of the sand, the highest shaft friction during installation is mobilized (Foray, 1991; Lehane & White, 2005) for pushed-in piles, followed by jacked and driven ones.

The performance of tapered piles in model tests is still not well known. The calibration chamber tests were performed only for non-displacement tapered piles. Although many centrifuge studies have focused on cylindrical piles under varied installation and loading conditions, tapered piles have received comparatively limited experimental attention (Naggar & Sakr, 2000; Suits et al., 2003; Sakr & El Naggar, 2003; Shabanpour & Ghazavi, 2022). They were focused mainly on their load-bearing performance. In the previous studies, the displacement tapered piles were, however, installed in 1g conditions, which does not permit the correct physical modelling of stress state and stress/strain changes during the penetration

and static loading of such models. This study aims to fill this gap by investigating and enhancing our understanding of the behavior of tapered piles throughout the in-flight installation process with monotonic pushing and under axial static loading in both compression and tension modes.

CHAPTER FOUR

4. Research methodology

4.1 Introduction

This chapter outlines the research methodology employed to investigate the installation effects and performance of tapered piles in sandy soils. A combined experimental and numerical approach was adopted to comprehensively investigate soil–pile interaction mechanisms during both installation and static loading phases.

The experimental program used geotechnical centrifuge modeling under plane strain conditions for the simulation of representative stress states. Model piles, represented as walls in a two-dimensional configuration, were tested to observe soil response during pile penetration and loading. Throughout this study, the terms *pile* and *wall* are used interchangeably, with *wall* referring to the plane strain representation used in the centrifuge setup.

Numerical simulations were performed to analyze load-displacement behavior and identify failure mechanisms. An overview of the entire research methodology, including both physical and numerical modeling, is summarized in Figure 4.1. The details of each method are described in the following subsections.

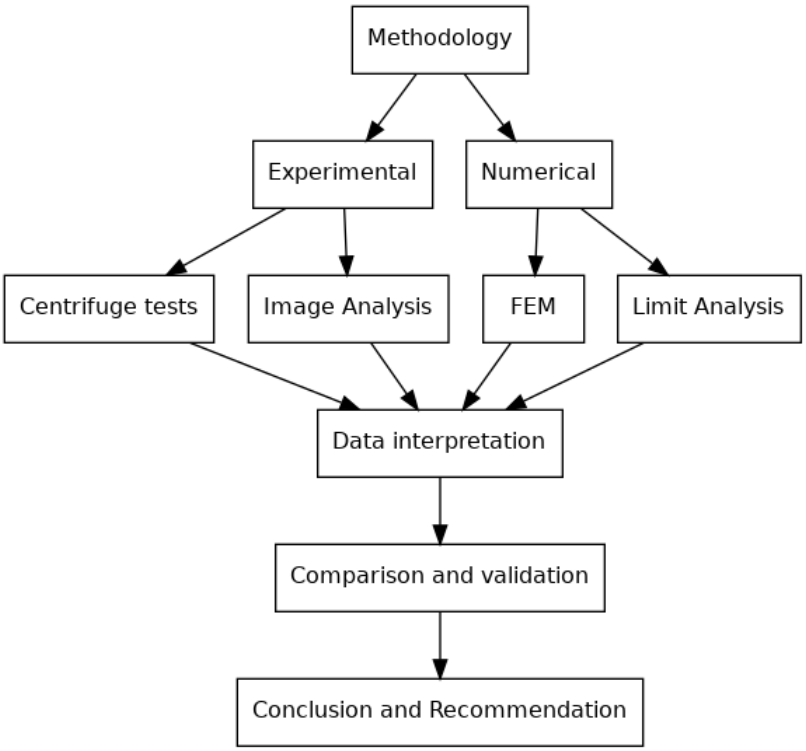

Figure 4.1: Flowchart summarizing the experimental and numerical research methodology.

4.2 Experimental testing using a centrifuge

To investigate the installation effects and behavior of tapered walls in sand, centrifuge modeling was employed as the primary experimental tool. This study was conducted under controlled plane strain conditions at the GERS-CG centrifuge facility at Gustave Eiffel University, using a series of model walls with varying taper angles.

The experimental program included both the installation and static loading phases of the piles to investigate the load-displacement response of pile, and displacement and stress redistribution is soil mass. To capture detailed stress and deformation behavior, the physical models were instrumented with pressure cells embedded in the soil mass and along the model walls. Additionally, high-resolution images were acquired through a transparent container wall during testing for image-based deformation analysis using Particle Image Velocimetry (GeoPIV).

4.2.1 Description of centrifuge facility

The centrifuge tests were conducted at the Geotechnical Centrifuge Facility (GERS-CG Lab) of Gustave Eiffel University in Nantes, France. This centrifuge is designed for advanced geotechnical model testing by replicating prototype stress conditions through high gravitational acceleration, up to 100g. The centrifuge has a 5.50-meter arm radius from the rotation axis to the swinging platform and can carry model payloads up to 2000 kg (Gers-CG, 2023). Table 4.1 summarizes the key technical specifications of the centrifuge. A photo of the centrifuge at the Geotechnical Centrifuge Facility (GERS-CG Lab) of Gustave Eiffel University in Nantes, France, is shown in Figure 4.2. As part of the Horizon Geolab (2021) European research infrastructure project, a series of tests were performed to investigate the behavior of straight and tapered model walls under controlled plane strain conditions.

Table 4.1: Specifications of the Centrifuge at Gustave Eiffel University (Gers-CG, 2023)

Description	Value
Distance axis to swinging basket	5.50m
Centrifuge room diameter	13.50m
Centrifuge room height	3.90m
Payload length	1.40m
Payload width	1.15m
Free height	1.50m
Max. weight model	2000 kg
Max. acceleration (@ 5 m)	100 x g
Max. inbalance	+/- 100kN

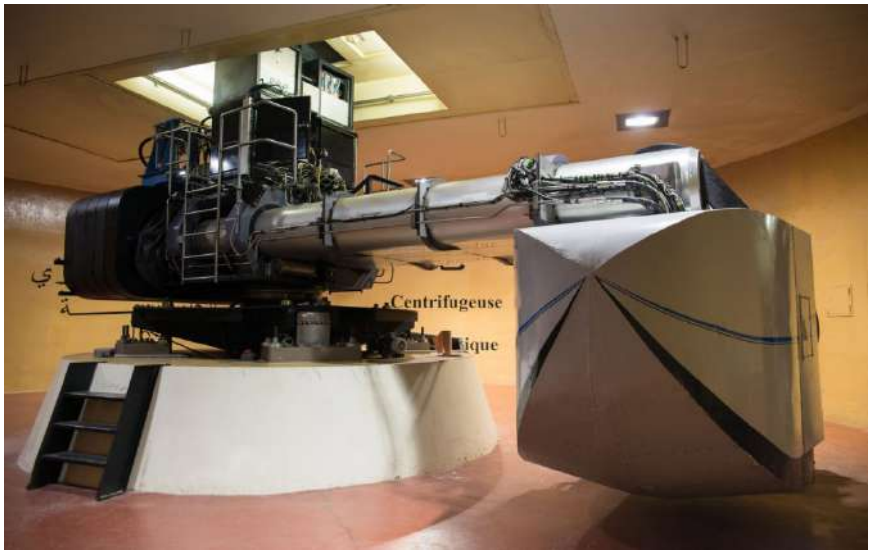

Figure 4.2: Photo of the Centrifuge of Gustave Eiffel University, Nantes (Garnier et al., 2007)

4.2.2 Scaling laws

In this study, a geometric scale of 1:25 was adopted, and the experiments were conducted under a centrifugal acceleration of 25g. Consequently, a model wall embedment depth of 224 mm corresponds to approximately 5.6 meters at prototype scale. To ensure consistency between model and prototype behavior, key parameters such as stress, strain, displacement, and loading rates were scaled according to established centrifuge scaling laws (Garnier et al., 2007). Table 3.2 summarizes the primary scaling factors used in this thesis.

Table 4.2: Summary of scaling laws used for this thesis

Physical Quantity	Scaling Law	Scale at N=25
Length (L)	1/N	1/25
Stress (σ)	1	1
Density (ρ)	1	1
Strain (ε)	1	1
Force (F)	$1/N^2$	1/625
Acceleration (a)	N	25
Displacement (u)	1/N	1/25

Special attention was given to minimize scale effects associated with grain size, especially for modeling the interaction between sand and the small model wall (Bałachowski, 2006). In this study, the smallest base breadth was 10 mm, and the mean grain size (d_{50}) of Fontainebleau NE34 sand was 0.2 mm, resulting in a base width to grain size ratio of 50. According to Garnier et al. (2007), a minimum ratio of 35 between pile diameter B and d_{50} should be respected to reduce size effects. In this study, this criterion was met. Furthermore, considering the smooth surface of the models, the grain size effects on both base and shaft resistance are considered negligible (Foray, Balachowski, & Colliat, 1998).

4.2.3 Physical models

Model sand

Fontainebleau NE34 sand was selected for the tests due to its well-characterized, uniform properties. Table 4.3 summarizes the key geotechnical properties of the sand used in this study.

Table 4.3: Properties of model sand (Beroya-Eitner et al., 2022)

Descriptions	Value	Unit
Soil name	Fontainebleau NE 34	
Relative density	0.68	-
Bulk density	1620	kg/m3
Critical friction angle (ϕ_c)	31.5	degree
Median diameter (d_{50})	0.210	mm
Coefficient of uniformity (C_U)	1.6	-

The sand was placed using the air pluviation (sand raining) method to achieve a target relative density of approximately 68%. The process was paused at designated layers to allow sensor placement (see Figure 4.3a). The final dry unit weight after centrifuge tests, confirmed by calibrated sampling boxes, averages 1620 kg/m³. Photographs taken during the sand raining process and after the completion of sand placement are shown in Figure 4.3.

(a) (b)

Figure 4.3: Model sand preparation (a) sensor placement and (b) the prepared soil in the container

Model walls (quasi 2D pile)

Three quasi-2D piles (walls) of different taper angles were fabricated from Aluminium 5083. The walls included one with a constant cross-section (S) and two with tapered profiles (T1 and T2), as detailed in Table 4.4**.** Each wall consists of two plates, and between each plate, three stress sensors are placed at three levels. At the end of penetration, these walls were all embedded to a depth of 224 mm, resulting in a slenderness ratio (L/B) of 14. The geometrical details of all three model walls are illustrated in Figure 4.4.

Table 4.4: Description and dimensions of model walls

Wall ID	Taper Angle (degree)	Bottom breadth (mm)	Top breadth (mm)
S	0	16	16
T1	0.75	13	19
T2	1.5	10	22

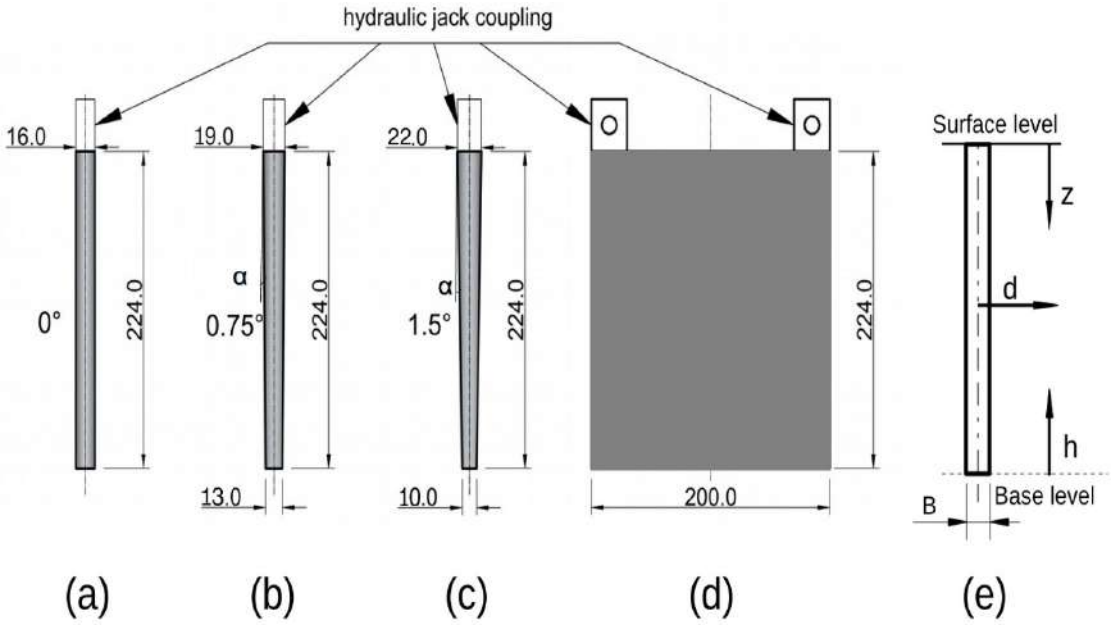

Figure 4.4**.** Model walls: (a) standard (S), (b) tapered (T1) with 0.75° taper angle, (c) tapered (T2) with 1.5° taper angle, (d) side view of the model wall, and (e) definition of quantities related to model walls. All dimensions in [mm]. α is the taper angle.

Container dimensions

The container was designed to simulate plane strain conditions for capturing real-time image-based observation. The internal dimensions of the container are 800 mm in length, 467 mm in height, and 200 mm in width. The container was filled with dry sand to a height of 450 mm. The front face of the container was made from 65 mm-thick transparent plexiglass. The other side of the container was made from rigid steel. Figure 4.5 shows a schematic of the model container. The width of the model was tigtly adjusted to the container in order to avoid the grain trapping between the model and the transparent wall. The effect of boundaries have been checked and to be no effect in our case based on Gui et al. (1998) recommendation.

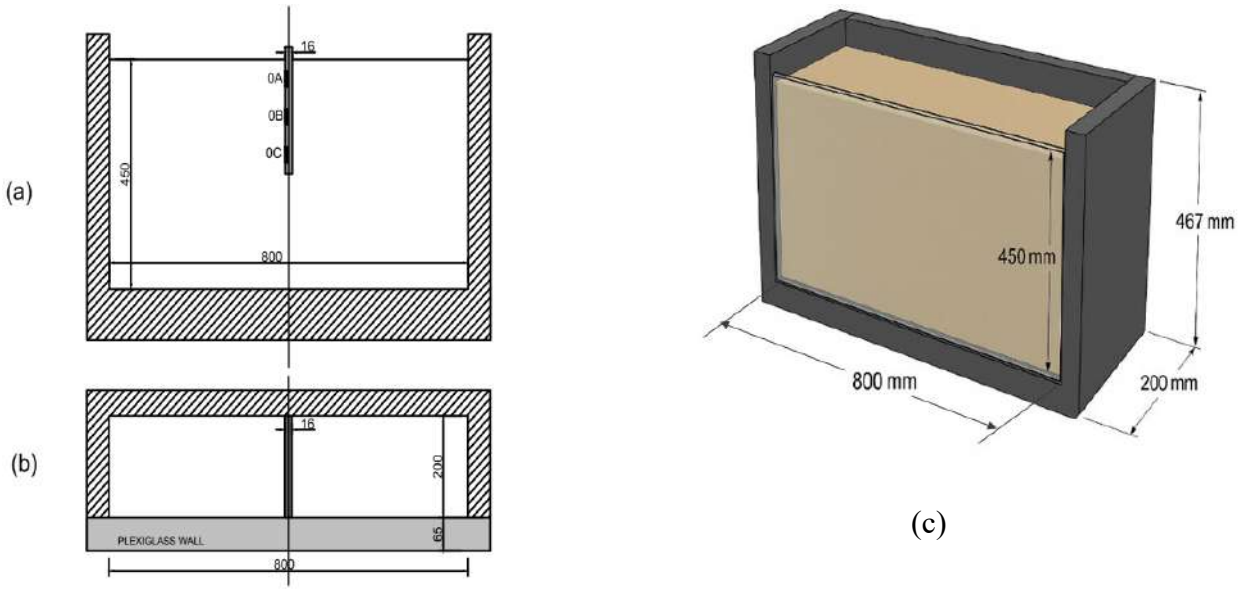

Figure 4.5: Schematic of the container with straight wall, a) 2D cross section, b) 2D plan, and c) 3D layout (not on scale)

4.2.4 Experimental setup

Instrumentation in soil and wall

The arrangement of the earth pressure sensors within the soil mass and the positions of the normal stress sensors along the wall are shown in Figure 4.6. The figure includes vertical and horizontal cross-sections of the setup and shows sensor locations relative to the wall and container. Instrumentation was installed within the soil mass and along the wall surface to measure contact stresses and soil stress redistribution during wall penetration. Five horizontal earth pressure cells were embedded within the sand mass at two predefined depths. Two sensors were placed at Level B (112 mm below the surface), and three sensors were installed at Level C (186.5 mm depth) at 2B, 4B, and 6B from the predefined wall axis.

Each model wall was also fitted with three normal stress sensors (0A, 0B, 0C) mounted along its shaft. Additionally, an axial load cell at the wall head monitors the total load throughout the installation and static loading phases.

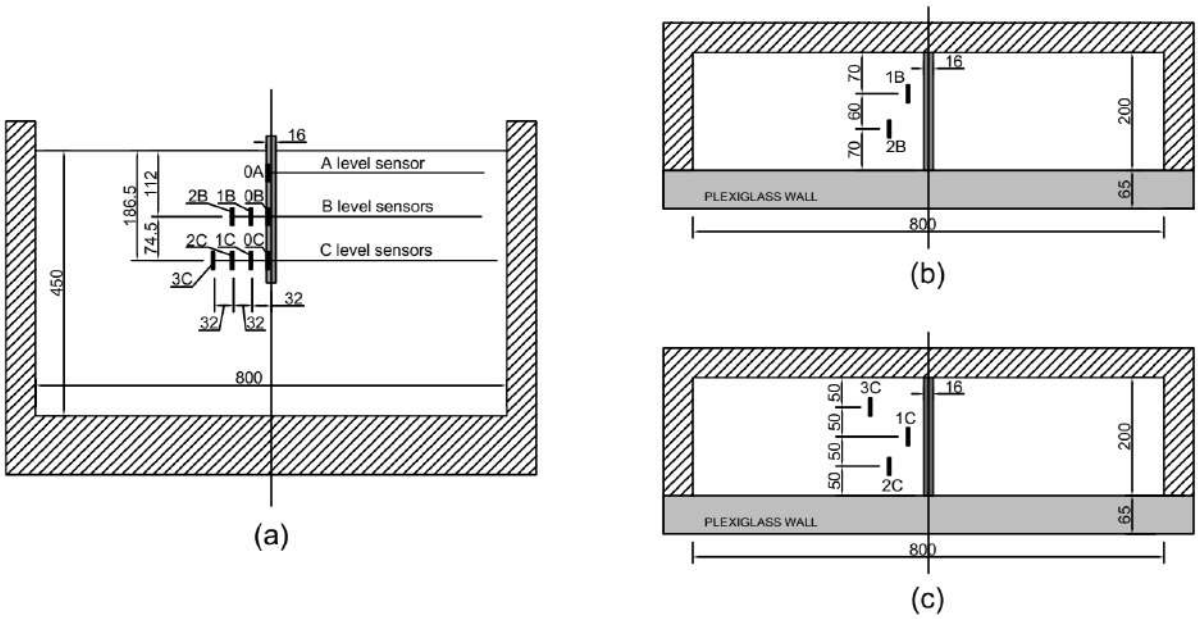

Figure 4.6: Layout of instrumentations: (a) vertical section view, (b) plan section at B-level, and (c) plan section at C-level. All dimensions in [mm].

Image acquisition (camera) setup

To track soil displacement during wall penetration, a high-resolution 12-megapixel CMOS camera (acA4112-8gm) was positioned 300 mm in front of the transparent face of the model container, as shown in Figure 4.7. The camera was carefully aligned to capture sequential images throughout the installation phase. The lighting system was designed to provide uniform illumination, reduce glare, and enhance contrast along the transparent observation face of the container.

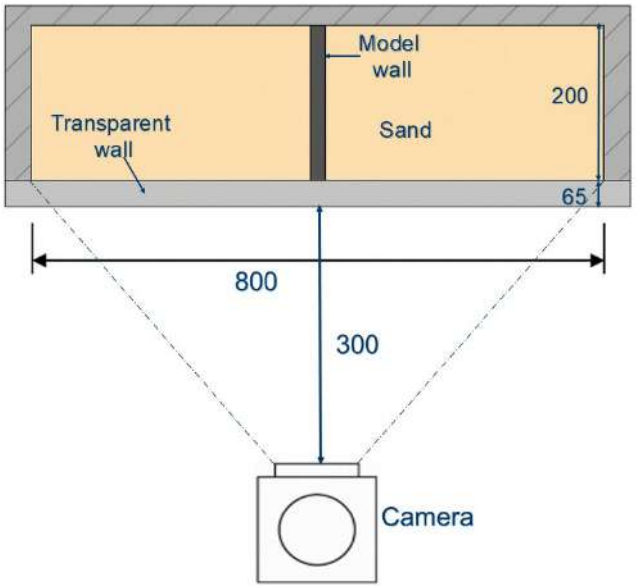

Figure 4.7: Camera setup for image acquisition. All dimensions in [mm].

Set up assembly and mounting

All components, including the container, embedded pressure cells, normal stress sensors, load cells, and imaging system, were securely assembled to ensure operational integrity under in-flight conditions. The completed experimental setup mounted inside the centrifuge swinging basket is shown in Figure 4.8.

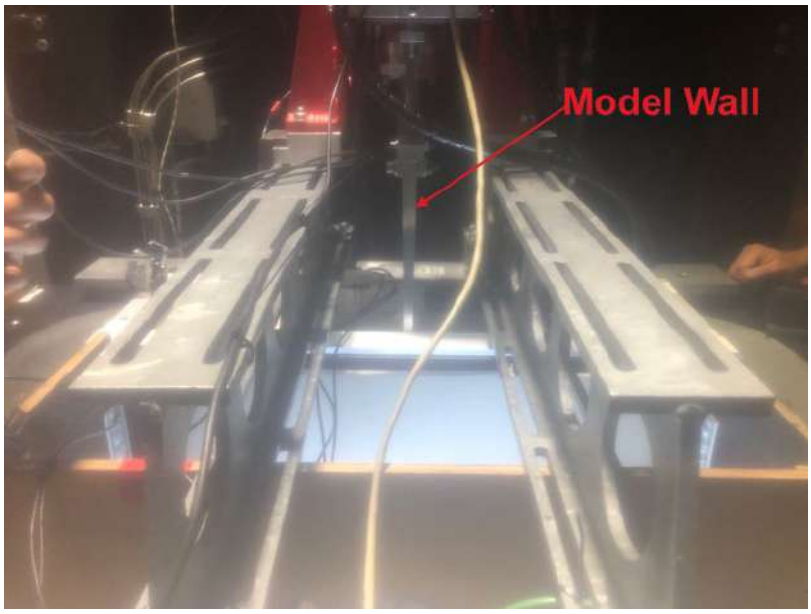

Figure 4.8: Photo of experimental setup mounted in centrifuge swinging basket

4.2.5 Testing procedures

Each experimental test consisted of three phases: (i) soil conditioning at 25g, (ii) monotonic wall installation, and (iii) post-installation static loading. All tests were conducted in-flight under a centrifugal acceleration of 25g to replicate prototype stress conditions. The installation phase involved pushing the model wall vertically into the dense sand at a constant rate of 0.1 mm/s until reaching a target embedment depth of 224 mm. During this phase, axial force and stress data were continuously recorded using a data acquisition system operating at an interval of 0.1 seconds. Simultaneously, sequential images of the soil domain were captured through the transparent sidewall using a high-resolution CMOS camera. The camera captured approximately 46 images per test during wall penetration.

Upon completion of the installation phase, a static loading test was conducted to evaluate the load-displacement response of the embedded wall. The wall head was loaded incrementally in compression using the actuator at a reduced rate of 0.1 mm/s to ensure quasi-static loading conditions. The load was applied until the wall displacement reached a magnitude equivalent to its average base breadth (16 mm), after which the wall was gradually unloaded, and a final pull-out test was also performed.

4.3 Image analysis using Particle Image Velocimetry

To analyze soil deformation induced during wall installation and static loading, Particle Image Velocimetry (PIV) was applied to analyze the images captured during the tests. High-resolution images (with a pixel size of approximately 50 μm) were captured through the transparent face of the container during centrifuge testing. These images were later processed to extract displacement and strain data. In this study, the advanced image correlation software GeoPIV-RG, developed specifically for geotechnical applications by Stanier et al. (2016), was used.

4.3.1 Overview of the GeoPIV-RG technique

GeoPIV-RG is a MATLAB-based digital image correlation tool developed for analyzing soil deformation in geotechnical model tests (Stanier et al., 2016). It improves upon the original GeoPIV by using a regular grid of tracking nodes and incorporating first-order subset deformation. This enables accurate measurement of displacement and strain fields with sub-pixel precision. The tool also applies a reliability-guided (RG) tracking approach, which enhances robustness and removes the need for user-defined search zones. It also includes an automatic reference image-updating feature that reduces random walk errors during large deformation analysis. In this study, GeoPIV-RG was used within MATLAB to process images captured through the transparent container wall for a detailed assessment of soil deformation patterns during the wall installation and loading.

4.3.2 Image preprocessing

Prior to analysis, all images underwent standardized preprocessing to ensure consistency and optimize the performance of the correlation algorithm. The sample images were first cropped to isolate the region of interest around the wall–soil interface. Image alignment techniques were then applied to correct for minor shifts or rotations between frames, ensuring a stable coordinate system for tracking. The images were then converted to grayscale to enhance pixel contrast and improve correlation sensitivity. Finally, noise reduction filters were applied to minimize the influence of lighting inconsistencies that could affect patch matching accuracy.

For each test, an image recorded at the beginning of the installation phase was selected as the reference image. All subsequent images were treated as target frames for incremental tracking using the GeoPIV-RG algorithm (Stanier et al., 2016).

4.3.3 Displacement and strain field extraction

Following preprocessing, image sets were analyzed using GeoPIV-RG to extract full-field displacement data. The algorithm tracked a predefined grid of nodes across successive image pairs, calculating the displacement of each node by correlating image patches between the reference and target frames. This produced a displacement vector field, which indicates the magnitude and direction of soil movement throughout the image domain. From these displacement vectors, the horizontal and vertical components of movement were extracted. These displacement components were used to assess soil movements during the installation and loading phases of the test.

In addition to displacements, strain fields were analyzed as the derivatives of the displacement vectors. This allowed for the determination of shear and volumetric strains throughout the observed region. The displacement and strain results obtained from image analysis were then further interpreted. These results were compared for the three model walls with different taper angles to assess the influence of wall geometry on soil deformation patterns. Furthermore, the results were cross-validated with measurements from embedded sensors.

4.4 Numerical modeling approach

Numerical simulations were conducted to further investigate the load-displacement response and failure mechanisms of tapered walls in dense sand. Two numerical techniques were employed: the Finite Element Method (FEM) using OPTUM G2, and Limit Analysis (LA) using LimitState GEO. Both approaches were implemented under two-dimensional plane strain conditions to replicate the geometry and boundary conditions of the physical tests. Simulations were performed for all three wall geometries: a straight-sided wall (S) and two tapered walls (T1 and T2) with taper angles of 0.75° and 1.5°, respectively. The process of model insertion was, however, not modelled and wish-in-place tapered walls were considered in the analysis.

4.4.1 Finite element modeling

The simulations with OPTUM G2 were considered to replicate the model conditions observed in the centrifuge experiments to enable direct comparisons between physical and numerical results. It means that the same stress level was applied to the soil and the model as in centrifuge tests. As a result, the unit weight of the model and the soil was increased 25 times in the calculations. A two-dimensional plane strain model was developed, with geometry, boundary conditions, and loading configured to match the experimental setup. Both upper-bound and lower-bound solutions were computed. The lower bound (or static) solution is based on a statically admissible stress field that satisfies equilibrium and boundary conditions without violating yield criteria (OPTUM Engineering, 2020). It provides a safe estimate of the collapse load, below which failure is not expected. On the other hand, the upper bound (or kinematic) solution relies on a kinematically admissible velocity (or displacement) field that satisfies compatibility and boundary conditions, estimating the maximum load at which failure could occur based on assumed plastic flow mechanisms (OPTUM Engineering, 2020).

Model setup

The numerical domain was defined with dimensions of 800 mm in width and 450 mm in height, consistent with the internal dimensions of the centrifuge container described in Section 3.2. Three wall geometries were simulated: a straight-sided wall (S) and two tapered walls (T1 and T2). All walls were assigned an embedment depth of 224 mm, consistent with the experimental configuration. They were modeled as rigid bodies with-in-place into the soil. It means that no installation effect was considered in the numerical analysis. Standard boundary conditions were applied as illustrated in Figure 4.9.

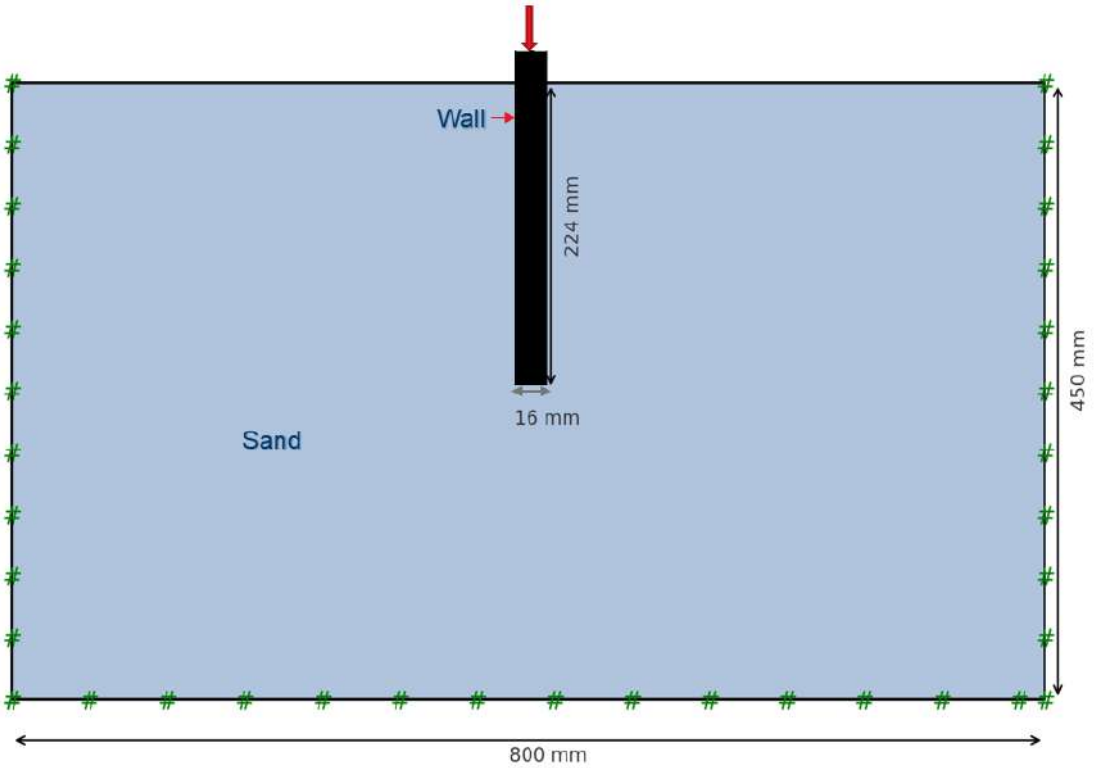

Figure 4.9: Typical model setup for numerical analysis of S-wall

Sand properties and models

Two constitutive soil models available in OPTUM G2 were used to simulate the behavior of Fontainebleau NE34 sand: the Mohr-Coulomb (MC) model and the Hardening Mohr-Coulomb (HMC) model.

The MC model was implemented with both associated and non-associated flow rules. A dilatancy angle of 5° was assigned for the non-associated case. The HMC model accounts for plastic strain development with strain hardening/softening behavior of sands. Taylor flow rule is used. A dilatancy angle of 5.37° and a hardening (fitting) parameter, m=0.5, is used. m value depends on the soil type: for soft clays, m≈1 is recommended, while for sands and other coarse-grained materials, m≈0.5 is appropriate (OPTUM Engineering, 2020).

Soil parameters were adopted from the work of Andria-Ntoanina et al. (2010). To model the interaction between the wall and the surrounding soil, a reduced interface friction angle of 16° was adopted. This value corresponds to the outcome of ring shear tests conducted on a smooth

interface in Geotechnical lab at Gdansk University of Technology. The effect of considering a volumetric dilation cap within the interface was analyzed by assuming a unit value for the dilatancy in the non-associated flow rule of the Mohr-Coulomb (MC) model. A summary of the material parameters used for the MC and HMC models in OPTUMG2 is provided in Table 4.5.

Table 4.5: Properties of Fontainebleau NE34 sand (Andria-Ntoanina et al., 2010)

Property	**MC Model**	**HMC Model**
Young's Modulus (E)	35 MPa	
Friction Angle (φ')	31.5°	31.5°
Cohesion (c′)	0	0
Poisson's Ratio (ν)	0.3	0.3
Unit weight (γ)	16 kN/m³	
Reference Young's Modulus ($E_{50,\,ref}$)		40MPa
Unloading Modulus ($E_{ur,ref}$)		75MPa
Earth Pressure Coefficient (K_0)	0.47	0.47
Dilatancy Angle for non-associated flow (ψ)	5.0°	5.37°
Reference Stress (p_{ref})		100 kPa
Hardening Parameter (m)		0.5

4.4.2 Limit analysis

Limit analysis was performed using LimitState GEO to determine ultimate load-carrying capacity and failure mechanisms by identifying kinematically admissible collapse patterns without the need for iterative stress-strain analysis. In this study, LimitState GEO was applied to assess the bearing capacity and failure modes of three wall geometries to compare with both the experimental centrifuge test and the FEM simulations.

Model setup

Three wall models, straight-sided (S), and tapered walls (T1 and T2) were analyzed under plane strain conditions using a two-dimensional domain. The computational domain dimensions (800 mm wide and 450 mm high) and boundary conditions were identical to those used in the FEM simulations. Each wall was modeled as a rigid vertical body embedded to a depth of 224 mm. Wish-in-place model installation was used. The setup with model geometry and boundary layout are similar to that used in FEM using OPTUM G2 (Figure 4.9).

Sand and interface properties

The soil (Fontainebleau NE34 sand) was modeled using the Mohr-Coulomb failure criterion with an associated flow rule. The same basic parameter values (see Table 4.5) were used from the FEM analysis to ensure consistency. Wall–soil interaction was represented using a reduced interface friction angle of 16°.

Analysis procedure

Static vertical loading was applied at the top of each wall to simulate the loading conditions during centrifuge testing. The analysis provided upper-bound collapse loads and visual representations of the corresponding failure mechanisms. These results were then compared with those obtained from FEM simulations and centrifuge experiments to assess the influence of taper angle.

Mesh sensitivity study

To ensure the robustness of the limit analysis results, a mesh sensitivity study was performed. This involved varying the number and density of potential discontinuities by testing four mesh configurations: coarse, medium, fine, and very fine. These variations helped ensure that the numerical setup did not affect the analysis outcome.

CHAPTER FIVE

5. Stress distributions and pile load-settlement behavior

5.1 Introduction

The axial response of the three model walls, straight (S), and tapered (T1 and T2), is based on data obtained from the head load cell during both the installation and static loading phases. The results are discussed in terms of axial force during penetration, followed by static loading. Moreover, stress measurement in the soil mass and on the wall-soil interface was presented and analyzed in the following sections. The interpretation of the result, with comparison with previous works, is also presented.

5.2 Load-settlement behavior of walls

Three monotonic pushed-in tests with walls of different shapes were performed. In each test, the wall was pushed into the subsoil at 0.1mm/s rate to a depth of 224mm. Once the final depth was reached, slow unloading of the model head was performed, and then the static compression loading up to the displacement corresponding to the mean wall breadth B=16mm was applied followed by unloading head wall to zero and final pull-out test (see Figure 5.1).

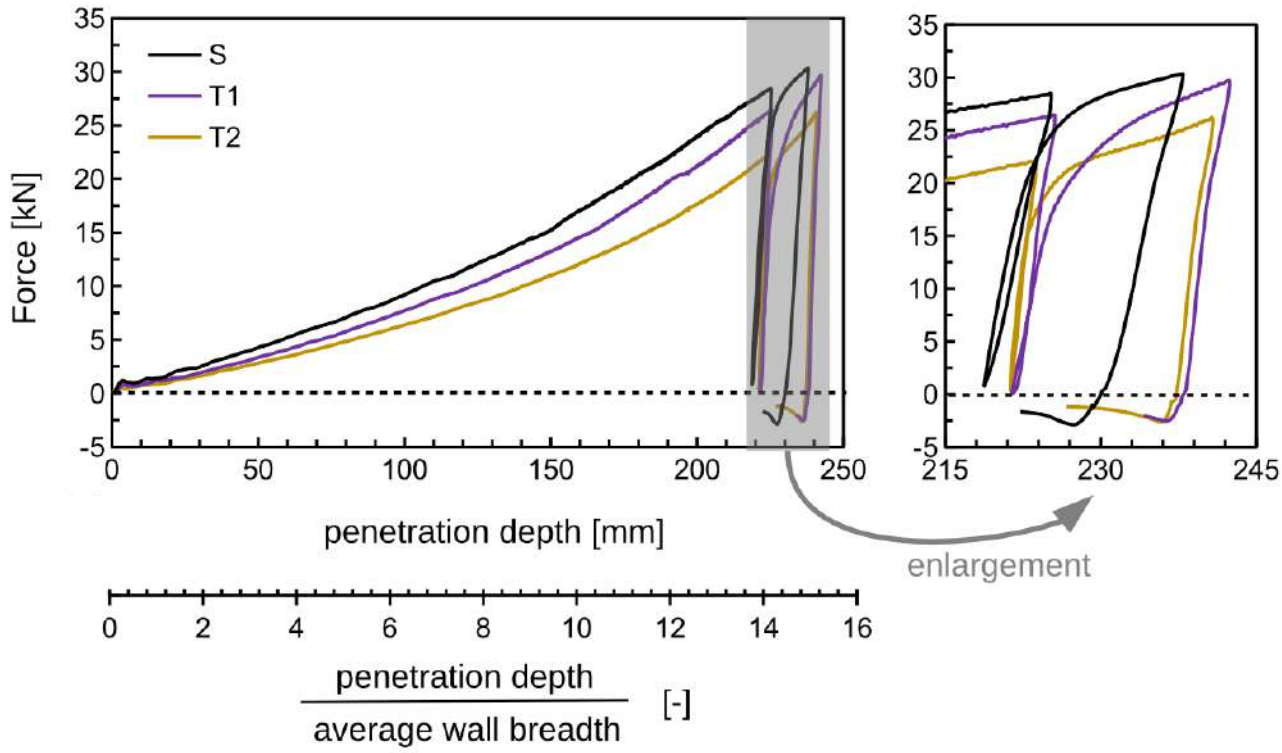

Figure 5.1: Load-settlement curves of walls for the entire test execution

The CPT test was performed at a distance of 12B from the side wall of the container to minimize boundary effects and ensure representative soil conditions. Figure 5.2a shows the mini-CPT performed in dense Fontainebleau sand during centrifuge testing, and Figure 5.2b shows the normalized cone resistance, $q_c/(\sigma'_{vo}/p_a)^{0.5}$ (Lunne et al., 1997). These curves indicate a uniform and homogeneous soil mass throughout the test.

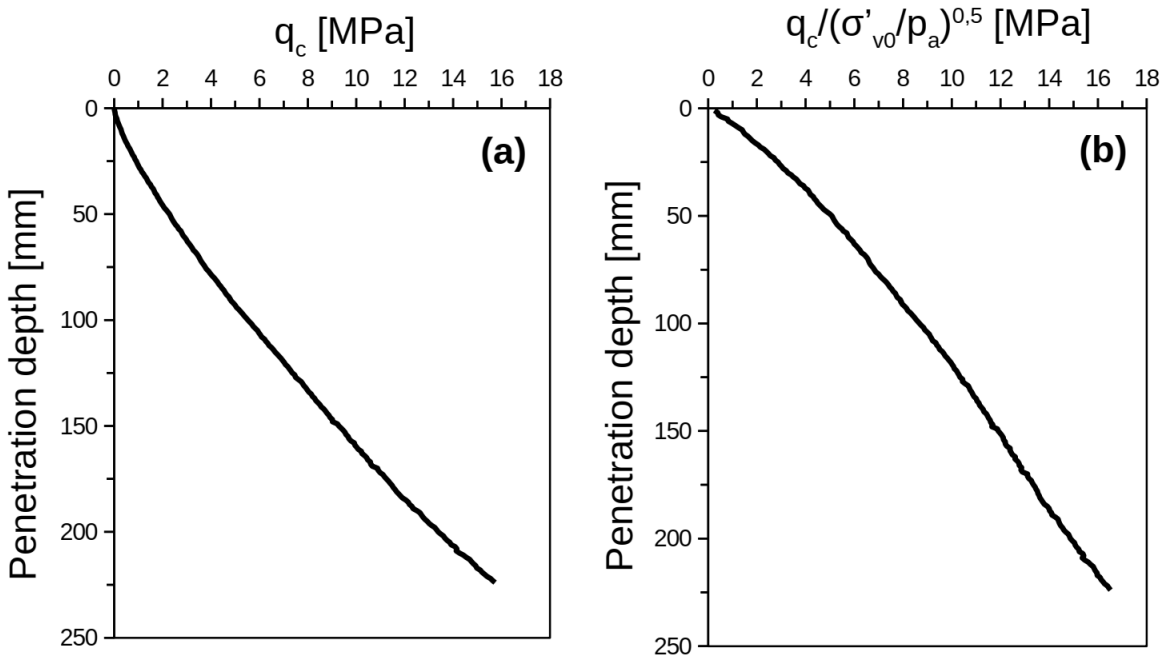

Figure 5.2: a) Cone resistance in dense Fontainebleau sand and b) normalized cone resistance

5.2.1 Installation phase

Figure 5.3 shows the mobilization of axial force for each wall type. It can be observed that the total force required for the wall insertion was slightly lower for the models with higher taper angles compared to the straight profile. At small depths, the penetration force for T2 and T1 constitutes only about 0.5 and 0.6 of the corresponding axial force for the straight wall, respectively. These ratios are getting higher with progressing penetration and approach 0.75÷0.9 at final embedment, which suggests easier and more efficient installation of tapered walls.

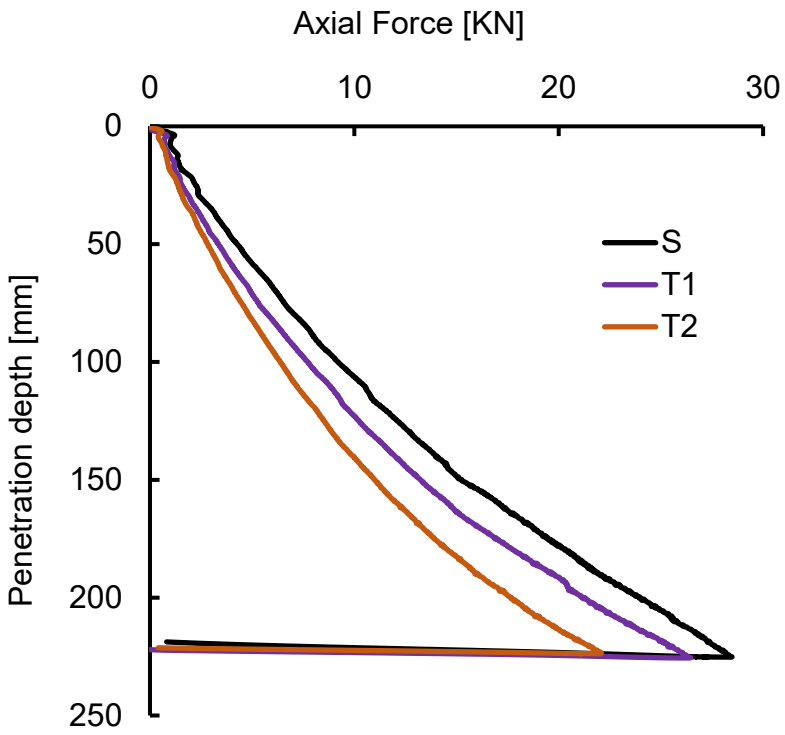

Figure 5.3: Axial force-penetration depth curves during installation of walls

One should notice that the tapered walls having the same volume and the same length were considered in the analysis. As the end-bearing mechanism dominates, the lower base area of tapered walls does not compensate for the increased lateral friction mobilized on the wall. As a result, the overall bearing capacity of tapered walls was lower than of the standard straight one. This observation is opposite to the centrifuge test results on tapered piles, which were however installed at 1g (Wei & El Naggar, 1998; M. H. E. Naggar & Sakr, 2000; M. H. Naggar & Sakr, 2002; Shabanpour & Ghazavi, 2022). Such installation mode does not permit to reproduce correctly the stress field in the pile vicinity and to model properly the installation process (Craig, 1985; Fan et al., 2021; Schlager & Moormann, 2022). At the end of installation at 1g the shaft friction is overestimated due to high dilatancy at small stress level, while the base resistance is hardly mobilized. The contribution of shaft friction to overall pile bearing capacity is thus higher than for the prototype.

To enable better comparison across wall types with varying base breadths, the head force is normalized by the wall base breadth (F/B). Figure 5.4 presents the results of normalized head force versus penetration depth. The head force normalized to a given wall base breadth is almost the same till the penetration of about 50 mm, and practically a very low shaft friction can be expected to develop (Klinkvort et al., 2013). Afterwards, due to higher friction mobilized on tapered walls, the curves start to diverge. One should notice that all wall models have the same lateral area.

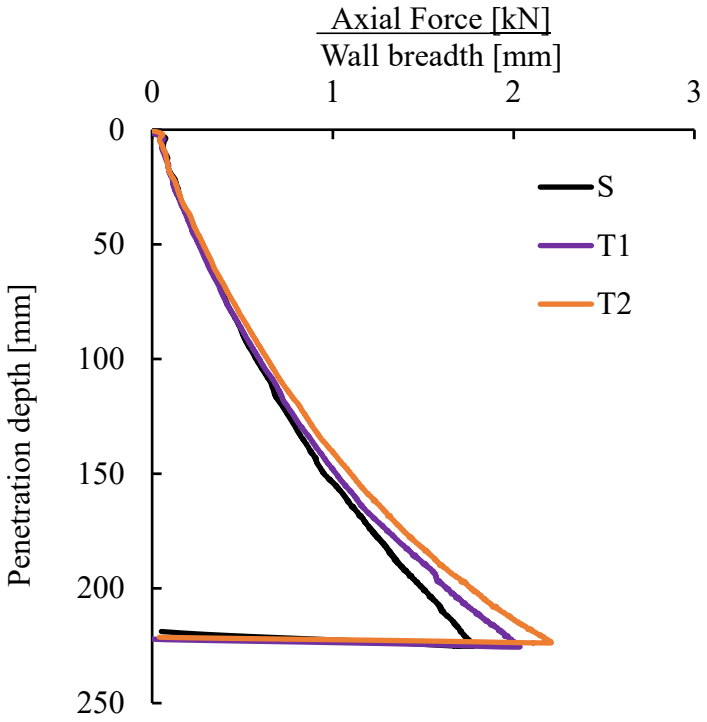

Figure 5.4: Normalized installation force-penetration depth curves of all walls.

5.2.2 Static loading phase

After installation, each wall was subjected to monotonic axial loading to evaluate its load-settlement behavior. The resulting load-displacement curves from the static loading tests are presented in Figure 5.5. The S wall exhibited a relatively stiff response, with a clear transition from the initial linear phase to a more gradual increase toward the ultimate load.

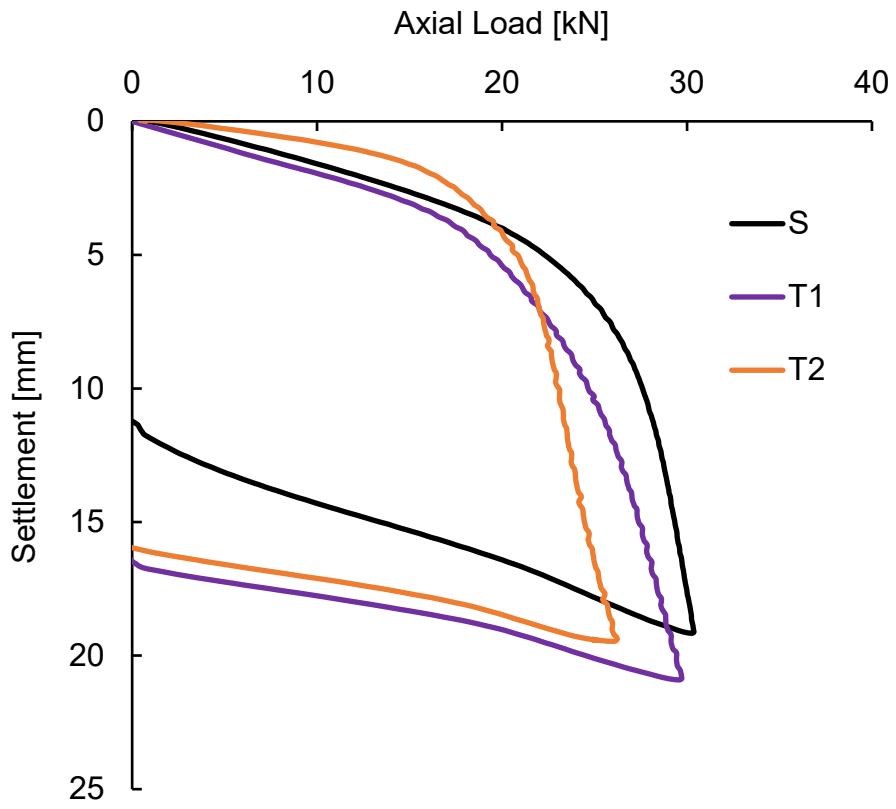

Figure 5.5: Load-displacement curves during static loading of S wall, T1 wall, and T2 wall

5.3 Stress on the wall surface

To measure the evolution of normal stress acting on the wall surface during monotonic installation, three sensors have been installed on each wall, see Figure 5.6d. The normal stress mobilized during continuous penetration of the wall is given in Figure 5.6 as a function of sensor embedment. For a given wall shape and the sensor depth, the largest values of moving normal stress are recorded at mid-depth of the model (B level), and they increase with taper angle. At the final stage of penetration, a considerable increase of normal stress is observed near the tip due to mobilization of base resistance. One should, however, note that the normal stress sensor on the tapered wall captures not only the horizontal stress component but the vertical one as well. The latter can considerably influence the measured values, especially in case of the stress cell located near the wall base.

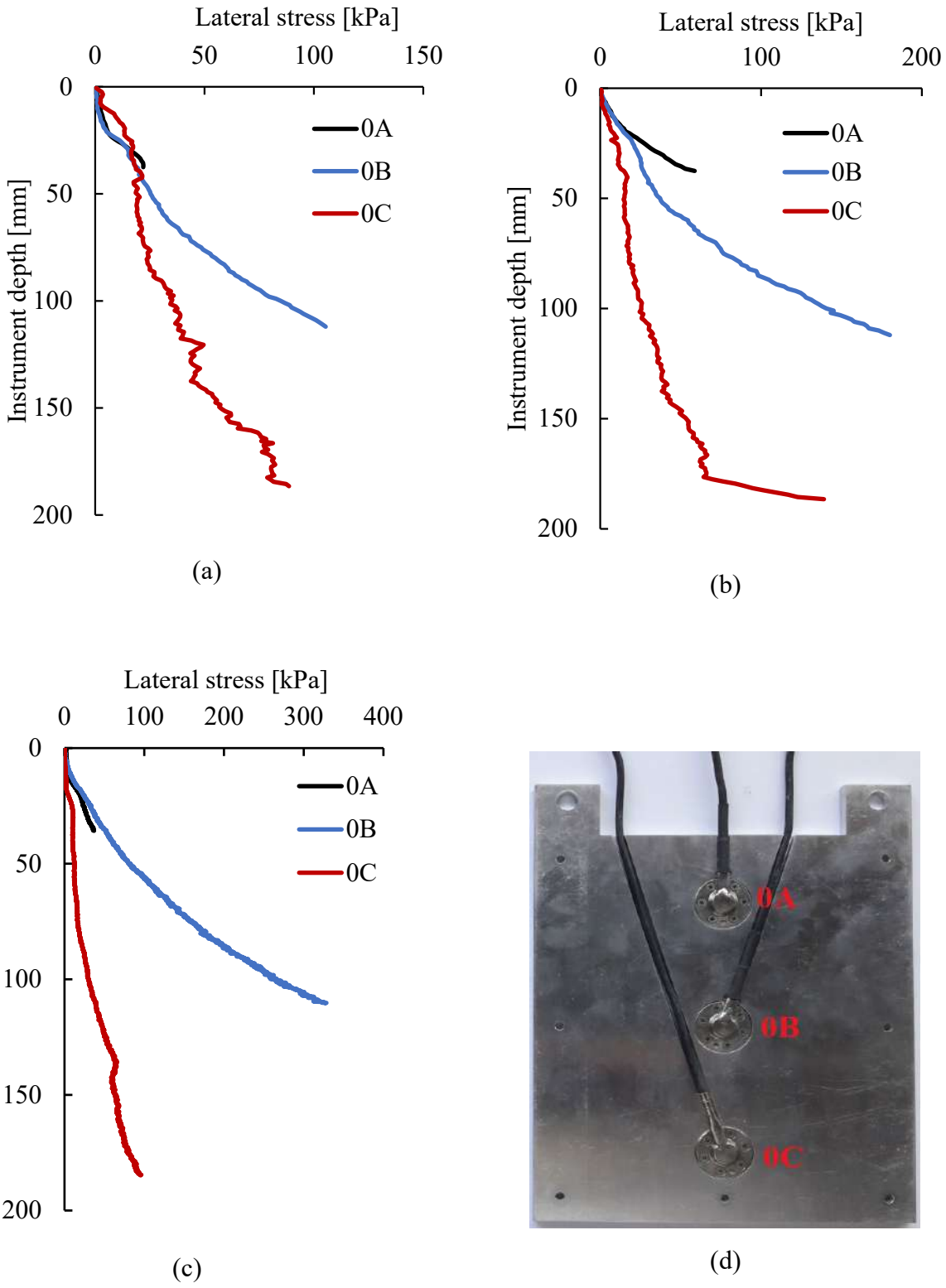

Figure 5.6: Normal stress evolution at the wall surface during installation of (a) S wall, (b) T1 wall, and (c) T2 wall d) sensor layout on the wall

To better interpret the wall–soil interaction for different wall geometries and depths, the measured lateral stress values were normalized by the cone resistance (q_c) obtained from adjacent CPT tests. The q_c values used for normalization correspond to the respective depths at which the stresses were mobilized. The normalization of lateral stress with q_c also allows for direct estimation of mobilized horizontal stress and has practical implications for predicting shaft capacity in design. At the end of wall penetration, the ratio of normal stress mobilized on the S wall to cone resistance is about 1.68% for B level and 0.7% for the sensor at C level (Figure 5.7). These ratios are comparable to the 1.6% value reported for monotonically installed pile models in centrifuge tests (White & Lehane, 2004).

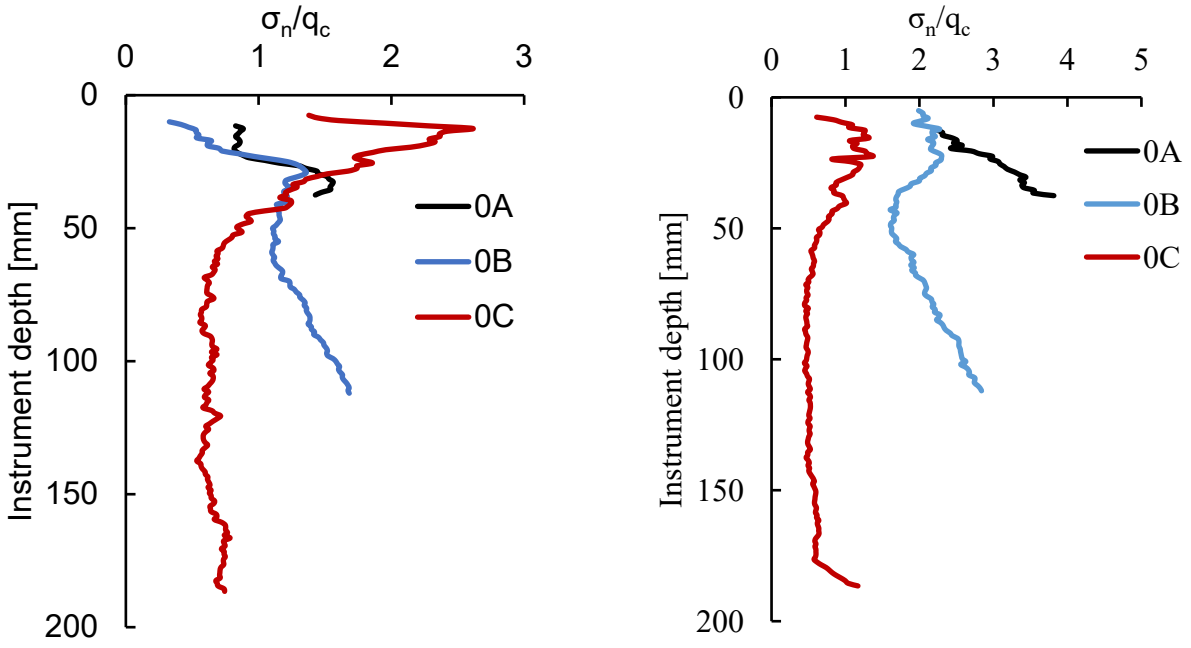

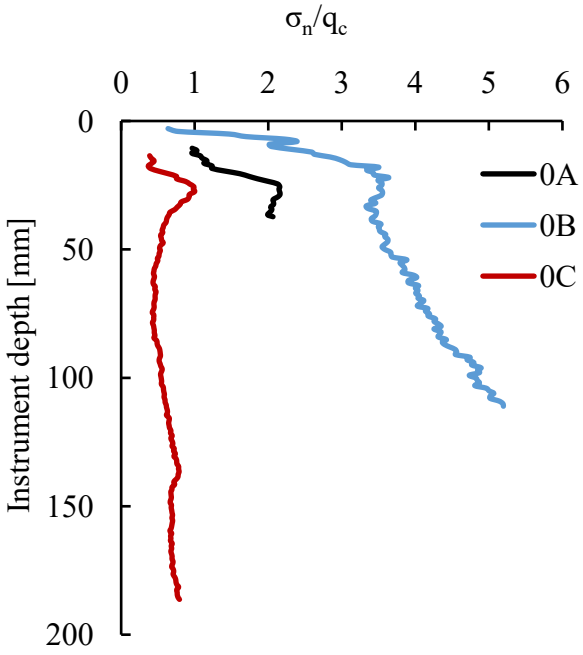

(c)

Figure 5.7: Stress on the wall normalized by cone resistance during installation of (a) S wall, (b) T1 wall, and (c) T2 wall

5.4 Stress mobilization in the soil mass

Measurements of lateral stress measured in the soil mass during both the installation and static loading were obtained from earth pressure cells positioned at two depths, Level B (112 mm) and Level C (186.5 mm), and at three horizontal distances (2B, 4B, and 6B) from the wall face.

5.4.1 Installation phase

All stresses measured during wall installation are referred to as moving stresses, as they were taken during the continuous pushing of the models. The stress distributions in the soil mass during wall installation have been recorded (Figures 5.8-5.10) from the sensors at two levels (B and C). The presented measurements start at earth pressure at rest registered after spin-up (soil conditioning). Notably, a distinct peak in stress was observed in the soil mass just before the wall base passed the level of the stress cell. This tendency can be noticed for the sensors in

both the upper and lower levels, indicating a maximum stress concentration at that specific location.

Once the wall base has moved below the position of the stress cells, a continuous decrease in stress was observed, reaching values close to or slightly above the initial ambient state. This trend was visible for the straight wall model (Figure 5.8) and aligns with the observations of Talesnick and Omer (2024) in calibration chamber tests.

In contrast, after the initial decrease for tapered walls, the stress cells at the upper level exhibit further slight re-mobilization of the horizontal stress (Figure 5.9a and 5.10a). This re-mobilization with further penetration is more noticeable for the wall with a higher taper angle. At a given sensor level, this re-mobilization is higher at stress cells closer to the wall.

The maximum value of horizontal stress gradually decreases with distance from the wall. For the stress sensors placed at a given distance from the wall, the highest maximum horizontal stress is observed for the S pile due to its largest base, which passes at the closest distance to the sensors. This maximum stress value decreases with the taper angle. At the end of the installation, the higher the taper angle of the wall, the larger the horizontal stress level is measured in the soil mass. While the continuous increase of soil stress at both sensor layers for T1 is still observed at the end of penetration, it is getting stabilized in the case of the T2 wall. One can thus expect that in the case of the T2 wall, the soil stress at the B-sensor level will reach a stable value after 7-8B penetration. This penetration length is necessary for the stabilization of the stress level within the soil mass and will probably be larger in the case of the wall with a lower taper angle.

A summary of stress evolution in the soil mass, along with the stress measured on the wall surface, is presented in Figure 5.11. The stress profiles in the soil mass and on the wall surface exhibit distinct behaviors. The mobilized stress on the wall increases monotonically with penetration depth. The mobilized contact stress at the end of penetration is considerably higher

than the horizontal stress in the soil mass. In contrast, the stress in the soil mass increases until the wall base reaches the sensor level, after which it decreases once the wall passes that level. One should notice a higher stress level mobilized at the end of penetration on the wall than in the soil mass in the case of B-level sensors. When comparing different wall shapes, the mobilized stress on the wall increases with the taper angle.

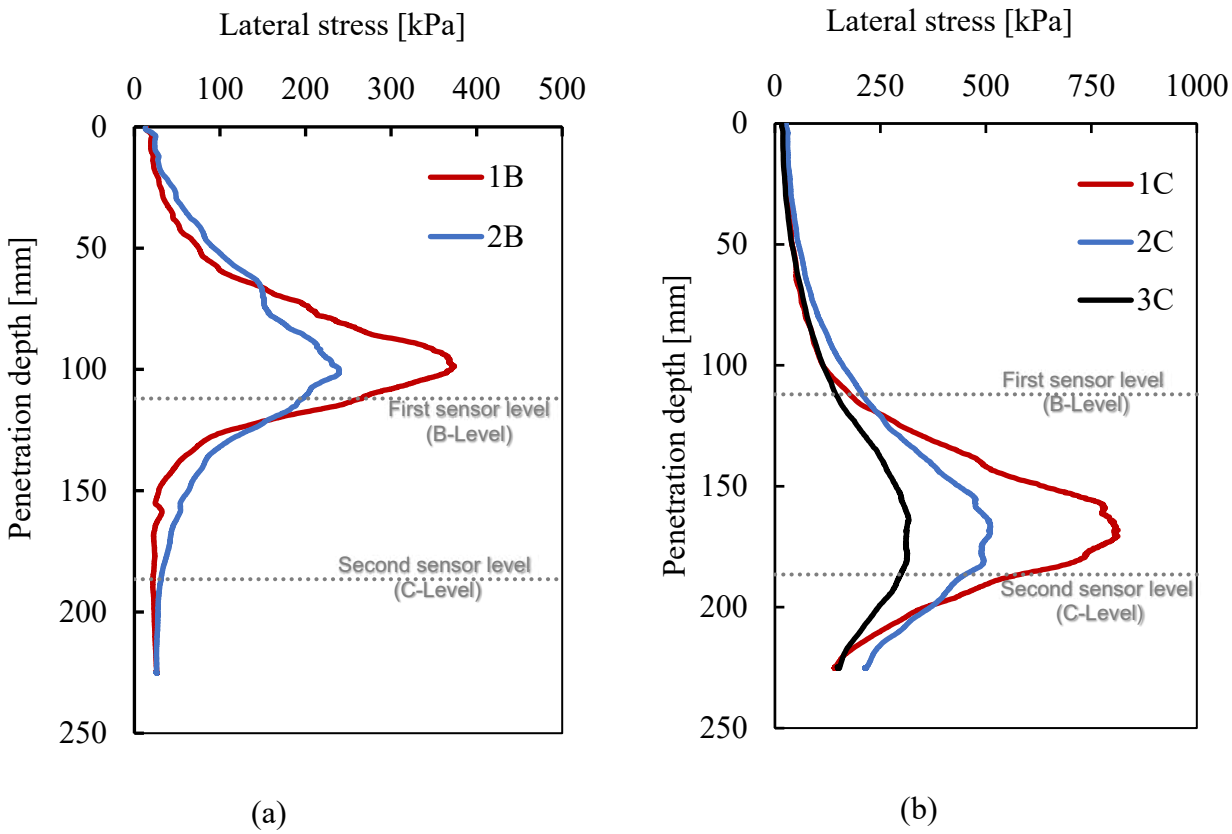

Figure 5.8: Stress mobilized in the soil during installation of S wall at a) B-level sensors, b) C-level sensors

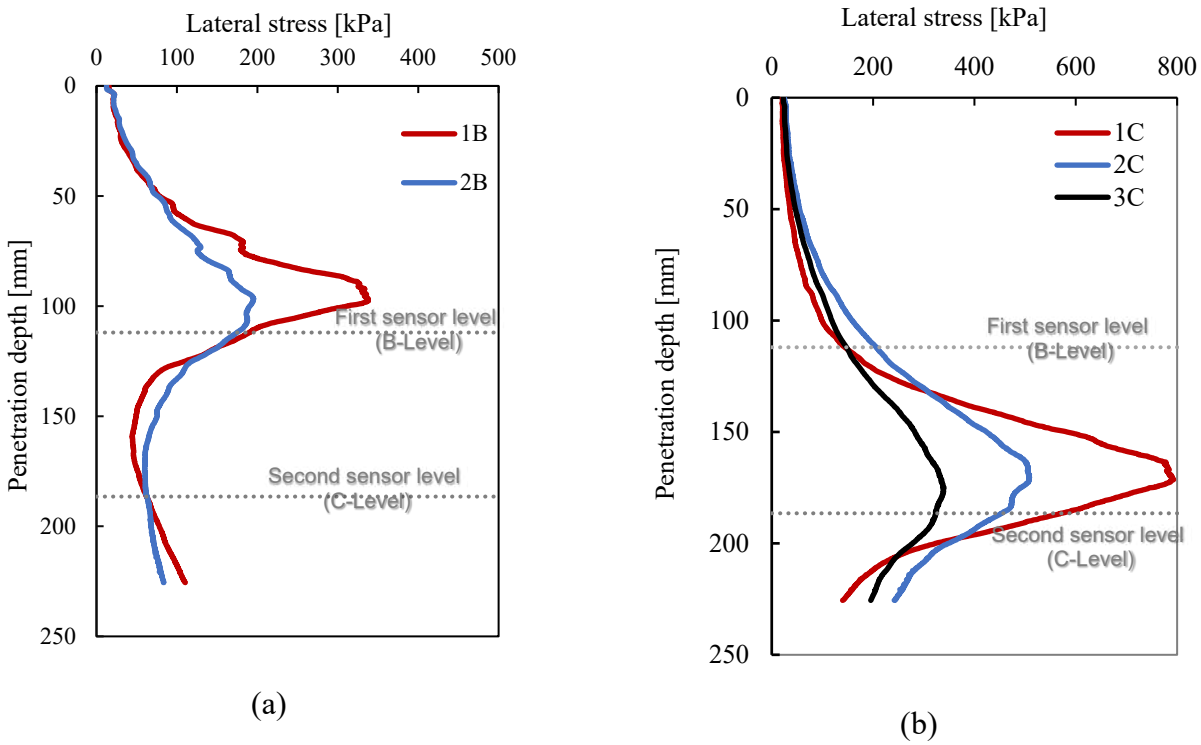

Figure 5.9: Stress mobilized in the soil during installation of T1 wall at a) B-level sensors, b) C-level sensors

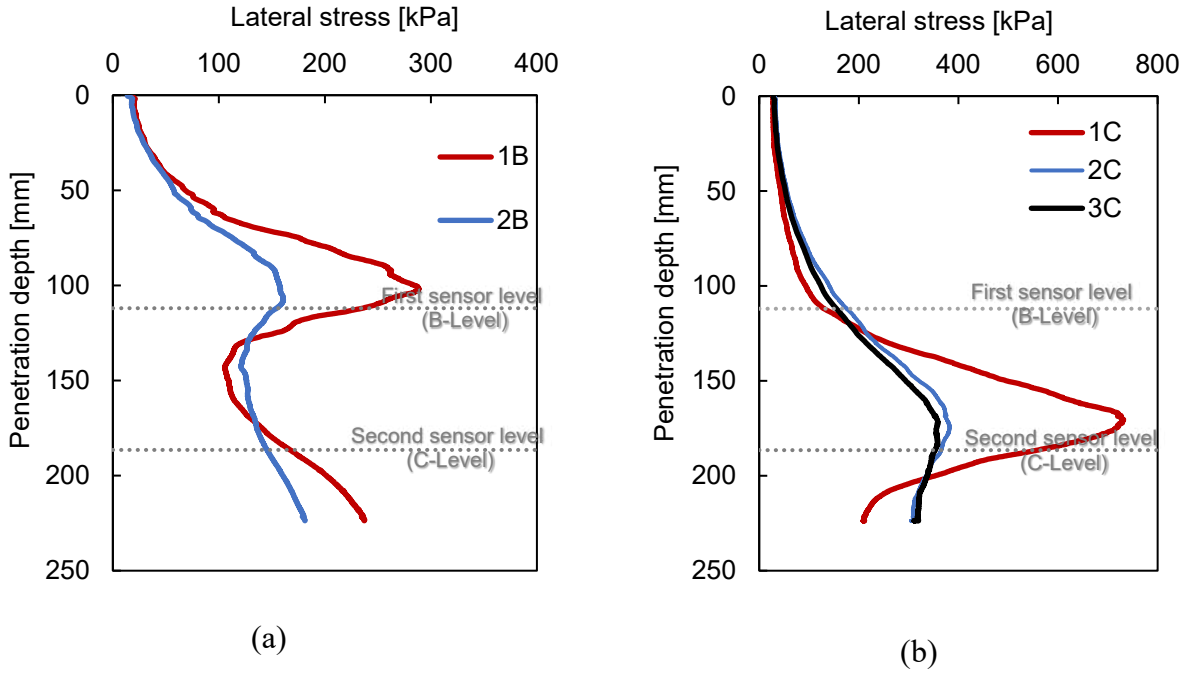

Figure 5.10: Stress mobilized in the soil during installation of T2 wall at a) B-level sensors, b) C-level sensors.

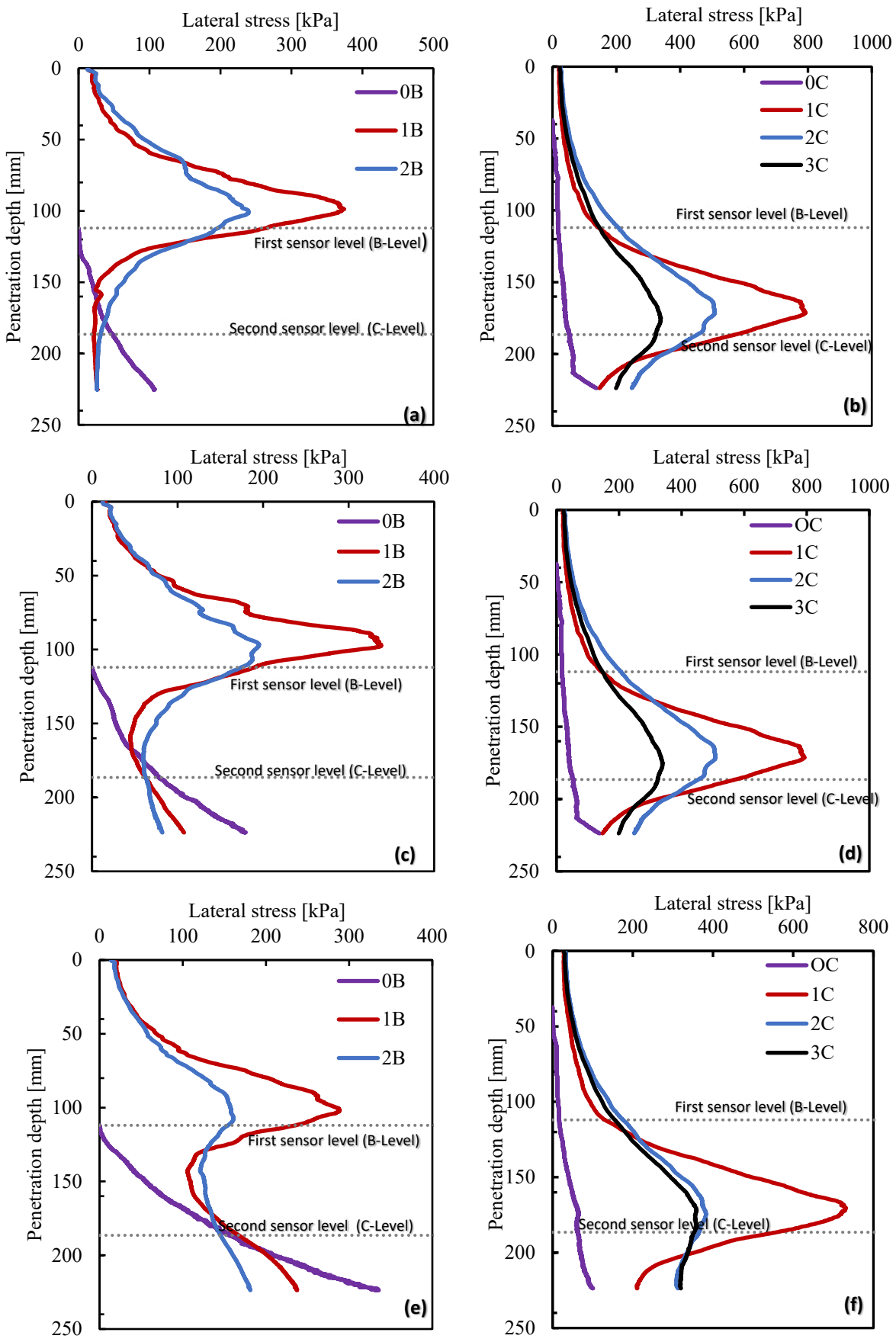

Figure 5.11: Stress distribution in the soil mass and on the wall during installation: (a)-(b) standard (S), (c)-(d) tapered (T1), and (e)-(f) tapered (T2)

Mobilized stress normalized by initial horizontal stress

The measured lateral stresses were normalized with the initial horizontal stress. The initial horizontal stress calculated at B-level is 21.59 kPa, and at the C-Level is 35.95 kPa. These mobilized stress distributions for all walls are shown in Figure 5.12. Higher stress ratio with a distinct peak is obtained for the nearest cell position. For a given wall shape, this ratio is larger for the stress sensors at a lower level, where it can exceed 20. A considerable drop in horizontal stress is observed after the wall base has passed the position of the sensors. In case of tapered models, this stress attenuation is less pronounced, and distinct re-mobilization of horizontal stress is even observed at the upper level of sensors during further wall penetration. In case of a tapered wall T2, one can expect the horizontal stress stabilization after the wall base has passed 7B below the sensing position. Further wall penetration would not substantially increase the value of horizontal stress at a given level. The mentioned distance will probably be larger for the walls with a smaller taper angle.

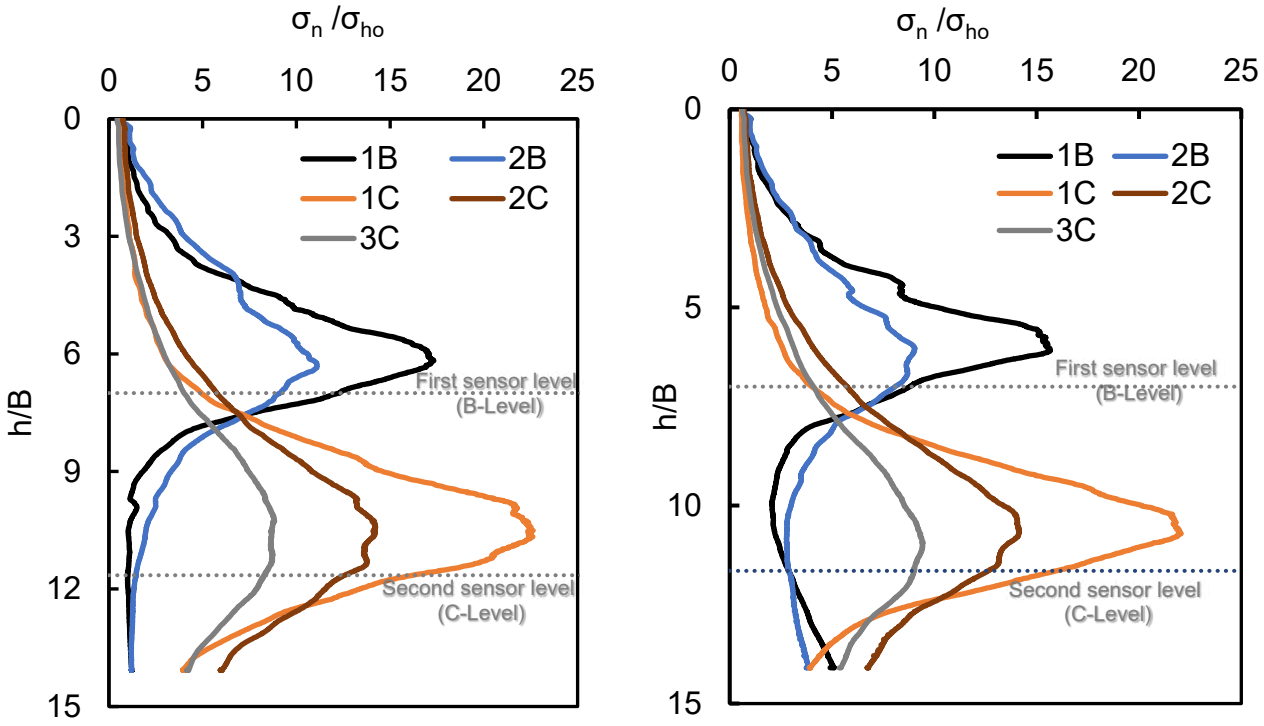

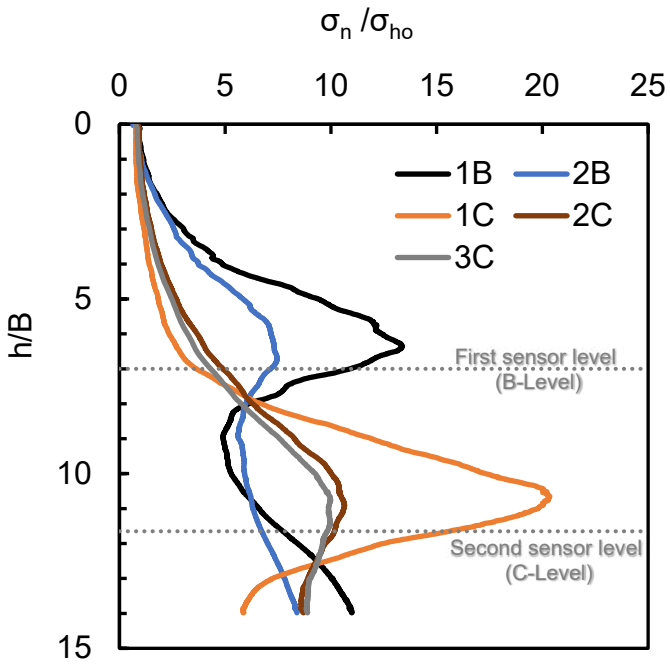

(c)

Figure 5.12: Mobilized lateral stress in the soil during wall installation normalized with initial stress (a) S wall, (b) T1 wall, and (c) T2 wall

Mobilized stress normalized by cone resistance

The measured stresses were further normalized using the cone resistance values obtained from the CPT test. The reference cone resistance (q_c) values used for normalization were taken from the CPT results shown in Figure 5.2a. A value of 6.4 MPa was used for sensors located at the first level (B-Level), while 12.19 MPa was used for sensors at the second level (C-Level). Higher stress ratios with distinct peaks are observed for the sensors located closest to the wall (1B and 1C), indicating larger stress mobilization during wall installation (Figure 5.13). Among these, the sensors placed at the C-level, located near the wall base, consistently recorded higher normalized stresses than the corresponding B-level sensors (1B and 2B), which are positioned closer to the mid-depth of the wall. For instance, in all three wall types, peak values at C-level sensors reached approximately 6–7σ_n/q_c, while B-level sensors generally ranged between 4 and 6 σ_n/q_c. This indicates that the stress concentration is more pronounced near the wall base,

suggesting a significant effect of depth and installation effects on lateral stress development in the surrounding soil. These observed values are consistent with previous findings in the literature. Jardine et al. (2013) reported normalized radial stresses (σ_n/q_c) reaching up to approximately 3% in calibration chamber tests around closed-ended displacement piles installed in dense Fontainebleau sand. heir results showed greater stress mobilization near the pile shaft (h/R = 6.7), which reduced with increasing distance (h/R = 21.7). While the values in this study are higher, the observed stress distribution patterns align closely with their finding, particularly the depth and location-dependent mobilization of horizontal stress during pile installation.

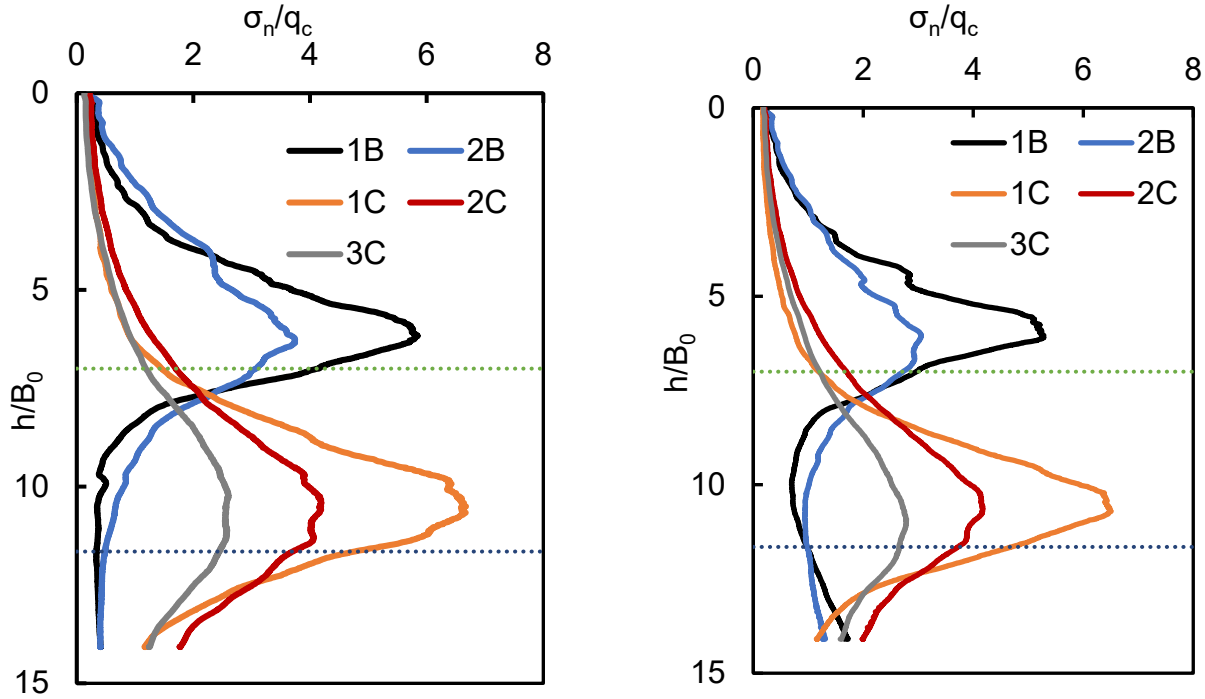

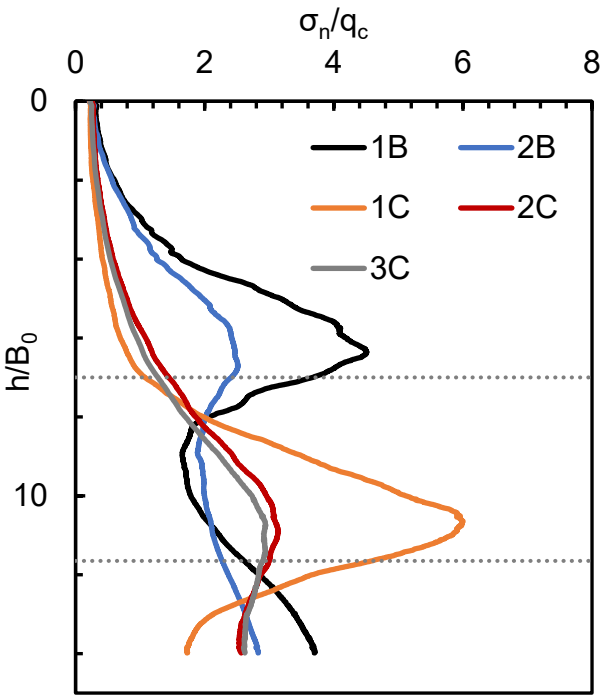

(c)

Figure 5.13: Mobilized lateral stress in the soil during wall installation normalized with cone resistance (a) S wall, (b) T1 wall, and (c) T2 wall. B_0 is the average wall breadth =16mm.

5.4.2 Post-installation state

The distribution of normal stress around the wall is presented (Figure 5.14) for moving and stationary stages (after unloading the model head to zero). At the end of installation, the highest normal stresses (both moving and stationary stresses) are measured for the T2 wall and the lowest for the S wall for both sensor layers. For the first sensor horizon (B-level, h/B=7), the contact stresses at the wall surface are generally higher than in the soil mass. One should notice even 15 times and nearly 6 times higher contact stress level than the soil horizontal stress prior to installation for T2 wall in case of moving and stationary conditions, respectively.The opposite tendency is observed in the second layer of sensors (C-level h/B=2.35), where the stress level still attenuates after the wall base has passed the sensing position. The moving stresses at the wall surface are considerably lower than the maxima in the soil mass. Such a tendency could be related to the soil contractancy in the zone of high stress level in the vicinity

of the wall base. When the soil flows upwards to the zone of lower stress level in the mid-height of the model, the dilative behavior of dense sand near the advancing model (White & Bolton, 2004) results in increased normal stress in the proximity of the wall.

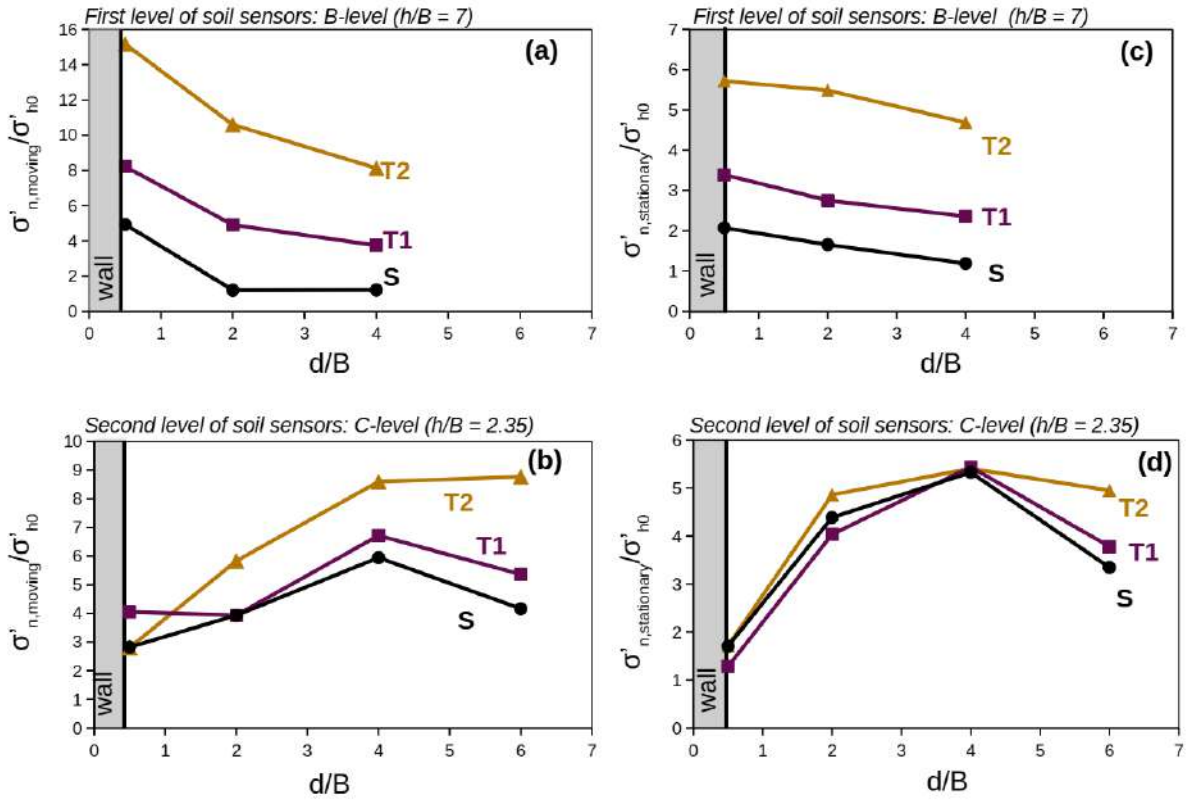

Figure 5.14: Distribution of normal stress (σ'_n) normalized with the initial horizontal stress (σ'_{h0}) (d = distance from the wall axis; B = average wall breadth, B = 16 mm) after monotonic installation (moving) (a-b), and after unloading (stationary) (c-d).

The stresses after installation have been normalized with the cone resistance (q_c) and are shown in Figure 5.15. The reference cone resistance (q_c) values used for normalization (previously mentioned as 6.4 MPa for B-Level and 12.19 MPa for C-Level) were selected based on the CPT profile shown in Figure 5.2a. It can be observed that similar trends to those normalized with the initial horizontal stress (σ'_{h0}) are maintained, with peak values occurring near the wall face and gradually decreasing with distance from the wall axis. The profile of stress normalized with cone resistance is similar to that of the stationary radial stress distribution presented by Jardine et al. (2013). Their result shows that the normalized stress with cone resistance peaks

near the pile shaft (r/R ≈ 2–3) and decreases with distance. Moreover, the variation in stress profiles with depth observed in the present study shows a strong similarity to their results at different h/R levels. For example, for h/B = 7, the lateral stress distribution is nearly similar to the flatter profile reported in their work for larger h/R values (e.g., h/R = 16-21 and 31.1). In contrast, the more curved profile observed at h/B = 2.35 resembles the steeper stress gradients reported in Jardine et al. (2013) for lower h/R = 5.6. These similarities further support the depth-dependent nature of lateral stress mobilization and the comparability between the wall and pile-induced stress fields.

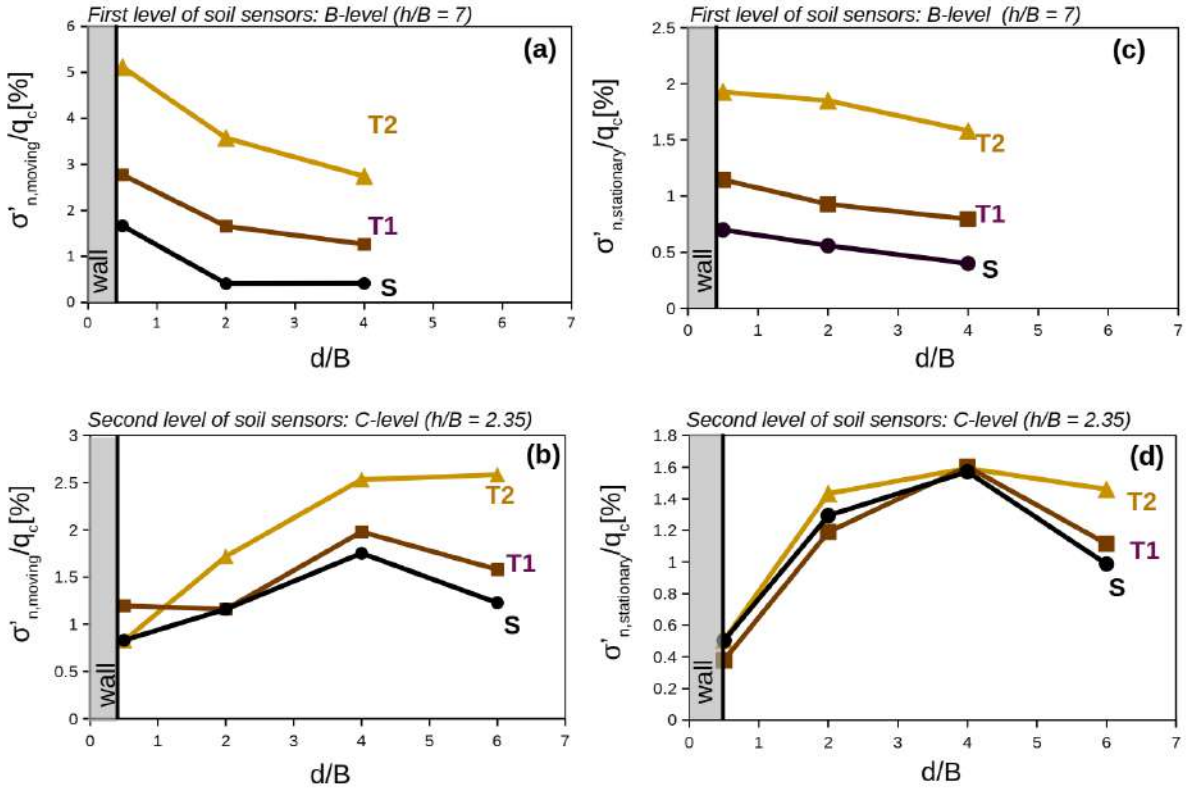

Figure 5.15: Distribution of lateral stress normalized with the initial horizontal stress (d = distance from the wall axis; B = average wall breadth, B = 16 mm) after monotonic installation (moving) (a-b), and after unloading (stationary) (c-d).

5.4.3 Loading phase

Figure 5.16 shows the horizontal stress mobilized in the soil during static loading of the S wall, measured at two sensor levels. At the shallower B-level (Figure 5.16a), the mobilized stresses are relatively low and uniform, showing only slight variation with increasing settlement. In contrast, the deeper C-level (Figure 5.16b) exhibits higher stress values, with noticeable differences among the sensors. A distinct reduction in horizontal stress is observed at the initial stage of loading at the C-level, which may be attributed to local stress redistribution or reversal.

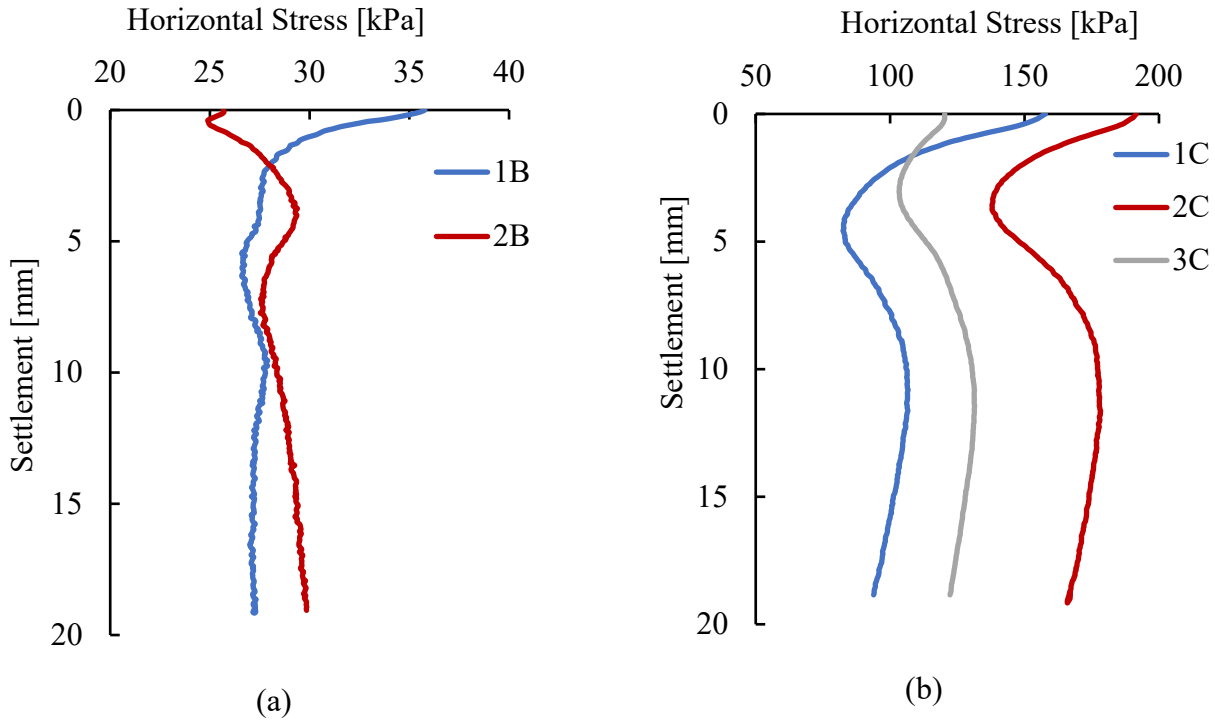

Figure 5.16: Stress mobilized in the soil during static loading of S wall at a) B-level b) C-level

Figure 5.17 presents the horizontal stress response in the soil during static loading of the T1 wall. At the B-level (Figure 4.17a), horizontal stresses increase progressively with settlement, with the sensor closest to the wall recording slightly higher values than the other. At the deeper C-level (Figure 5.17b), a significant drop of horizontal stress is observed in the vicinity of the wall base due to soil compressibility.

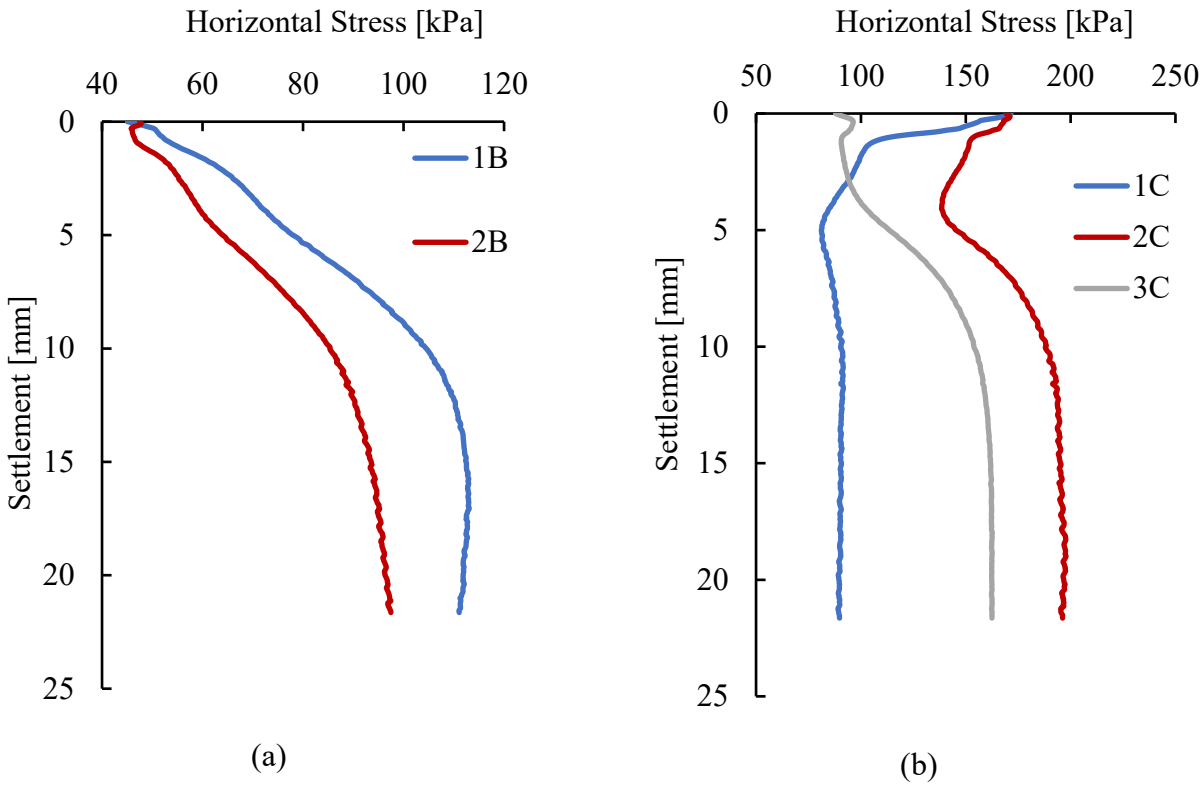

Figure 5.17: Stress mobilized in the soil during static loading of T1 wall at a) B-level, b) C-level

Figure 5.18 shows the horizontal stress mobilized in the soil during static loading of the T2 wall. At B-level (Figure 5.18a), sensors 1B and 2B show a steady increase in horizontal stress with settlement. Higher stress values are observed than those observed for the S and T1 walls. At C-level (Figure 5.18b), the higher stress are mobilized, with sensors 2C and 3C mobilizing the highest values, followed by 1C. Similarly to S and T1 wall, a decrease of horizontal stress is observed in the vicinity of the wall base.

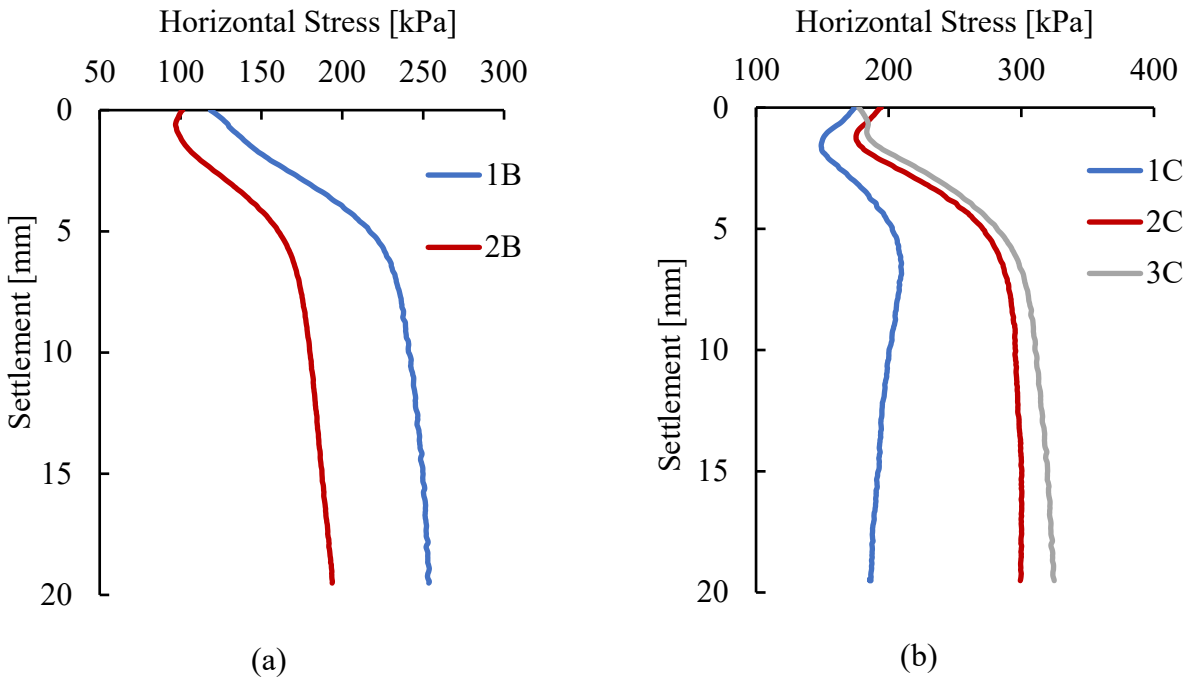

Figure 5.18: Stress mobilized in the soil during static loading of T2 wall at a) B-level, b) C-level.

5.5 Comparative analysis of wall types

5.5.1 Contact stress on the wall

Figure 5.19 compares the lateral stress measured at sensor 0A for all wall types during the installation (Figure 5.19a) and static loading phases (Figure 5.19b). During installation, the tapered walls (T1 and T2) mobilized higher lateral stresses compared to the straight wall (S), with T1 exhibiting the greatest stress levels. A similar trend was observed during the loading phase, where the tapered wall again showed the highest lateral stress response, while the S wall recorded the lowest values. These observations suggest that wall geometry has a significant impact on stress mobilization, with tapered shape more mobilizing lateral contact stresses throughout both phases. One should also notice that these observations are taken at small depths, where the complex failure mechanism is influenced by the proximity of the soil surface.

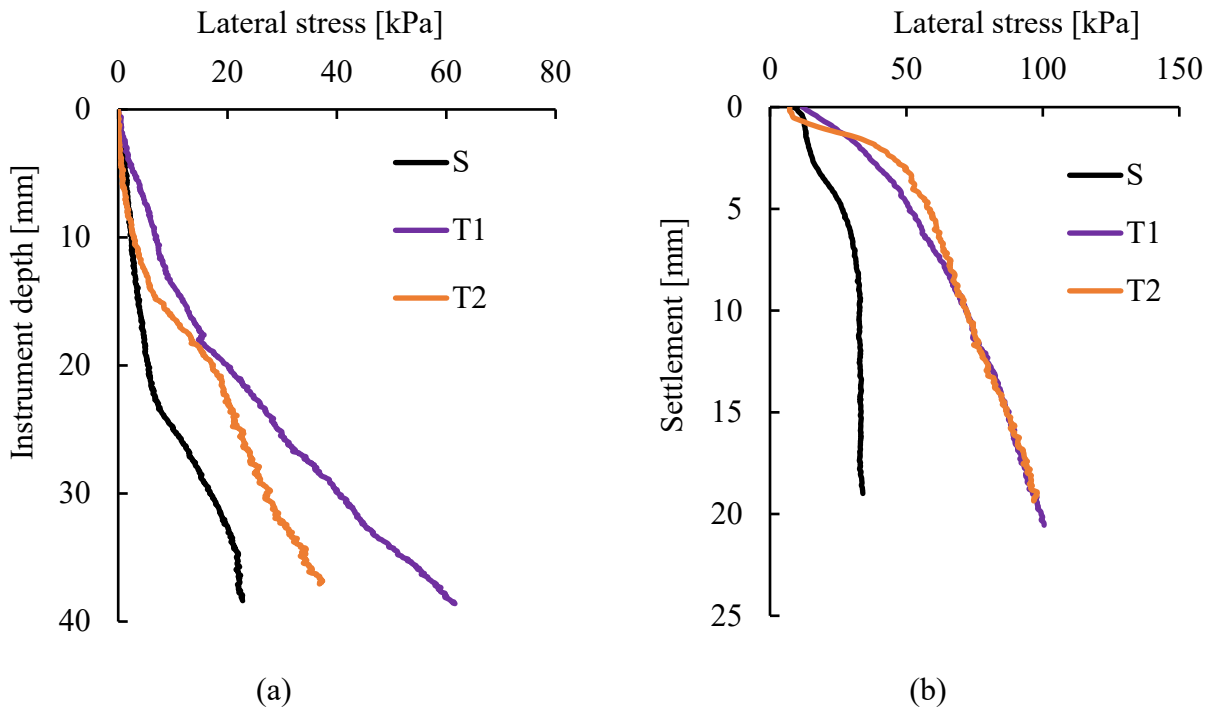

Figure 5.19: Comparison of stress measured from sensor 0A during a) installation, b) loading

At the mid-depth of the walls (sensor 0B), Figure 5.20 indicates that both tapered walls (T1 and T2) mobilized higher lateral stresses during installation compared to the straight wall (S), with similar values observed for T1 and T2. The effect of tapering appears to be more pronounced at this depth. Under static loading (Figure 5.20b), the differences in lateral stress became even more evident. Both tapered walls exhibited higher stress responses than the straight wall, with T2 exceeding T1.

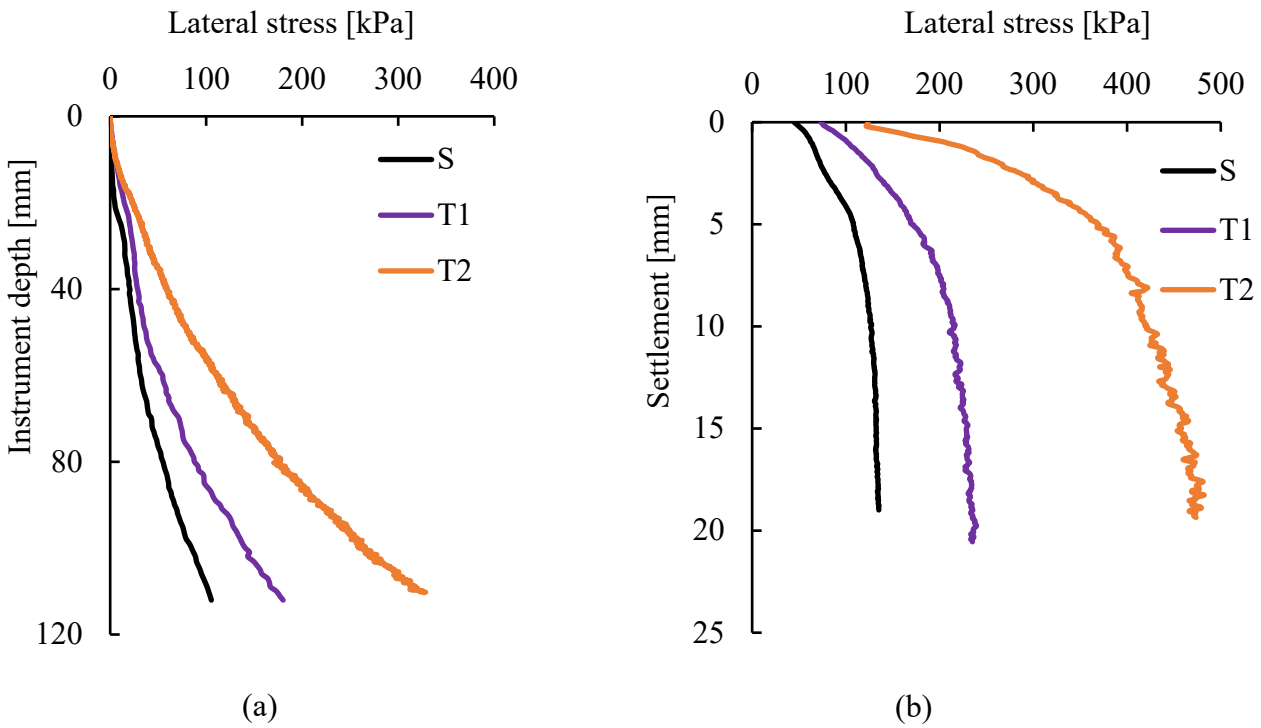

Figure 5.20: Comparison of stress measured from sensor 0B during a) installation b) loading

Figure 5.21 compares the lateral stress response nearly at the base level of the walls (sensor 0C). During installation (Figure 5.21a), the T2 wall mobilized higher stresses compared to the straight wall which indicates a strong influence of the wall geometry near the base. Under static loading (Figure 5.21b), both tapered walls again exhibited greater stress development than the straight wall, with the T1 wall showing the largest horizontal stress.

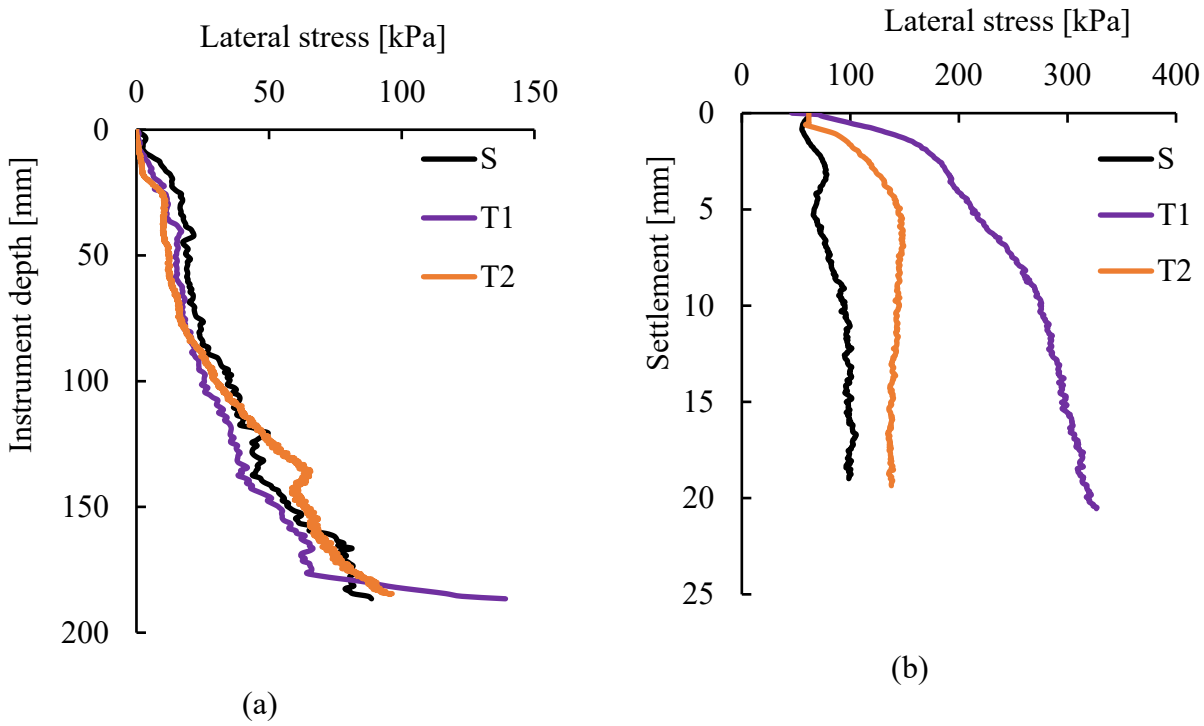

Figure 5.21: Comparison of stress measured from sensor 0C during a) installation b) loading

5.5.2 Stress in the soil mass

Stress at 2D distance

Figures 5.22 and 5.23 show the lateral stress distribution in the soil mass at a 2D distance from the wall, based on measurements from sensors 1B and 1C, respectively. During installation (Figures 5.22a and 5.23a), slightly similar stress levels were observed across all wall types at the deeper sensor (1C), particularly before the wall base passes stress level. However, at the shallower sensor (1B), both tapered walls exhibited slightly higher lateral stresses beyond a certain depth, with the T2 wall mobilizing the highest stress near the base. Notably, a localized peak in stress was recorded just before the walls reached the sensor level, with the T1 wall showing the largest stress at that point.

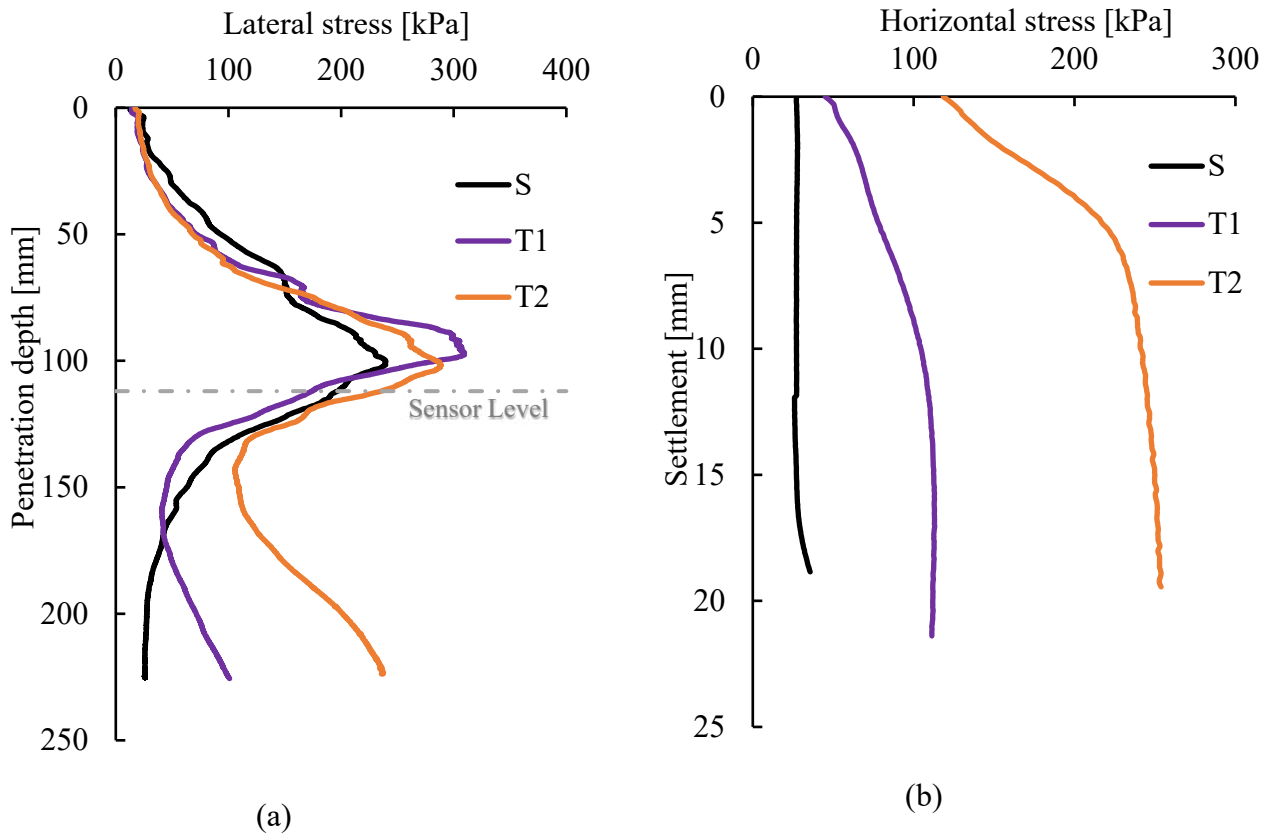

Figure 5.22: Comparison of stress measured from sensor 1B during a) installation, b) loading

The tapered walls induced the highest lateral stresses during static loading (Figures 5.22b and 5.23b). At sensor 1B, the S wall mobilized a relatively constant and low stress level throughout the loading phase, while the stresses with the tapered walls increased progressively with the settlement. A similar trend was observed at sensor 1C, where T2 wall mobilized higher stresses than the S and T1 walls. These results confirm that while installation-induced stress was relatively similar across all wall types, the influence of wall taper became more pronounced under loading, with the T2 wall consistently mobilizing the highest stress in the surrounding soil mass. This can be attributed to the higher taper angle of the T2 wall, which likely generated greater soil displacement and interaction during settlement, thereby mobilizing increased lateral stress.

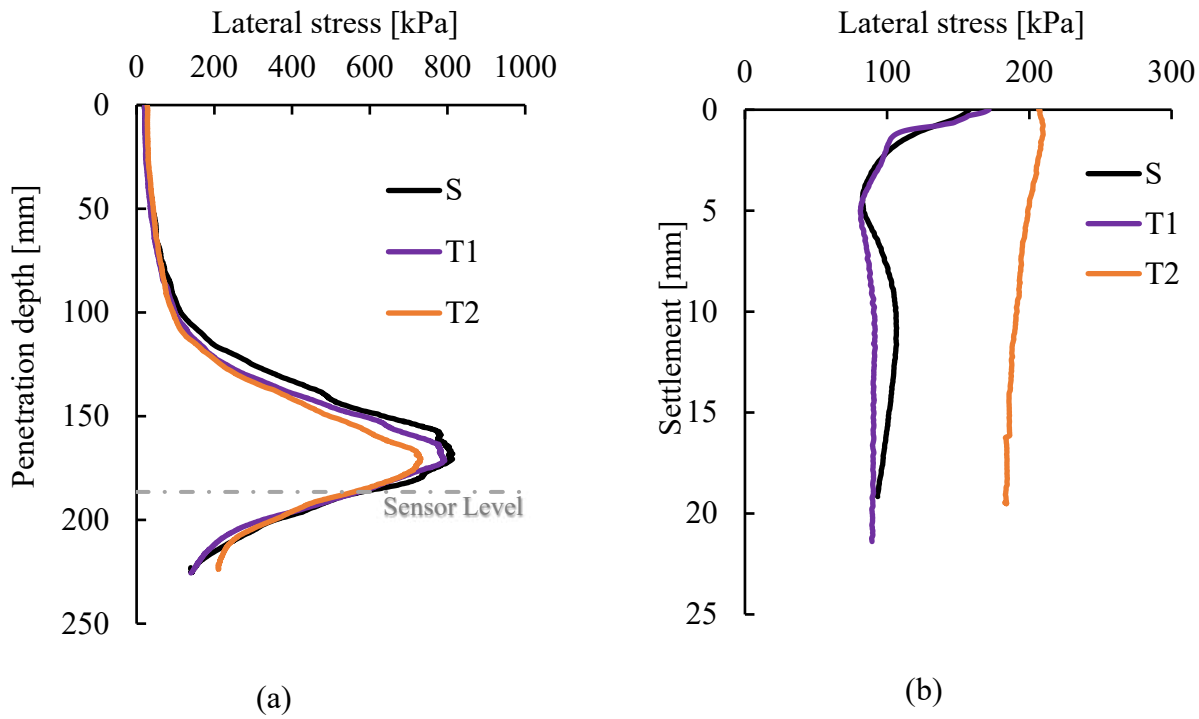

Figure 5.23: Comparison of stress measured from sensor 1C during a) installation b) loading

Stress at 4D distance

Figure 5.24 shows the lateral stress development at a distance of 4D from the wall face, based on measurements from sensor 2B during both installation and static loading. During installation (Figure 5.24a), the S wall initially mobilized the highest stress before reaching the sensor level, showing a distinct peak at shallow depth. However, once the wall tip passed the sensor, the trend shifted, with the tapered walls, particularly T2, mobilizing greater stresses toward the end of the installation. This pattern continued during static loading (Figure 5.24b), where the tapered walls continued to induce substantially higher lateral stresses than the straight wall, which remained relatively unchanged.

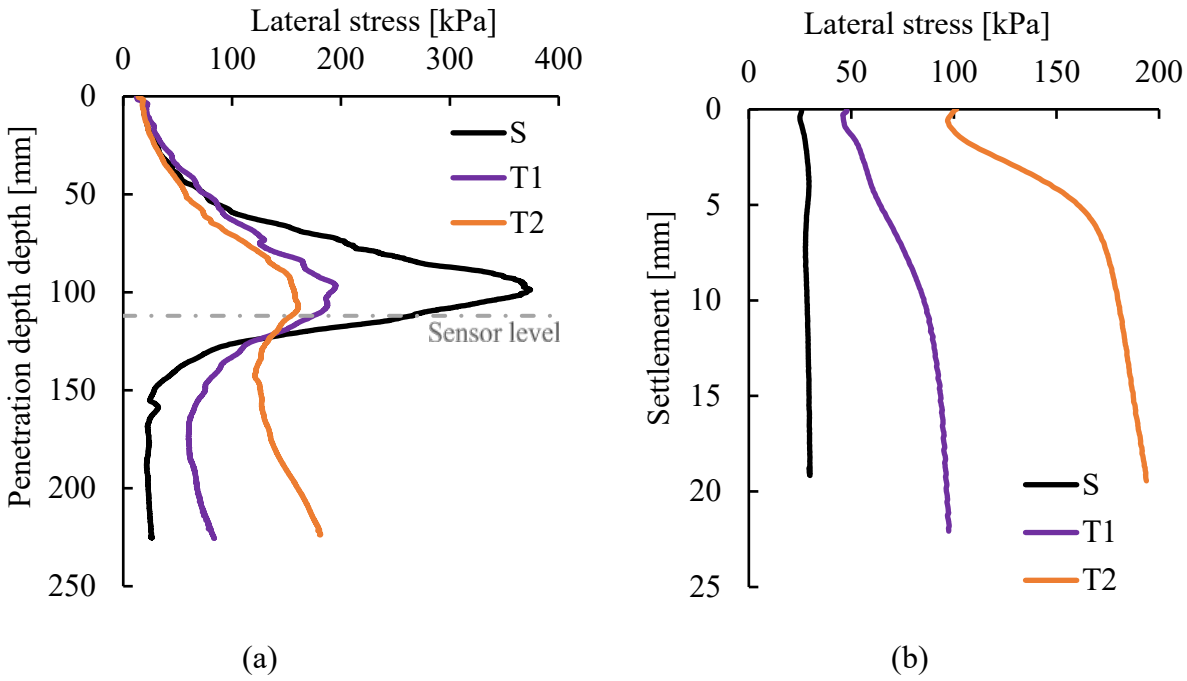

Figure 5.24: Comparison of stress measured from sensor 2B during a) installation b) loading

Figure 5.25 shows the lateral stress distribution measured at a distance of 4D from the wall face using sensor 2C. During installation (Figure 5.25a), the S and T1 wall initially mobilized nearly similar higher stress than T2 wall. However, as the walls approached the penetration end, the tapered walls, particularly T2, began registering slightly higher stresses.

Under static loading (Figure 5.25b), the differences became more pronounced, with the T2 wall mobilizing the highest lateral stress, followed by T1, while the S wall developed comparatively lower stress levels. These results suggest that while the straight (S) wall tends to generate higher lateral stresses during the initial installation phase, the tapered walls become more effective in developing lateral resistance under static loading conditions, leading to higher stress levels in the surrounding soil.

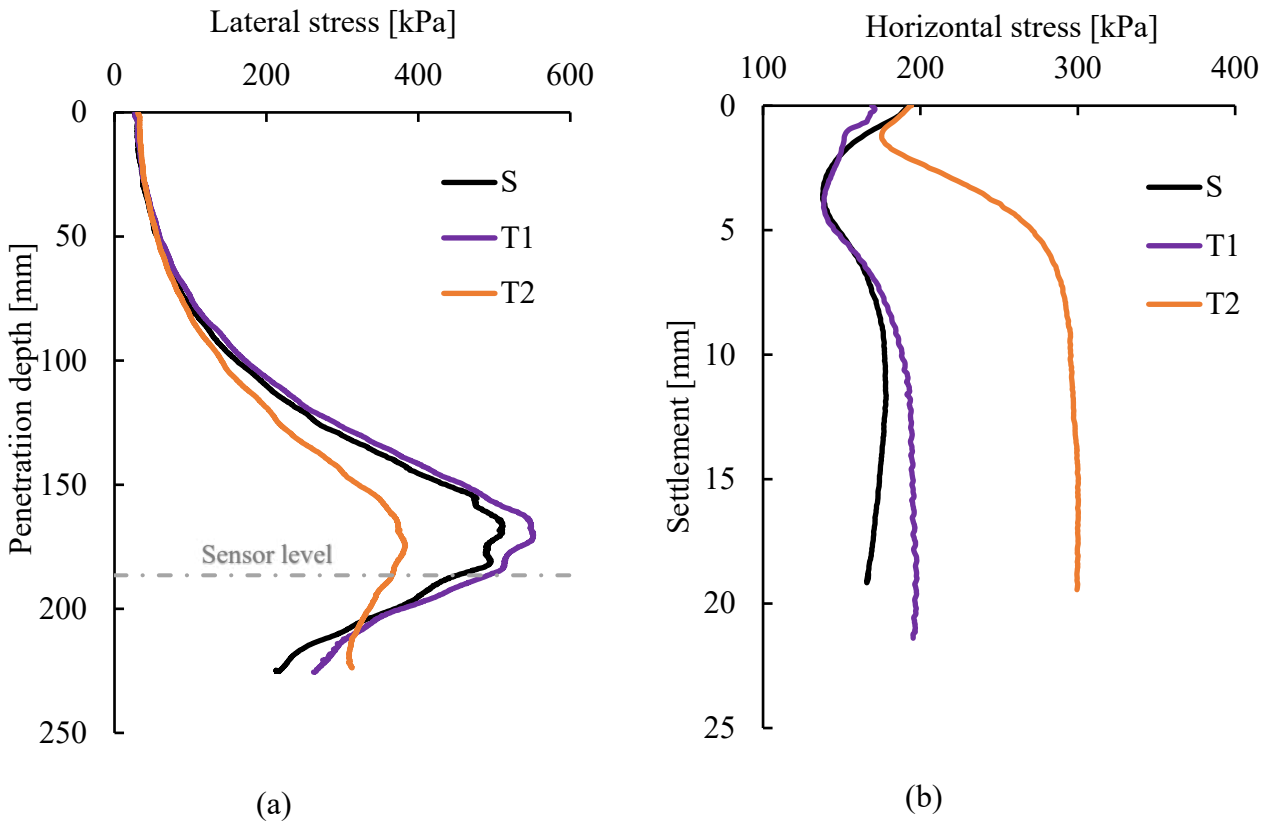

Figure 5.25: Comparison of stress measured from sensor 2C during a) installation b) loading

Stress at 6D distance

Figure 5.26 shows the lateral stress distribution measured at a distance of 6D from the wall face registered using sensor 3C. The overall trends are similar to those observed at 4D (Figure 5.25), but the stress magnitudes are generally lower due to the increased distance from the wall. During installation (Figure 5.26a), all wall types exhibited comparable stress levels in the upper depth. However, the T2 wall began to mobilize significantly higher stresses beyond a certain depth than the others. Under static loading (Figure 5.26b), this pattern continued, with T2 again generating the highest lateral stress, followed by T1 and then the S wall. These findings further highlight that the influence of wall tapering extends over a considerable distance into the soil mass, with the T2 wall representing the most substantial stress mobilization even at greater distances.

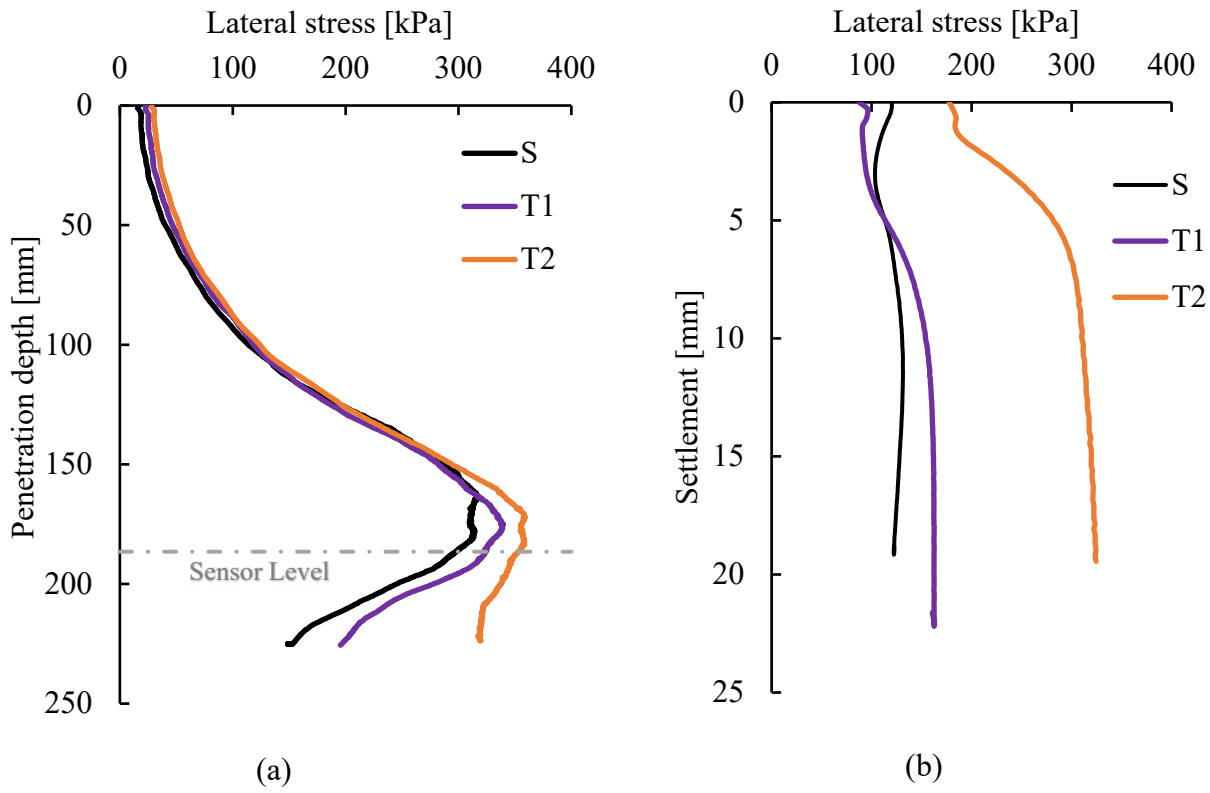

Figure 5.26: Comparison of stress measured from sensor 3C during a) installation b) loading

5.6 Estimation of lateral stress coefficients and β values

The estimation of lateral stress coefficient (K) and shaft friction coefficient (β) is fundamental for evaluating the shaft resistance of piles using the classical β-method which is widely used in geotechnical design. These coefficients relate to the mobilized skin friction along the pile shaft to the effective vertical stress and the interface behavior between the pile and the surrounding soil.

In this approach, the apparent friction is used to calculate the skin friction:

$$f_s = \beta \sigma'_{v0} \quad 5.1$$

$$\beta = K tan(\delta_{cv}) = \frac{\sigma'_n}{\sigma'_{v0}} tan(\delta_{cv}) \quad 5.2$$

where: f_s = skin friction; β = shaft friction coefficient; σ'_{v0} = initial vertical stress; K = lateral stress coefficient; δ_{cv} = constant volume angle of interface friction; σ'_n= mobilized normal stress.

Figure 5.27a-c shows the local values of lateral stress coefficient K (i.e., σ'_n/σ_{v0}) and the β coefficient along the pile shaft at two stages: immediately after installation (the "moving" state) and after unloading (the "stationary" state).

The values of K increase toward the middle of the pile in all cases, with the highest values recorded during the moving state. For the standard (S) wall (Figure 5.27a), maximum K reaches approximately 5. In contrast, the tapered T1 and T2 walls (Figures 5.27b and 5.27c) show higher stress mobilization, with local K values of approximately 9 and 23, respectively. In the upper part of the shaft and near the base, the mobilized K values are considerably smaller. Based on estimated local values along the shaft, the average K values were approximately 3.5 (S wall), 7 (T1 wall), and 12 (T2 wall). These indicate that tapered geometries significantly enhance the lateral stress coefficient up to 2–4 times more than that of the straight wall.

The β values were calculated using normal contact stress measured in the centrifuge tests and interface friction angles obtained from ring shear tests on smooth steel–Fontainebleau sand under constant normal loads. These ring shear tests were conducted under large displacement conditions to simulate real interface behavior. The critical interface friction angle was observed to decrease slightly with increasing normal stress, ranging from 14.2° at 100 kPa to 13.5° at 400 kPa.

For the moving state, the average β values are approximately 0.45 for the S wall, 0.75 for the T1 wall, and 1.5 for the T2 wall, with peak values occurring at mid-depth, 0.6, 1.0, and 1.8, respectively. The corresponding values for the stationary state are lower across all wall types. These results show that the β coefficients for tapered walls are more than twice as high as those for the straight wall, resulting in higher skin friction (Figures 5.27a-c). This enhanced frictional resistance confirms the greater contribution of shaft friction to the bearing capacity in tapered piles compared to straight ones.

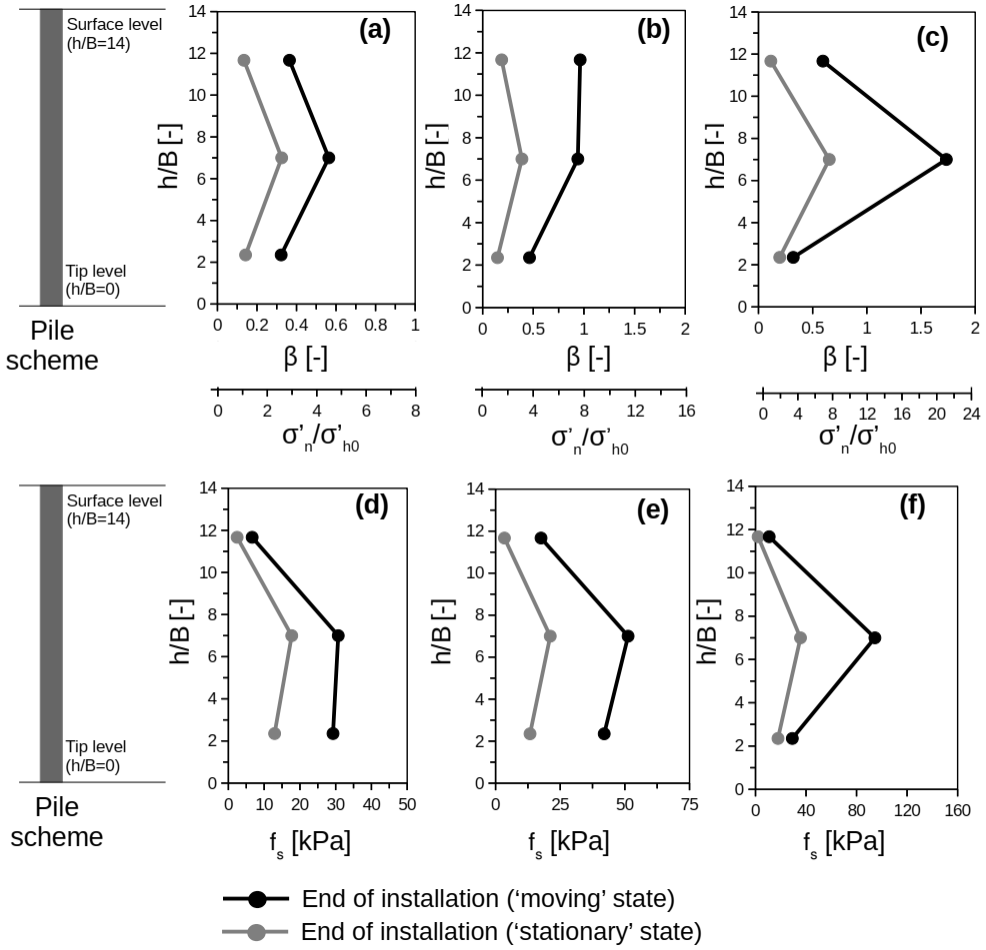

Figure 5.27: Distribution of β coefficients (a-c) and unit friction resistance (d-f) along the pile shaft for S wall [(a) and (d)], T1 wall [(b) and (e)], and T2 wall [(c) and (f)].

To quantify the effect of pile geometry on shaft resistance, a taper coefficient (K_t) was introduced following the approach of Naggar & Sakr (2000). This coefficient expresses the ratio of shaft friction mobilized on tapered walls relative to that on the straight wall and is defined as:

$$K_t = \frac{unit\ shaft\ friction\ of\ tapered\ piles}{unit\ shaft\ friction\ of\ straight\ piles} \quad 5.3$$

In this study, K_t is approximated using the ratio of mobilized normal stresses acting along the wall shaft for tapered and straight walls, assuming that shaft friction is proportional to normal stress.

The coefficient was calculated along the wall shaft at different loading phases (end of installation and stationary) using contact stress measurements from the centrifuge tests. Figure 5.28 shows the taper coefficient K_t plotted along the wall shaft. For the T1 wall (Figure 5.28a), the highest taper coefficient was observed near the pile head (h/B ≈ 11.65) during the moving state, reaching approximately 3.3. This suggest that upper shaft regions experience greater stress amplification during installation. For the T2 wall (Figure 5.28b), the maximum taper coefficient was registered at mid-depth (h/B = 7). This confirms that the effect of tapering is lanrger when the embedded portion of the wall coincides with its widest geometry.

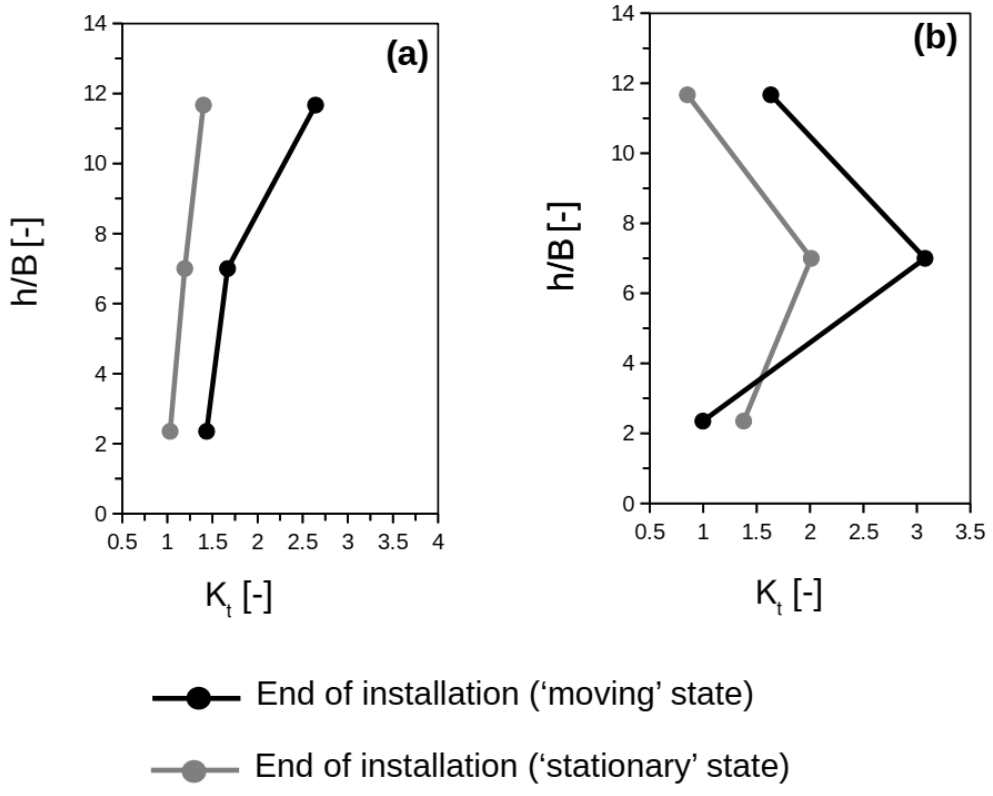

Figure 5.28: Distribution of taper coefficient K_t along a) T1 wall and b) T2 wall

5.7 Comparison with previous studies

The stress measurement of this study can be compared with experimental works of Jardine et al. (2013). They used calibration chamber tests using a mini-IPC pile jacked in dense Fontainebleau sand ($D_r = 0.72$) under a vertical surcharge of about 150kPa, which is considered here as a reference. Only the S wall is considered in this study for comparison with their work.

Figure 5.29 presents the normalized horizontal stress with the normalized position of the sensors with the wall base h/B (h = distance from the wall base, B = average wall breadth). The highest normalized stresses are obtained when the base is about one diameter above the position of the sensors, i.e., for h/B = -1, which is in agreement with observation by Foray (1991) and Yang et al. (2014) in calibration chamber tests. The ratio σ_n/q_c is close to 6÷7% for the standard wall, and it approaches 5.5÷6.5% and 4.5÷6% for the T1 and T2 walls, respectively. For sensors 2B and 2C (d/B = 4), the maximum ratio σ_n/q_c is almost two times lower than for d/B =2.

The maximum normalized horizontal stress recorded for the S wall at d/B = 6 (sensor 3C) is approximately 2.6%. In comparison, the mini-ICP tests reported by Jardine et al. (2013) recorded a slightly higher maximum normalized horizontal stress of about 3.2% at a greater radial distance from the pile axis ($r/R \approx 8$). Although the sensor locations are not directly equivalent, the values are within a similar range.

While this study concerns plane-strain conditions, one can expect lower values of stress in comparison to the axisymmetric state (as in the mini-IPC case) due to the geometric dependence of the lateral stiffness of the pile-soil interface. This lateral stiffness is the highest for the small diameter model and decreases with W/B aspect ratio (W = wall width, B = wall breadth).

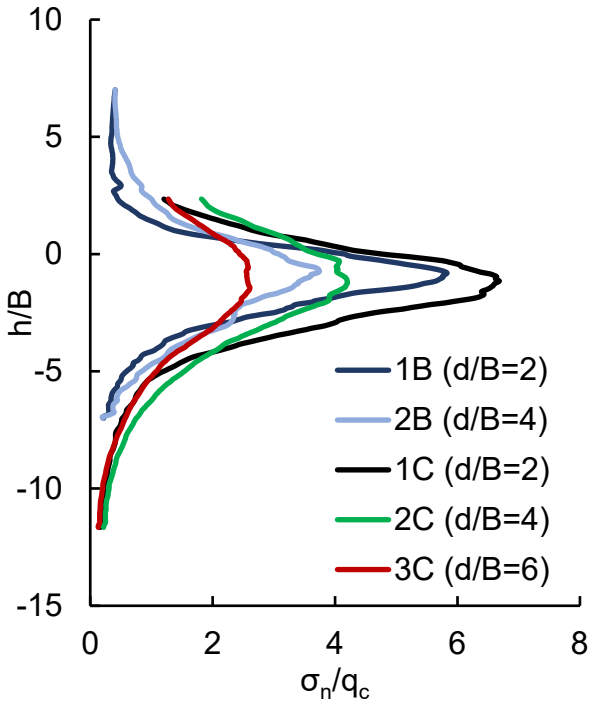

(a)

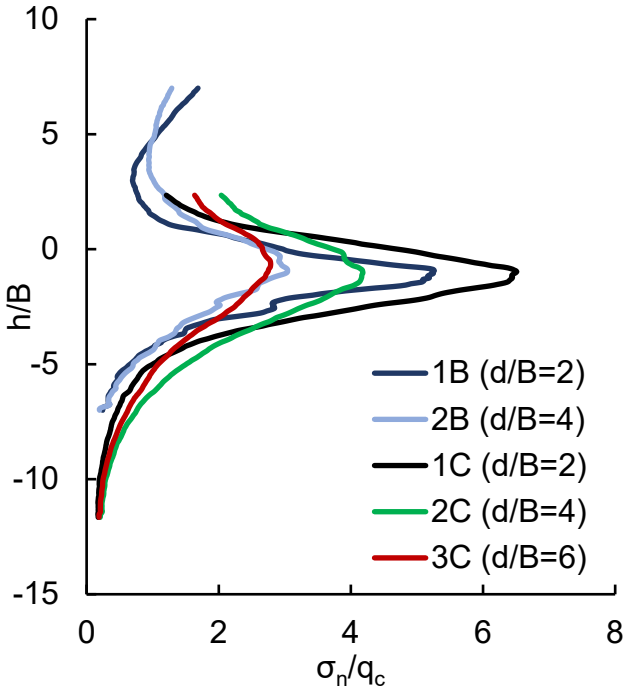

(b)

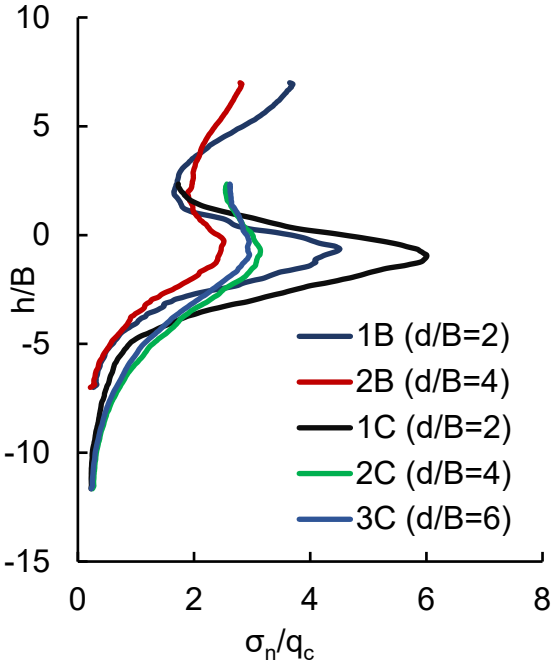

(c)

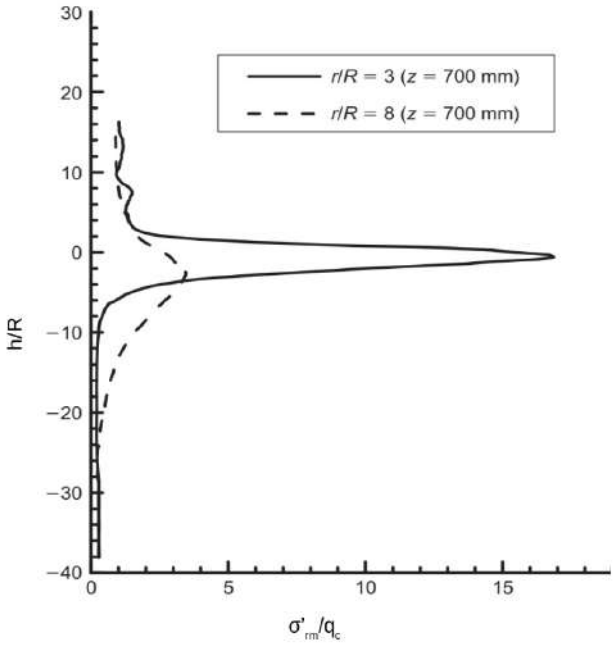

(d)

Figure 5.29: Lateral stress normalized with cone resistance versus normalized depth (h positive above wall base, B = wall breadth, d = distance from the wall axis) (a) S wall, (b) T1 wall, (c) T2 wall d) (Jardine et al., 2013a, 2013b).

The profile of stresses after installation (stationary), normalized with cone resistance is presented in Figure 5.30. The profiles are similar to those reported for mini-ICP (Jardine et al., 2013; Yang et al., 2014). The maximum normalized stationary stresses (σ_n/q_c) for S wall ($\sigma_n/q_c \approx 0.8$ for d/B=2) are lower than those presented by Jardine et al. (2013) for Mini-ICP ($\sigma_n/q_c \approx 2$).

The distributions for the C sensor level (h/B=2.35) are very similar. Maximum values are observed further from the wall, with much lower values recorded at the wall surface. This means that higher horizontal stress is usually mobilized during the model penetration in the vicinity of the axisymmetric pile compared to the S wall. Still, it attenuates with more distance than in the case of plane-strain conditions. The geometric decay of induced horizontal stress with distance from the pile shaft can explain more pronounced stress attenuation in axisymmetric conditions. Due to differences in boundary conditions (plane-strain instead of axisymmetric state) and installation mode, the results may be judged as comparable.

A comparative centrifuge study by Ezzeddine (2024) investigated stroke-based (cyclic) installation under similar conditions using the same model wall in Fontainebleau NE34 sand. The results showed that cyclic jacking produced a more distributed and relaxed stress field around the wall, with lower peak stresses and less pronounced stress re-mobilization.

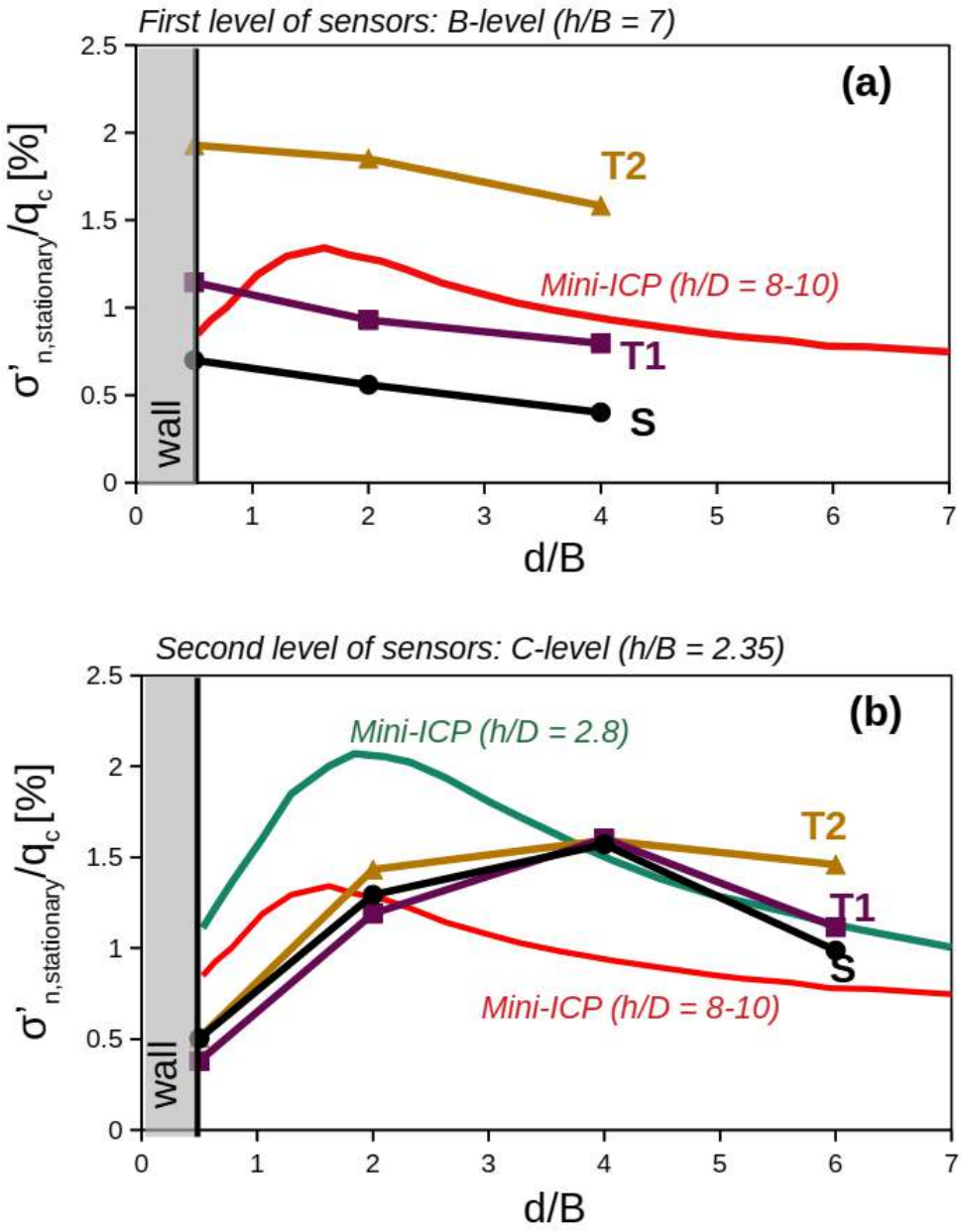

Figure 5.30: Distribution of stationary stress normalized with the cone resistance (d = distance from the wall axis; B = average wall breadth; h = distance above the pile tip; D = pile diameter) for B level (a) and C level (b)

5.8 Summary

The evolution of both the horizontal stress in the soil mass and the normal stress on the wall surface was measured during monotonic installation and static load test in compression using embedded sensors in the soil mass and on the wall-soil interface. During wall penetration, the horizontal stress in the soil mass and normal stress at the wall surface change significantly depending on the wall shape and penetration depth. The maximum value of horizontal stress in the soil mass is observed when the base of the model approaches 1B to the sensing level.

Different patterns of horizontal soil stress mobilized during wall penetration as a function of taper angle. While a continuous decrease of stress to the level prior to the end of installation is observed for straight walls after the base has passed the sensing level, a slight re-mobilization of the stress is noticed for tapered models. The re-mobilization rate increases with taper angle. In case of tapered wall T2, the horizontal stress stabilization after the wall base has passed 7B below the sensing position. This distance will probably be larger for the walls with a smaller taper angle. The horizontal stress evolution during the monotonic installation of the models confirms high overconsolidation of the soil mass after the passage of the wall base. Important installation effects are observed for continuously pushed-in walls, resulting in high level of contact stress at the end of penetration and during static compression loading, especially at the mid-height of the model.

The investigation of the stress development at the wall surface and in the soil mass has shown the mechanism of load transfer. Larger normal contact stress induced during monotonic penetration of the tapered wall results in more than two times higher lateral stress coefficient and shaft friction. The lateral stress coefficient (K) is higher at mid-depth for all wall types compared to regions near the bottom and base of the wall. Significantly higher values were observed for the tapered walls i.e two times higher for T1, and more than three times higher

for T2. The maximum taper coefficient (K_t) values reached 2.7 for the T1 wall and 3.0 for the T2 wall.

As the end-bearing mechanism dominates, the lower base area of tapered walls does not compensate for the increased lateral friction mobilized on the wall. As a result, the overall bearing capacity of tapered walls in compression was 10% and 20% lower for the T1 and T2 models, respectively, than for the straight one. One should notice that the models with quite low slenderness, equal to 14, were used in the present study. The application of longer piles with higher surface roughness could substantially increase the contribution of shaft friction to the overall bearing capacity of the models.

CHAPTER SIX

6. Soil displacement and strain fields

6.1 Introduction

Image-based analysis of soil deformation patterns and strain fields around the model walls was done using Particle Image Velocimetry (PIV). The PIV analysis was performed using GeoPIV, a MATLAB-based tool by White and Take (2002). GeoPIV applies PIV principles to extract displacement data from sequences of digital images captured during experiment. It operates by tracking the texture and the spatial variation of brightness within an image of soil through a series of images. The study includes vertical and horizontal displacement components and shear and volumetric strain distributions. The analysis considers three stages of the wall installation, i.e., when it reached the depths of 112mm (B-level sensor), 186.5mm (C-level sensor), and the final embedment of 224 mm. These depths correspond to the specific levels at which the pressure sensors have been placed in the soil mass (see Chapter 5).

6.2 Soil displacement during installation

6.2.1 Horizontal displacement

The horizontal displacement contours of the soil during installation are shown on the right-hand side of Figures 6.1 to 6.3. Figure 6.1 presents the contours when the wall reaches the B-level, Figure 6.2 corresponds to the C-level depth, and Figure 6.3 shows the contours at the final installation depth. The stress cell positions within the soil mass are indicated on the graphs. The contours of 1, 2, and 4mm of soil displacements were chosen for the presentation.

Moderate and relatively uniform lateral displacements around the wall surface were obtained for the straight wall (S). However, both tapered walls (T1 and T2) exhibited reduced horizontal displacements near the wall tip and larger horizontal displacements near the wall surface. The decrease in lateral displacements near the wall tip was more pronounced for the taper angle of 0.75 degrees (T1). The highest spread of horizontally displaced soil is observed near the surface for a given penetration depth. Moreover, the horizontal displacements near the surface increase with the taper angle of the wall, i.e., the highest level of horizontal displacement is observed close to the T2 wall. The most considerable horizontal extent of the line, '1mm', can be noticed for the latter due to imposed lateral displacement, especially at the final wall embedment. The line '1mm' lateral extent approaches 15B at the final wall embedment.

6.2.2 Vertical displacement

Figures 6.1 to 6.3 show the vertical displacement contours of soil during installation at different levels of wall penetrations on the left-hand side. The contours of positive (downward) and negative (upwards) 1, 2, and 4mm of soil displacements were chosen for the presentation. Additionally, the zero displacement line, which separates the zones of upwards and downwards displacement, is traced.

These vertical displacement contours are characterized by surface-level soil heave and a progressing "bulb" near the wall tip. The standard wall exhibits the most pronounced vertical displacements at the wall tip, forming the most significant vertical displacement "bulb" around the wall and showing the least surface heave. As the taper angle increases, the vertical displacement field is redistributed, and the surface heave becomes more prominent. In contrast, the extent of the displacement "bulb" along the wall is reduced due to the smaller base breadth. The line 'zero displacement' is getting deeper with the taper angle. This line is getting deeper with wall embedment.

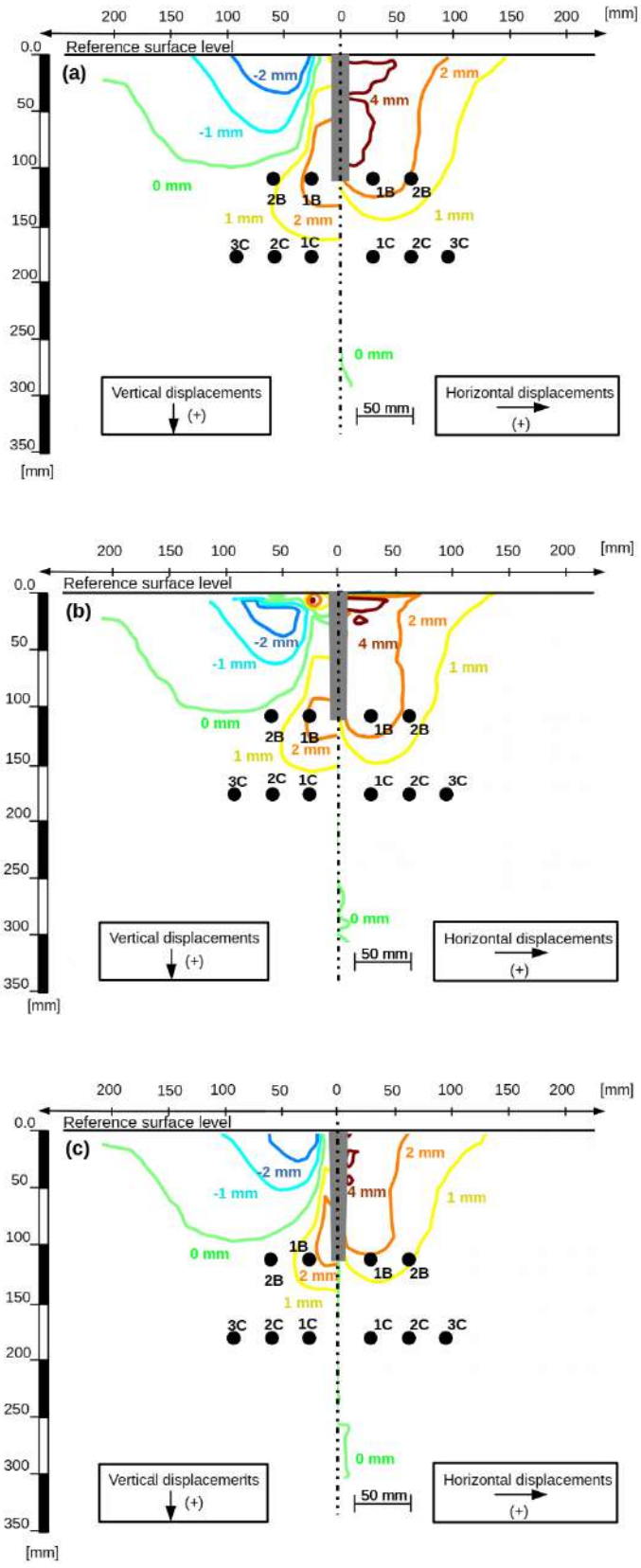

Figure 6.1: Vertical and horizontal displacement fields (model scale) when the wall base is at the first sensor level (B-level): (a) S wall, (b) T1 wall, and (c) T2 wall

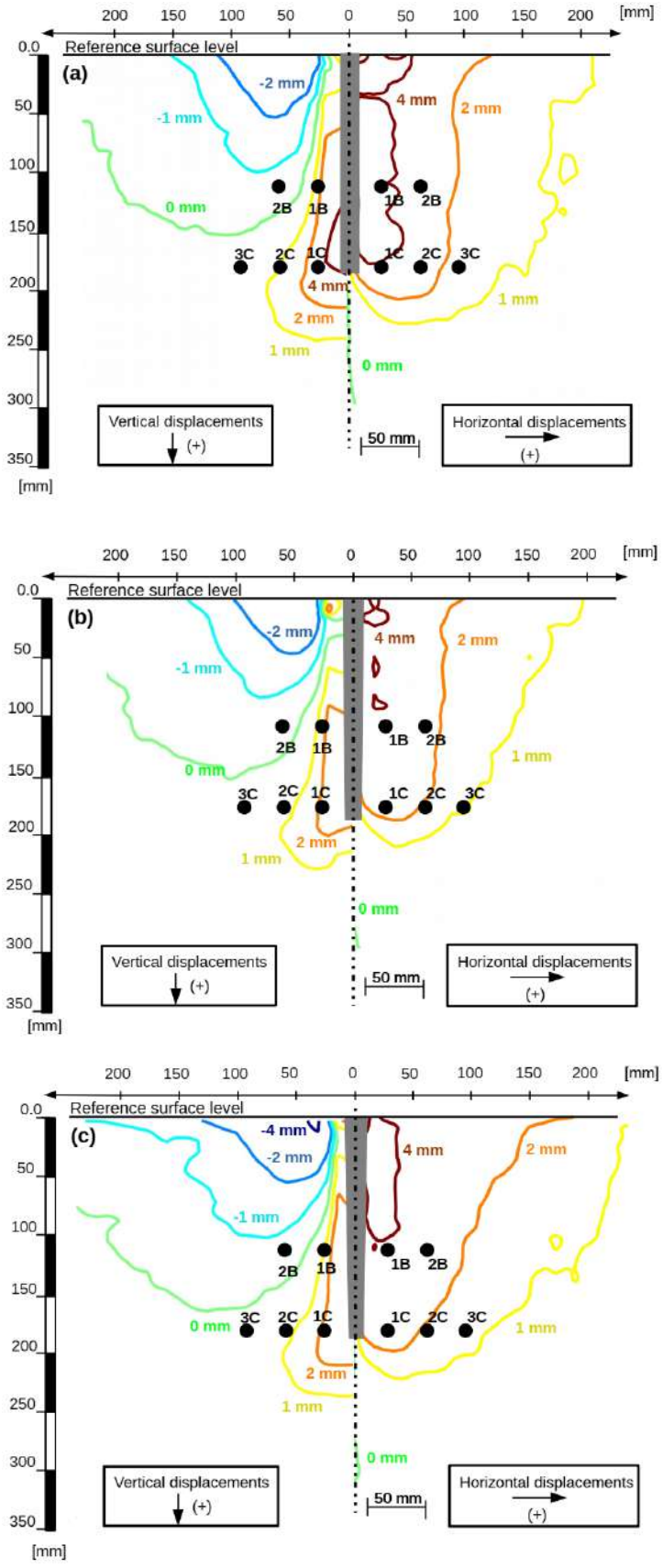

Figure 6.2: Vertical and horizontal displacement fields (model scale) when the wall base is at the second sensor level (C-level): (a) S wall, (b) T wall, and (c) T2 wall

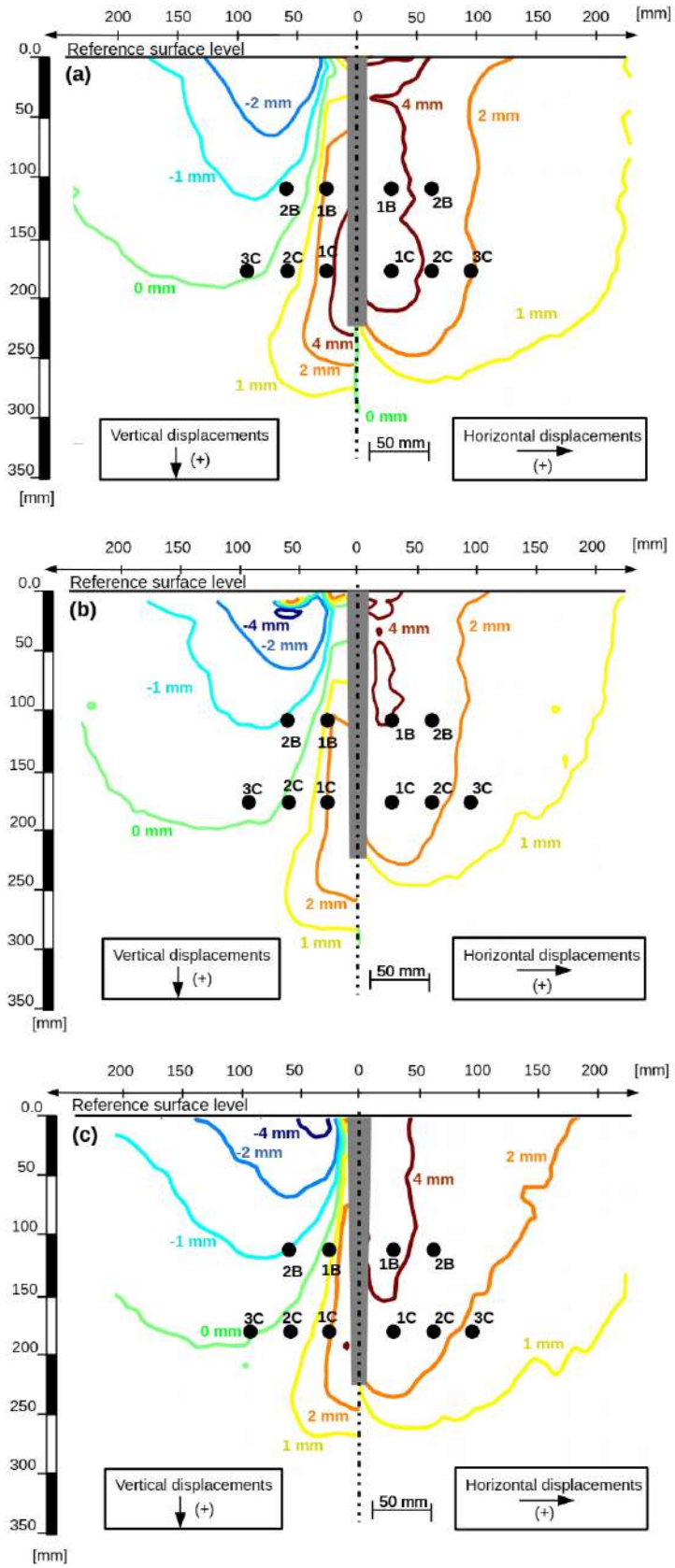

Figure 6.3: Vertical and horizontal displacement fields (model scale) when the wall base is at final penetration level: (a) S wall, (b) T wall, and (c) T2 wall

6.2.3 Comparison of soil displacement with similar studies

The straight wall (S) results can be considered a benchmark for qualitative comparison with some previous studies. For instance, Arshad (2014) presents the experiments on a conical straight axisymmetric pile (31.75mm in diameter). During the pile installation in medium dense sand (D_r = 65%) at a depth of 10D (D = pile diameter) and distance h/D=2 above the pile tip, they measured vertical displacement around the pile surface as approx. 3mm at 1D and approx. 0.5 mm at 4D from the pile axis. In this research, at a similar depth of 11B (C-level) and the same distance from the pile tip (h/B=2), the vertical displacements of 4mm and 0.5mm can be noticed at the distances of 1B and 4B from the wall axis, respectively.

Similarly, slightly higher values occur in terms of horizontal displacements. The equivalent displacement zones in plane-strain (PS) conditions in our research are similar in the close vicinity of the wall in the axisymmetric (AX) conditions. The PS conditions return much higher horizontal displacement at a larger distance than AX conditions. For the horizontal displacement of s_h = 3.5 mm at 1D and s_h = 0.8 mm at 4D (where s_h = horizontal displacement) in the reference research (Arshad et al., 2014), s_h = 4mm at 1B and s_h = 3 mm at 4B are obtained in this study. It signifies more pronounced displacement attenuation with distance from the model in AX than in PS conditions. Larger displacements in PS than in AX conditions were also found by Liu (2010) in centrifuge tests on the installation of piles and walls in sand. Bearing all the mentioned notes in mind, the displacement fields during the insertion of the straight wall elaborated in our study can be judged similarly to other studies concerning PS and AX conditions. No equivalent reference study concerning the soil displacements near the tapered piles and walls exists.

6.3 Strain fields during installation

6.3.1 Shear strain

The contour maps of shear strain at the end of installation for each wall type are shown on the right-hand sides of Figures 6.4a, b, and c. Very intense shear strain is concentrated near to pile, with a magnitude of more than 20% in the area of 1B around the pile. Outside this zone, the shear strain level reduces with distance from the wall (i.e., 5% for 7B) and becomes negligible at around 10B (shear strain lower than 1~2%). At this distance, it can be seen that the shear strain is about 2% for the S-wall, assuming that the walls would have an isolated wall behavior with no interaction with adjacent ones.

The shear strain equal to 1% can be considered a noise level in this PIV analysis (it was allowable precision with the setup used). The shear strain contours for tapered walls are slightly narrower. Although the extent of the 10% shear strain zone is similar for all wall shapes, the 5% shear strain contour is narrowed to a distance of 5~6B and 4~5B from the wall for T1 and T2, respectively. The wall base area also shows a significant reduction in the spread of the shear strain zone.

6.3.2 Volumetric strain

The contours of volumetric strains at the end of installation for each type of wall (S, T1, and T2) are shown on the left-hand side of Figure 6.4a, b, and c. A significant compression zone (approx. 1B wide) around the walls is observed for all wall types. However, they are more distinct for tapered models. This is typical behavior where the insertion of a displacement pile produces densification of the neighboring soil (Stuedlein et al., 2016).

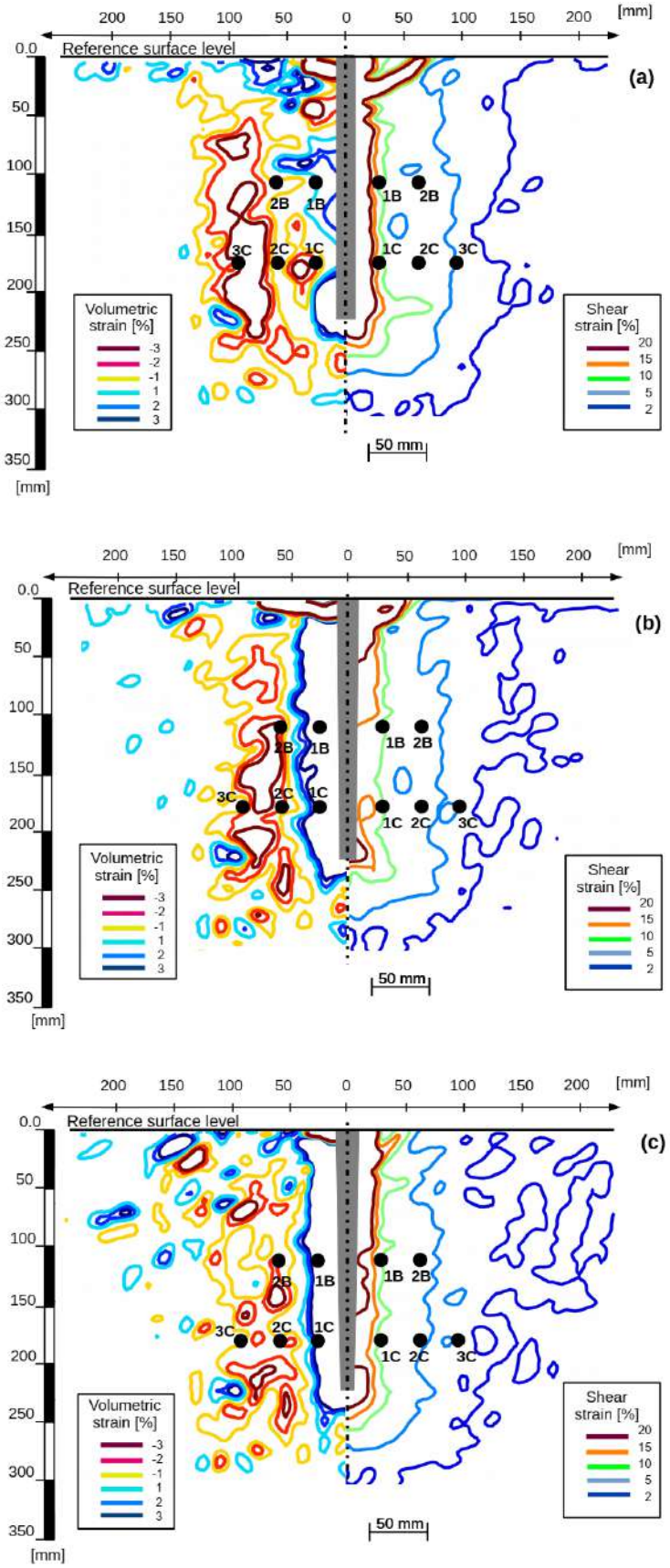

Figure 6.4: Volumetric and shear strain fields at final penetration depth: (a) S wall, (b) T wall, and (c) T2 wall

In case of tapered walls, this mechanism is more developed by the additional imposed lateral displacement due to the wall shape. Outside this region, the zones of contraction and dilation can be observed. The largest dilation zone can be noticed at a distance of about 4~5B outside the S-wall surface. The dilation zones are localized closer to the tapered walls. Such dilative behavior could be related to the path of soil particles moving during the model installation from the zone of very high stress near the base to the zone of small stress level at some distance from the pushed-in wall, as it was suggested by White and Bolton (2004). It could also be associated with consecutive failure mechanisms in the soil mass when the wall is pushed into the soil. The resulting soil dilation is produced within the consecutive overlapping shear zones. In this way, the installation of tapered walls densifies the soil nearby (contraction zone at a distance 1~2B), but some part of the soil (in the range of 4~8B) is slightly loosened (dilation zone).

6.3.3 Comparison of strain fields with similar studies

The shear strain contours for the straight wall are slightly similar to the experimental data concerning piles presented by Fu et al. (2023), but they are significantly wider. These observations are related to the different boundary conditions in both cases. The obtained shear strain pattern also fits the results of White and Bolton (2002) for loose silica sands. These values cannot be compared directly, but the same trend is maintained.

The phenomenon of soil contraction near the penetrating straight wall was previously observed by White and Bolton (2004) and White (2002). The latter presented the zones of contraction and dilation in detail, especially in the vicinity of the pile base. Taking into account his findings for medium dense sands (D_r = 64% and D_r =55%), one can observe that the zones of contraction near the wall and dilation at farther distances to the wall are qualitatively comparable to this research.

The position and shape of contraction and dilation zones are also similar to the results of White and Bolton (2002) for loose silica sands. They found that contraction dominates even at 3.5B from the pile axis. For the dense sand in this research, this zone is narrower and is limited to approximately 2B. One can also notice a high gradient of volumetric strain at a distance of 2~3B from the T1 wall between the zones of contracting and dilative soil. Moreover, a relatively uniform shear strain field is observed near this wall. It could be related to a smoother 'laminar' installation of the T1 wall than the other models, where more disturbance is introduced in the soil mass.

6.4 Displacement of soil particles

The evolution of the horizontal displacement of soil particles at four positions is given in Figure 6.5. The horizontal displacements are larger for a measurement point closer to the wall (Figure 6.5a and c versus Figure 6.5 b and d). The displacement within the soil increases sharply up to the point when the wall base passes the sensor level, and this increase continues until the wall reaches a depth of 1B. Afterward, the further horizontal displacement of the soil particles is much smaller. Shortly after passing the sensor level, the horizontal displacement becomes nearly constant for the S-wall. For the T1 wall, a slight increase in horizontal displacement is observed after the wall has passed the B-level. In the case of the T2-wall, the horizontal displacement uniformly increases throughout penetration with only slightly reduced slope inclination when the sensor position has been reached.

The backbone-type curves obtained for S-wall are very similar to the deformation patterns measured around the piles in AX conditions reported by Fu et al. (2023), Arshad (2014), and Tehrani et al. (2018). However, those studies show only the results for loose (Dr = 45%) and very dense (D_r = 85%) sands on similar depths (z/D = 9~13) and radial locations (r/D = 1~1.5D).

The measurements for S-wall fit closer to the dense state, but the observed difference can be attributed to the different boundary conditions mentioned before. Quantitatively, the results obtained for S-wall can be judged as being proper.

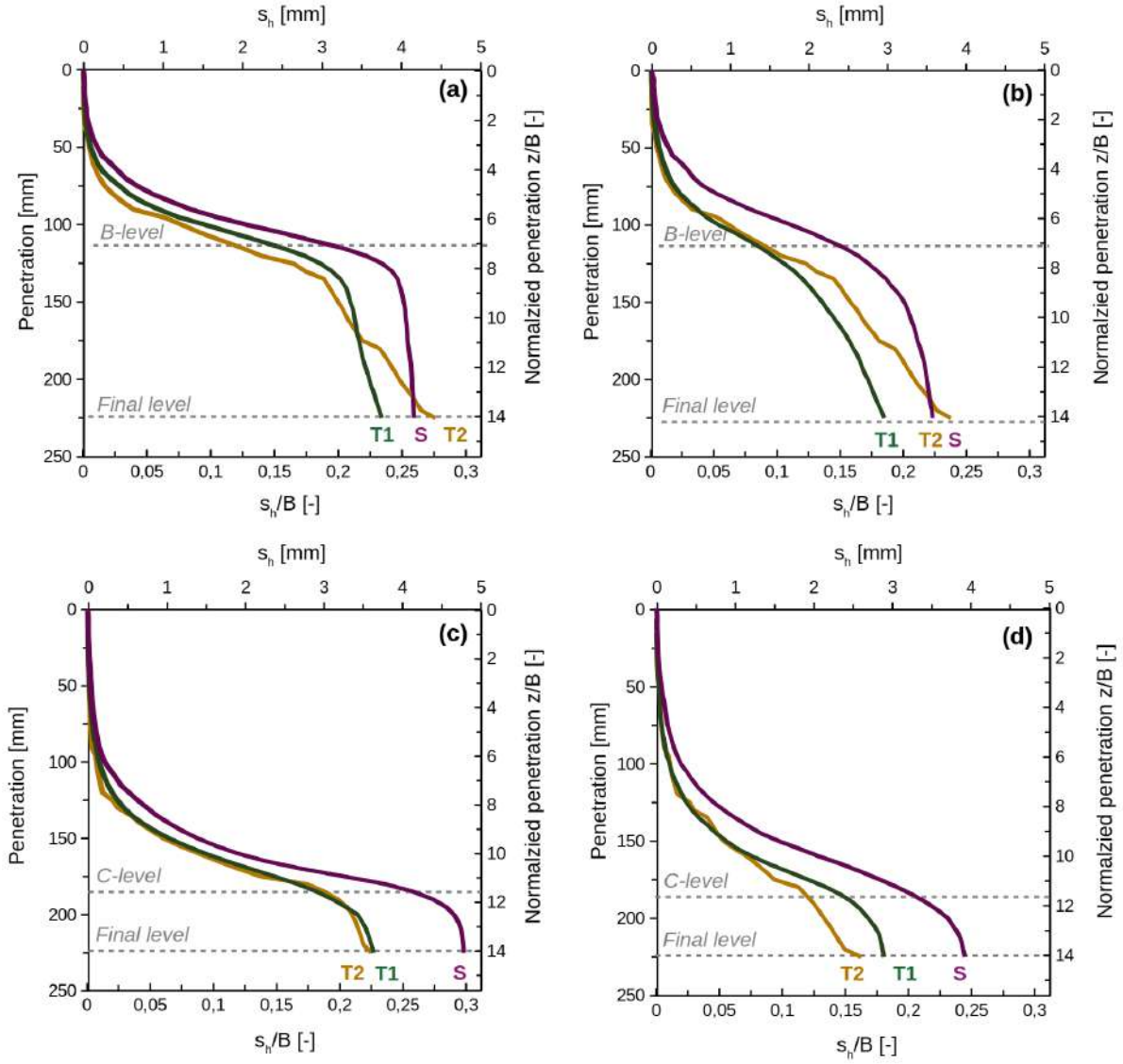

Figure 6.5: Evolution of horizontal displacement of soil particles during penetration of walls: (a) 1B location (z/B=7, d/B = 2); (b) 2B location (z/B=7, d/B = 4); (c) 1C location (z/B=11.65, d/B = 2); (d) 2C location (z/B=11.65, d/B = 4).

The soil particles trajectories for sensor positions are presented in Figure 6.6. The maximum downward movement is observed for the soil element close to the wall (d/B=2) when the model base has reached the given sensor position (h/B=0). However, for the soil element far from the wall (d/B=4), this maximum downward movement of the soil particle is measured before the wall base has passed the sensor level. Then, the upward movement of soil elements is recorded following the penetration of the models. It can be noted that larger downward displacements occur in the case of the straight wall than for the tapered ones, which is in line with the bulb observation in Figure 6.3. Similarly to horizontal displacement, the vertical ones are bigger for measurement points close to the wall.

Based on volumetric strain contour and displacement fields, the tentative scheme of volume changes in the mid-height of the wall was introduced in Figure 6.7. The horizontal movement of the soil is the main reason for soil densification. However, the vertical soil movement triggers the final volumetric changes. In the close distance to the pile, the vertical soil movements are neutral or positive to the soil densification, but they produce soil loosening with further distance from the wall. The final volume change is the result of both components of deformation. The relation between the horizontal and vertical components is modified with the taper angle. In the mid-height of fully embedded models with the same breadth, the horizontal soil movement intensifies with the taper angle of the walls. In contrast, the vertical movement remains quite similar for all wall shapes. As a results, the zone of dilative soil is getting smaller for the tapered walls.

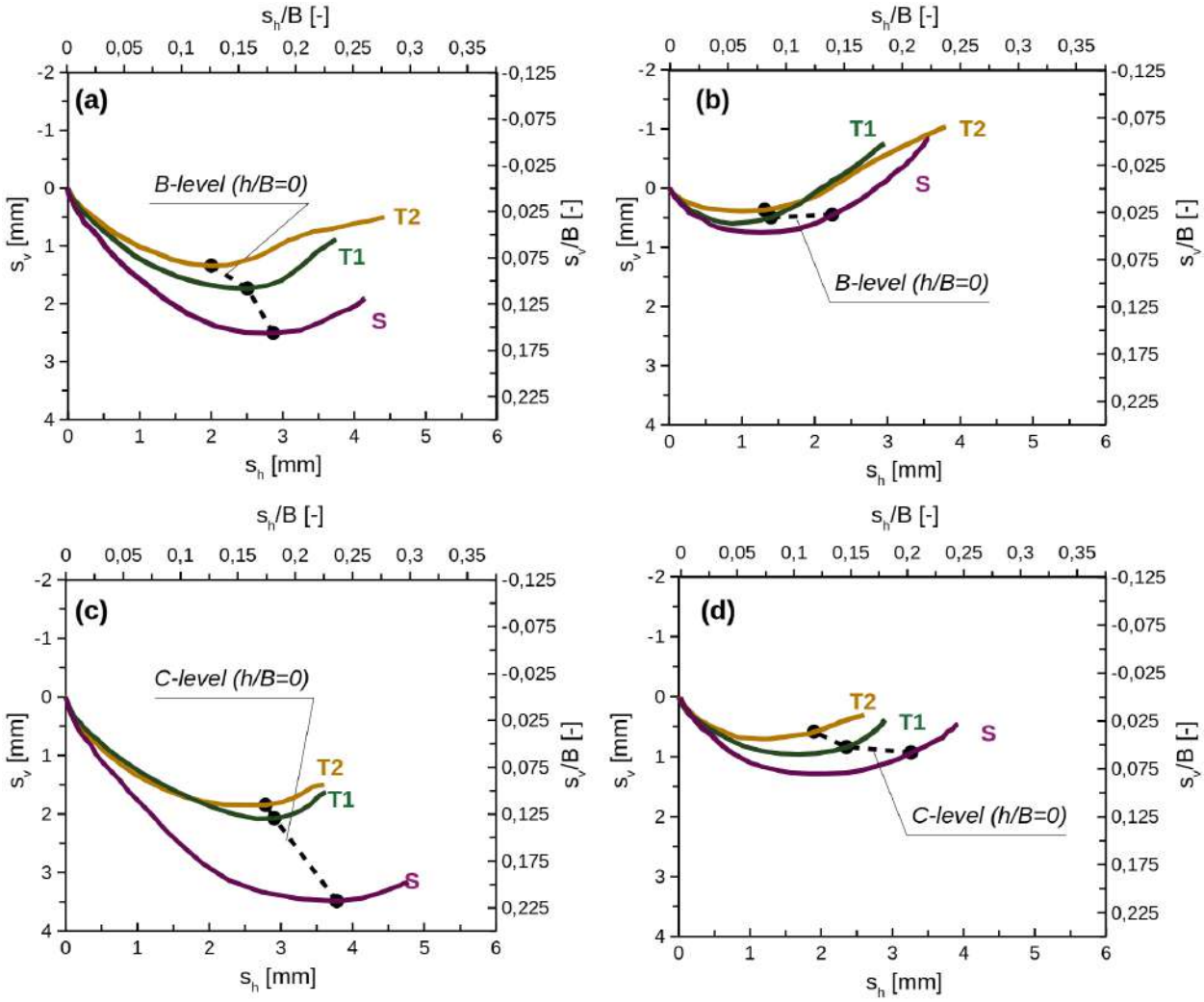

Figure 6.6: Trajectories of soil particles during penetration of walls: (a) 1B location (z/B=7, d/B = 2); (b) 2B location (z/B=7, d/B = 4); (c) 1C location (z/B=11.65, d/B = 2); (d) 2C location (z/B=11.65, d/B = 4). Downward and outward soil displacements are positive.

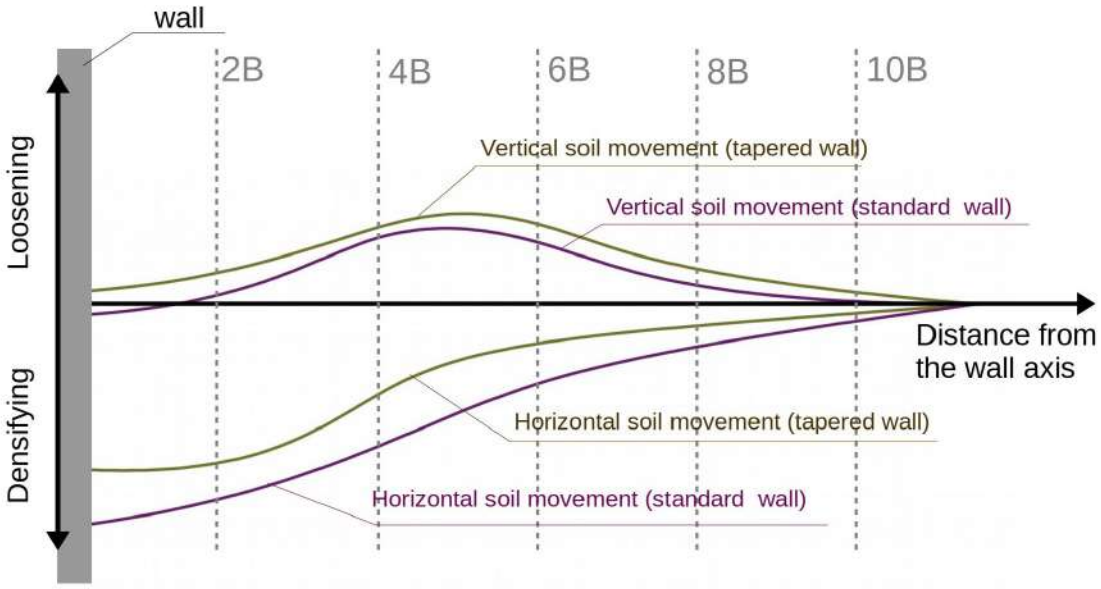

Figure 6.7: Tentative scheme of volume changes in the mid-height of the straight and tapered walls.

6.5 Summary

The displacements and strains developed during the monotonic installation of different-shaped walls was investigated using the PIV technique. Various displacement and strain contour patterns were observed as a function of wall type and penetration depths. The soil zone influenced by the installation is considerably larger for tapered walls than for straight ones. For instance, the zone corresponding to the contour of 2 mm horizontal displacement at the end of installation (s_h/B=0.125) varies in a range from 10B near the soil surface to 3B near the wall base for T2-wall and from 6B near the soil surface to 5B near the wall base for S-wall. In the case of the tapered wall (especially T2), the horizontal displacements near the soil surface are well pronounced. However, they are significantly reduced near the wall tip compared to the straight model (they are twice smaller at the distance of 1B from the wall tip). The lateral extent of the densified zone ('line 1mm' of soil lateral displacement) near the wall at the final embedment is about 15B, regardless of the wall shape. This is significantly greater than the

radial influence zone typically observed in axisymmetric cone penetration tests (Arshad et al., 2014), which extends only 5–8 cone diameters from the penetrometer axis.

Vertical displacement patterns show upward soil movement near the surface and downward movement near the wall tip for all wall types, with the largest vertical displacements observed near the S-wall tip. Soil particle trajectories indicate that the maximum downward movement (for soil at d/B = 2) occurs as the wall base reaches the same depth (h/B = 0). Tapered wall installation results in a more confined shear strain zone near the wall base, densifying the surrounding soil within 1–2B while slightly loosening the soil in the 4–8B range. However, this dilation zone is smaller than the straight wall, indicating better overall soil improvement around tapered geometries.

A notable distinction is observed in the horizontal displacement behavior: for the straight wall, displacement in the soil mass stabilizes once the base passes a given soil element. In contrast, tapered walls continue to induce increasing horizontal displacement beyond that point.

These observations from monotonic installation can be compared with the results of stroke-based (cyclic) installation reported by Ezzeddine (2024), who conducted centrifuge tests under similar conditions using GeoPIV. Cyclic jacking led to broader but less concentrated deformation fields.

CHAPTER SEVEN

7. Numerical analysis of load–settlement and failure mechanism

7.1 Introduction

This chapter presents the results of the numerical analysis conducted to evaluate the bearing capacity of different tapered walls installed in sand. Finite Element Method (FEM) and Limit Analysis (LA) approaches were employed to simulate the behavior of the walls under static loading conditions. First, the FEM results, including the load-displacement behavior, are discussed. This is followed by the presentation of the Limit Analysis results, focusing on determining collapse loads and failure mechanisms. Finally, a comparison between the numerical predictions and experimental findings is provided.

7.2 Finite element method results

7.2.1 Load-displacement behavior

Numerical analyses were performed using the Finite Element Method (FEM) in OPTUM G2. The numerical model was developed under plane strain conditions, assuming rigid wall behavior with soil–rough wall interface properties. The load-settlement behavior of the straight model walls were analyzed using both the Mohr-Coulomb (MC) and Hardening Mohr-Coulomb (HMC) models. The wall was modeled as wish-in-place at a depth of 224 mm (model scale), and thus, the installation effects related to continuous penetration in the sand mass were not considered in the simulation.

The load-settlement curve for the S wall is shown in Figure 7.1. The head load was calculated by multiplying the stress at the top of the wall by the cross-sectional area (breadth × length),

where the wall breadth and length are 16 mm and 200 mm, respectively. The load-displacement curve exhibits a progressive increase in axial load with the settlement, followed by a gradual reduction in stiffness as displacement continues. Initially, the response is nearly linear, showing elastic behavior, after which a nonlinear trend develops as plastic deformation accumulates in the surrounding soil. MC model gives higher values compared to the HMC model.

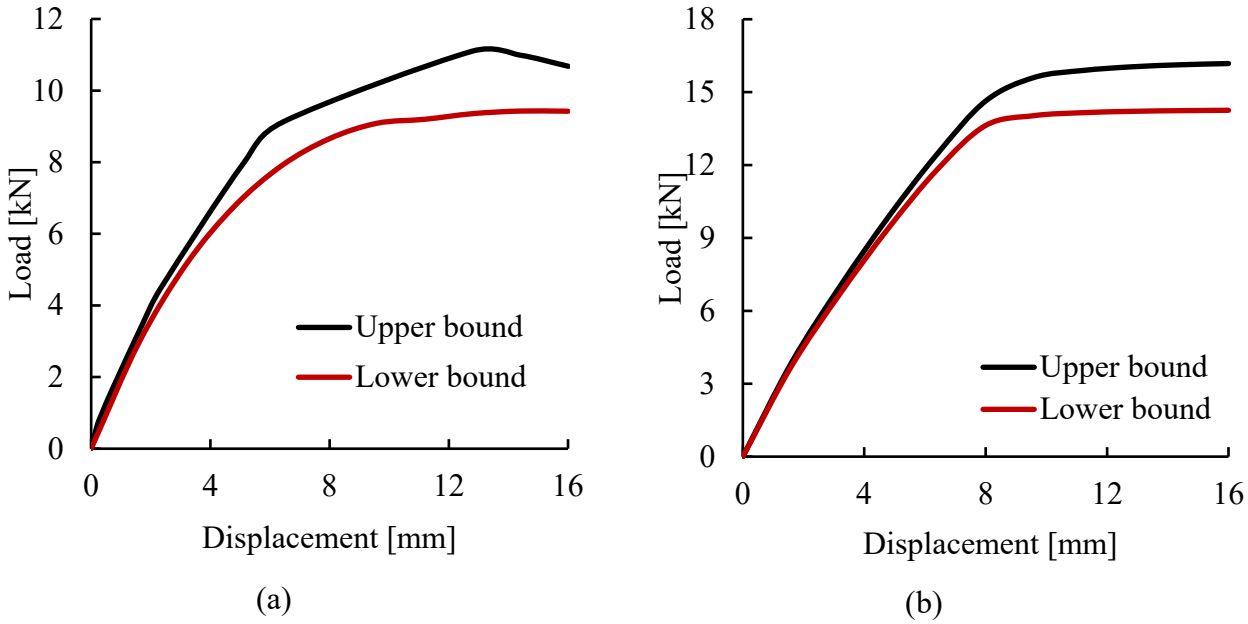

Figure 7.1: Load-displacement curve for S Wall using a) HMC model, b) MC model

7.2.2 Parametric study

The initial parametric analysis was conducted on the S wall to examine the effects of several factors including boundary size, effect of associated and non-associated flow rules, effect of the dilation cap, and the influence of mesh density on load-displacement curves. Additionally, the comparison between the Mohr-Coulomb (MC) and Hardening Mohr-Coulomb (HMC) models was also considered. Following this, the analysis was extended to tapered walls, focusing on how the taper angle affects the load-settlement behavior.

7.2.2.1 Effect of boundary size

The influence of container size on the load-displacement behavior was investigated using FEM analysis. While maintaining a constant domain height of 450 mm, the domain lengths were varied at 800 mm, 1000 mm, and 1200 mm. For this case, the mesh density of 1000 elements was considered. The results in Figure 7.2 show the load-displacement curves for the upper and lower bound values obtained from the HMC and MC models with the associated flow rule. These results indicate that the variation in domain size has a negligible impact on the load-displacement behavior, suggesting that boundary effects are minimal under these conditions**.** Moreover, lower and upper-bound solutions are relatively close to each other.

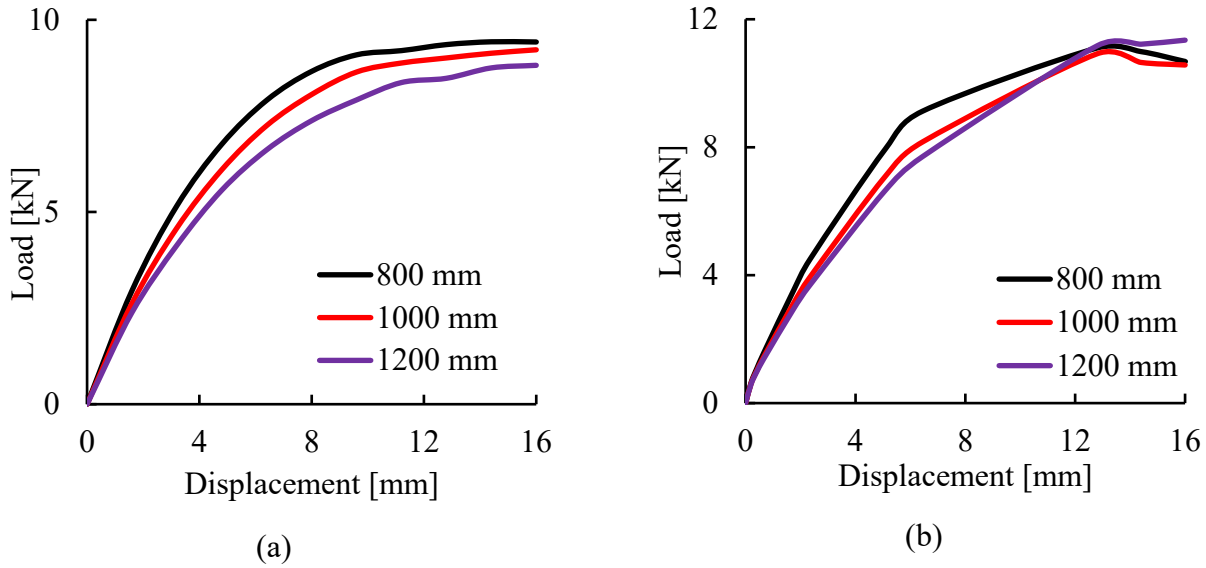

(a) (b)

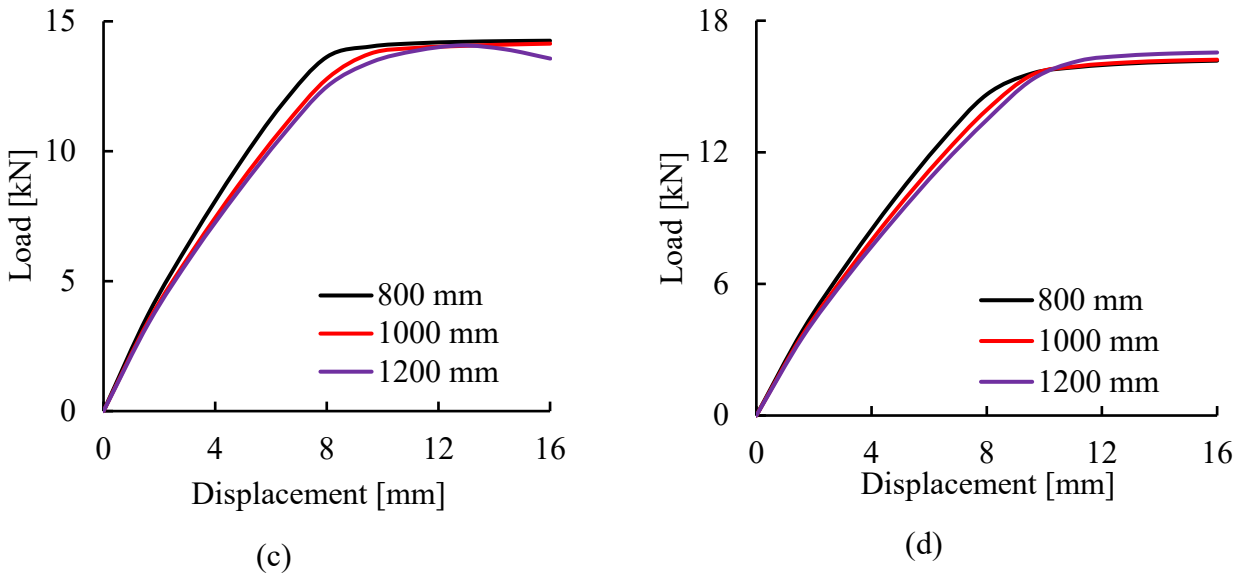

Figure 7.2: Effect of boundary condition (container size) on the load displacement curves (a) HMC–lower bound, (b) HMC–upper bound, (c) MC–lower bound, (d) MC–upper bound

7.2.2.2 Effect of the number of mesh elements

The influence of mesh density on FEM results was analyzed considering four mesh densities: 1000, 2000, 4000, and 6000 elements. The effects were examined for both the upper and lower bounds of the HMC and MC models (Figure 7.3). The analysis shows that as the number of elements increased, the gap between the upper and lower bounds consistently decreased up to 4000 elements. Specifically, the lower bound values increased while the upper bound values decreased, indicating a convergence of results. Beyond 4000 elements, for example, at 6000 elements, this effect became negligible, suggesting that further mesh refinement did not significantly improve the solution (Figure 7.3) but may propagate some numerical errors. That is why the domain of 800mm with 4000 elements was assumed for further analysis.

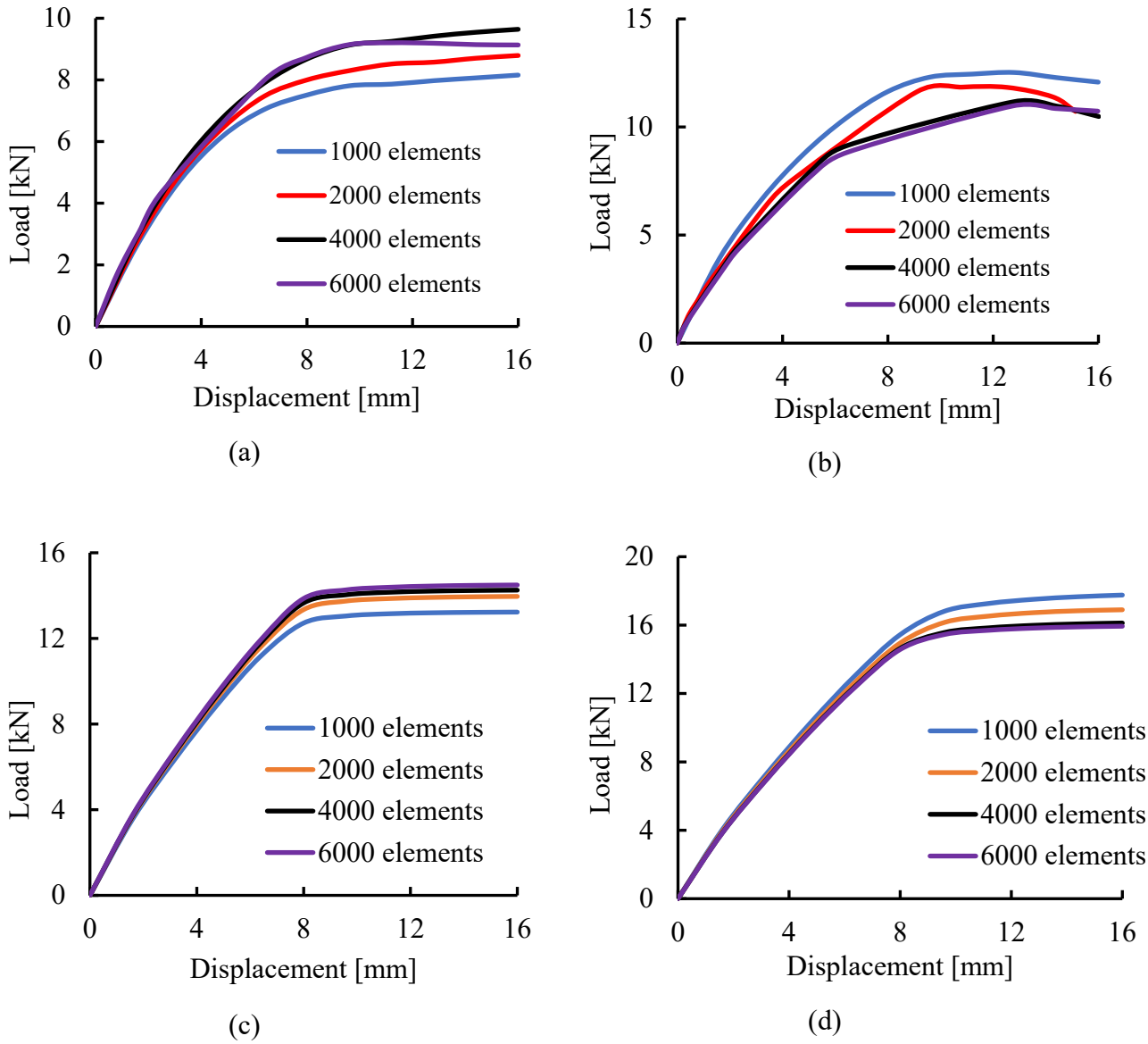

Figure 7.3: Effect of mesh density on load-displacement curves: (a) HMC–lower bound, (b) HMC–upper bound, (c) MC–lower bound, (d) MC–upper bound

7.2.2.3 Associated vs Non-Associated flow for MC model

The difference between associated and non-associated flow rules within the MC model for the sand mass and wall-soil interface was also investigated. Four cases were considered: a) associated flow rule for soil and interface, b) associated flow rule for soil and non-associated interface, c) non-associated flow rule for soil and associated one for the interface, and d) non-associated flow rule for both soil and interface. The results revealed that cases with associated flow rules (a and b) exhibited higher stiffness and load capacity. Among these, Case A

(associated soil and interface) showed the highest response, followed by Case B (associated soil and non-associated interface). Conversely, cases with non-associated flow rules (c and d) exhibited load-displacement behavior with lower stiffness and capacity than those with associated flow rules. Case C (non-associated soil and associated interface) demonstrated higher capacity than case D (non-associated soil and interface), with case D, yielding the lowest load capacity among all. These trends are illustrated in Figure 7.4, where all load-displacement curves (a-d) present the significant influence of flow rules on predicted wall performance.

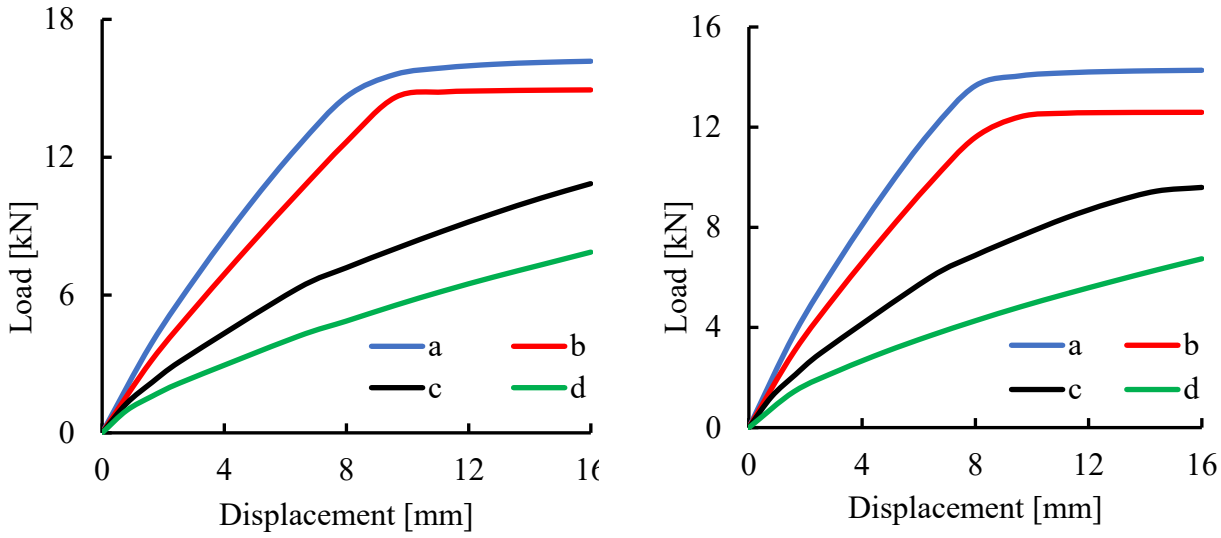

Figure 7.4: Load-displacement curves for different combinations of MC models with associated and non-associated flow rules a) Upper bound b) Lower bound

7.2.2.4 Effect of dilation cap

The effect of considering a dilation cap was investigated for the non-associated Mohr-Coulomb (MC) model and Hardening Mohr-Coulomb (HMC) model. This analysis applied a volumetric dilation ($\varepsilon_{v,cr}$) of unit value to both the soil and the soil-wall interface. The results indicated that including the dilation cap led to slightly lower load-settlement curves than the cases without the dilation cap in both the MC and HMC models (Figure 7.5).

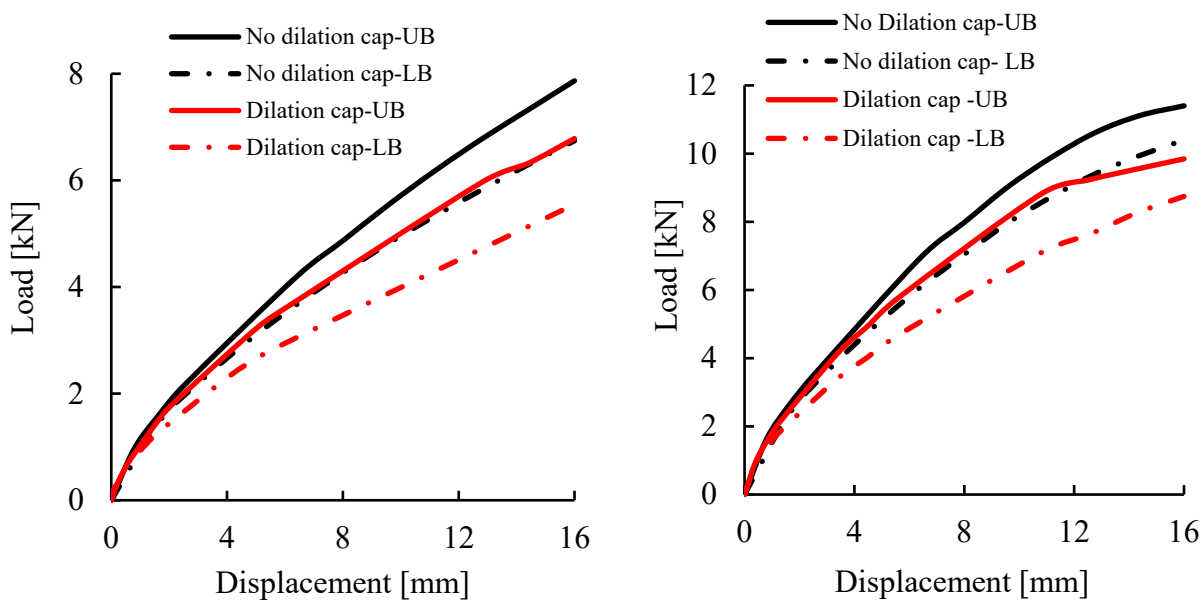

Figure 7.5: Effect of dilation cap on the load settlement curves using a) HMC model and b) MC model

7.2.3 Modeling of tapered walls

After parametric studies concerning the standard wall, the effect of the taper angle on the load-displacement curves was analyzed. Based on findings from the standard walls, a mesh density of 4000 elements was adopted, as it provided optimal accuracy and convergence. Given the negligible impact of boundary conditions previously established, a container size of 800 mm, consistent with the experimental setup, was used.

The load-displacement curves for different taper angles obtained using the HMC model are shown in Figure 7.6. The upper bound solution in Figure 7.6a shows that all wall types exhibit a nonlinear increase in load with displacement, followed by a slight drop near the peak load. The straight wall (S) consistently shows the highest load capacity, reaching approximately 11.3 kN. The T1 wall, with a moderate taper, follows closely behind, while the T2 wall with largest taper angle shows the lowest load response, with a peak load of about 9 kN.

The lower bound solution (Figure 7.6b) also shows a similar trend in load-displacement behavior. The straight wall exhibits the highest maximum load, approximately 9.5 kN, followed by T1 and T2. This consistenty for both analyses confirms the significant influence of taper geometry. Overall, both the upper and lower bound results indicate that the taper angle significantly affects the load-displacement response, with increased taper leading to reduced load capacity.

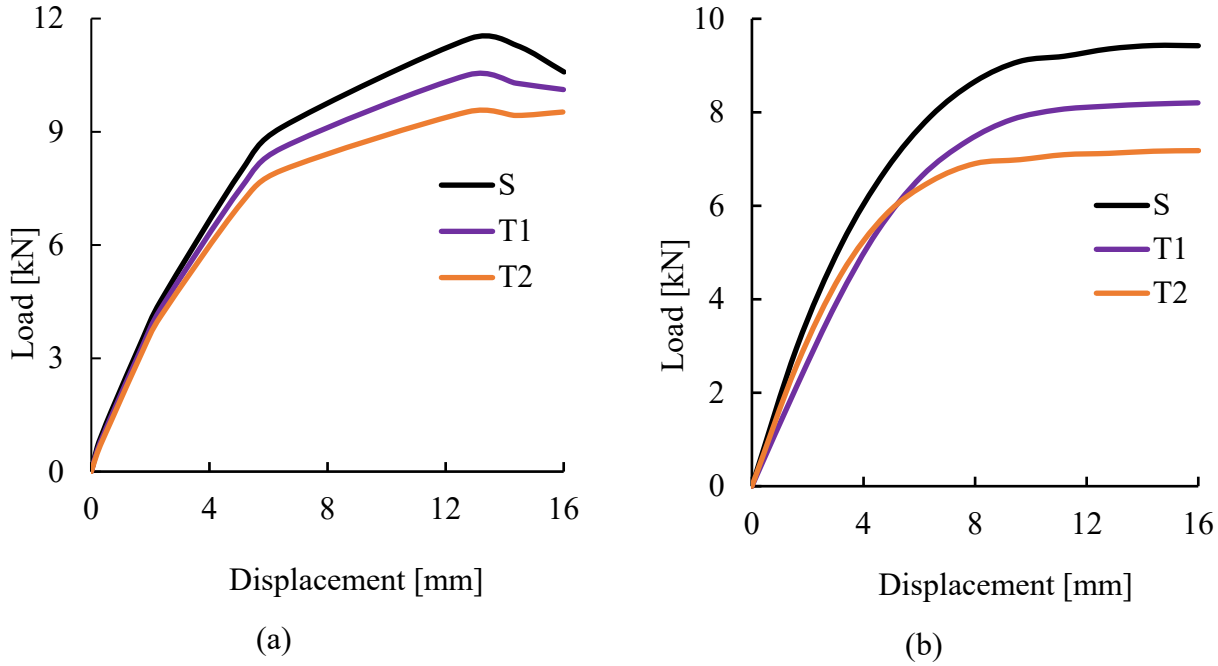

Figure 7.6: Load-displacement curves of walls using HMC model (a) upper bound b) lower bound

7.2.4 Base resistance estimation

Both the Mohr-Coulomb (MC) and Hardening Mohr-Coulomb (HMC) models were used to analyze the stress distribution at the wall base. The base resistance values were computed from the normal stress acting at the base per unit width and are summarized in Table 7.1. It is observed that the MC model gives higher base resistance values compared to the HMC model. For instance, the S-wall exhibits a base resistance of 4.29 MPa with the MC model and 2.01 MPa with the HMC model.

Table 7.1: Base Resistance for all wall types

Wall Type	Model	Normal stress at the base per unit width (kN/m)	Base force (KN)	Base Resistance (MPa)
S	HMC	2014.22	6.446	2.014
	MC	4292.50	13.736	4.293
T1	HMC	2198.00	5.715	2.198
	MC	4343.50	11.293	4.344
T2	HMC	2137.44	4.275	2.137
	MC	4256.90	8.514	4.257

The base resistance results obtained for the S-wall were also compared with analytical estimates. Using theoretical equations (equation 3.7) and table 3.1, the base resistance under both plane strain and axisymmetric conditions was calculated and compared with the numerical values from FEM simulations, as shown in Table 7.2. The calculations were performed for $\phi = 31^{o}$ and δ/ϕ=0.5.

Under plane strain conditions, the analytical base resistance was found to be 3.11 MPa and numerical analysis (FEM) results 4.29 MPa (MC) and 2.01 MPa (HMC). The analytical result lies between the two numerical predictions. For axisymmetric conditions, the analytical method estimated the base resistance to be 18.38 MPa, which is comparable to the value of cone resistance at final penetration depth (Figure 5.2).

Table 7.2 : Comparison of base resistance from numerical and analytical methods

Method	Condition/Model	Base Resistance (MPa)
Analytical	Plane Strain	3.11
	Axisymmetric	18.38
Numerical (FEM)	MC	4.29
	HMC	2.01

7.3 Limit analysis results

The Limit analysis (LA) was employed using Limit State Geo software to investigate the effect of taper angles on the failure load and failure mechanisms under static loading. This analysis provided insights into the effect of wall geometry on load-bearing capacity and the failure mechanisms. The soil was modeled using the Mohr-Coulomb (MC) failure criterion with the associated flow rule. The parameters used for the soil were the same as those used in the FEM analysis.

7.3.1 Collapse (failure) load estimation

The failure load estimated from the Limit analysis for all wall types is shown in Figure 7.7. The straight wall (S) achieved the highest failure load of 18.78 kN, followed by the moderately tapered (T1), which reached 14.68 kN. The sharply tapered wall (T2) exhibited the lowest failure load of 12.9 kN. This trend is consistent with the findings from FEM analysis, confirming the significant effect of pile geometry on load capacity. The results shows that the straight pile (S) has the higher load-bearing capacity due to its largest base area and tapered walls has lower values.

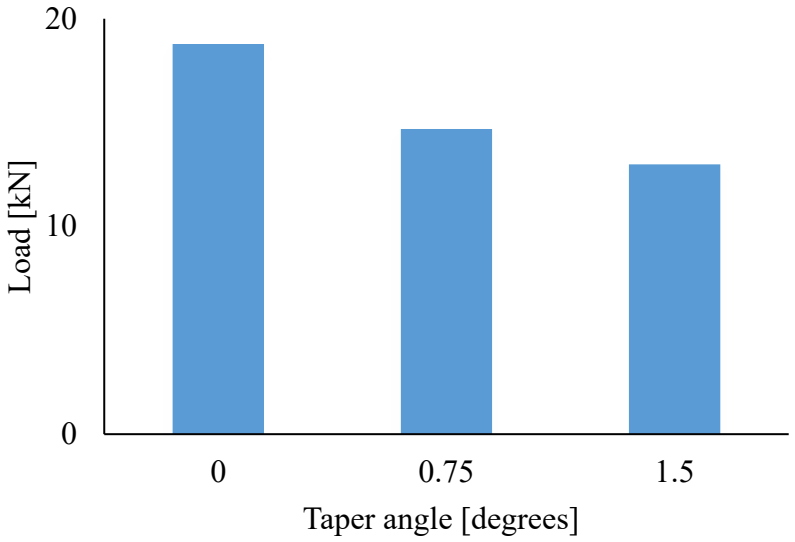

Figure 7.7: Failure load comparison for S, T1, and T2 walls at the end of installation

7.3.2 Failure mechanisms

The failure mechanisms of the straight wall (S), moderately tapered wall (T1), and sharply tapered wall (T2) were analyzed to evaluate the effect of taper geometry on failure patterns. The failure mechanisms exhibited a deep failure mode for all models, with slip lines concentrated near the wall base extending into the surrounding soil (Figure 7.8). The results consider an upper-bound solution with a kinematic mechanism.

For the straight model (S), the slip lines were localized directly below the base and extended vertically downward. This failure mechanism resulted in limited mobilization of the surrounding soil, with the load primarily transmitted by end-bearing at the wall base. The moderately tapered model (T1) shows a more distributed failure pattern. The slip lines originated from the base and extended outward along the taper region. This mechanism increased the contribution of shaft friction to the overall load-bearing capacity.

The sharply tapered model (T2) showed a similar deep failure mode, with slip lines concentrated closer to the pile tip and a reduced outward spread. The pronounced taper angle increased stress concentrations at the base and the shaft. However, the smaller base area had a lower bearing capacity than the T1 wall.

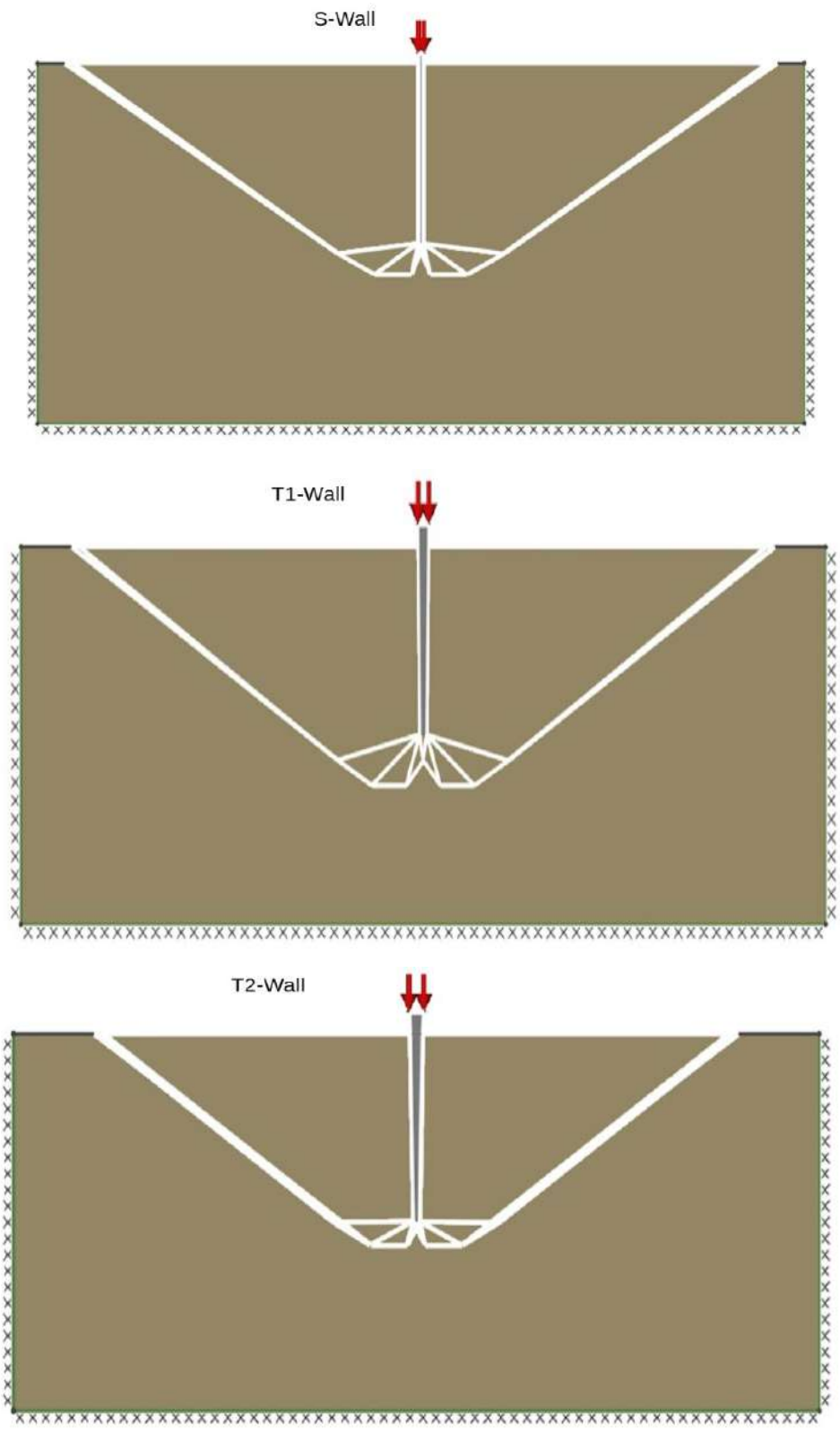

Figure 7.8: Failure mechanisms of the straight (S), moderately tapered (T1), and sharply tapered (T2) walls

7.4 Comparative analysis

7.4.1 Comparison of bearing capacity

The maximum load capacity from numerical analyses was compared with the centrifuge test result obtained at the end of monotonic penetration. Figure 7.9 shows a summary of the lower bound (LB) and upper bound (UB) solutions obtained from the FEM analysis (both MC and HMC models), Limit Analysis (LA), and centrifuge experimental results.

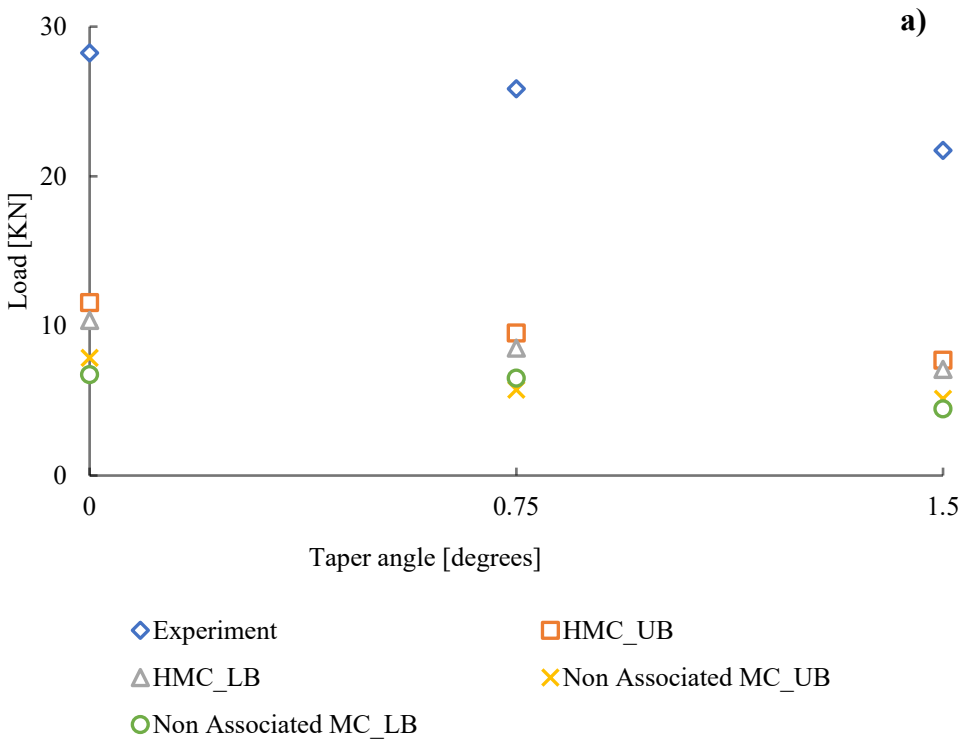

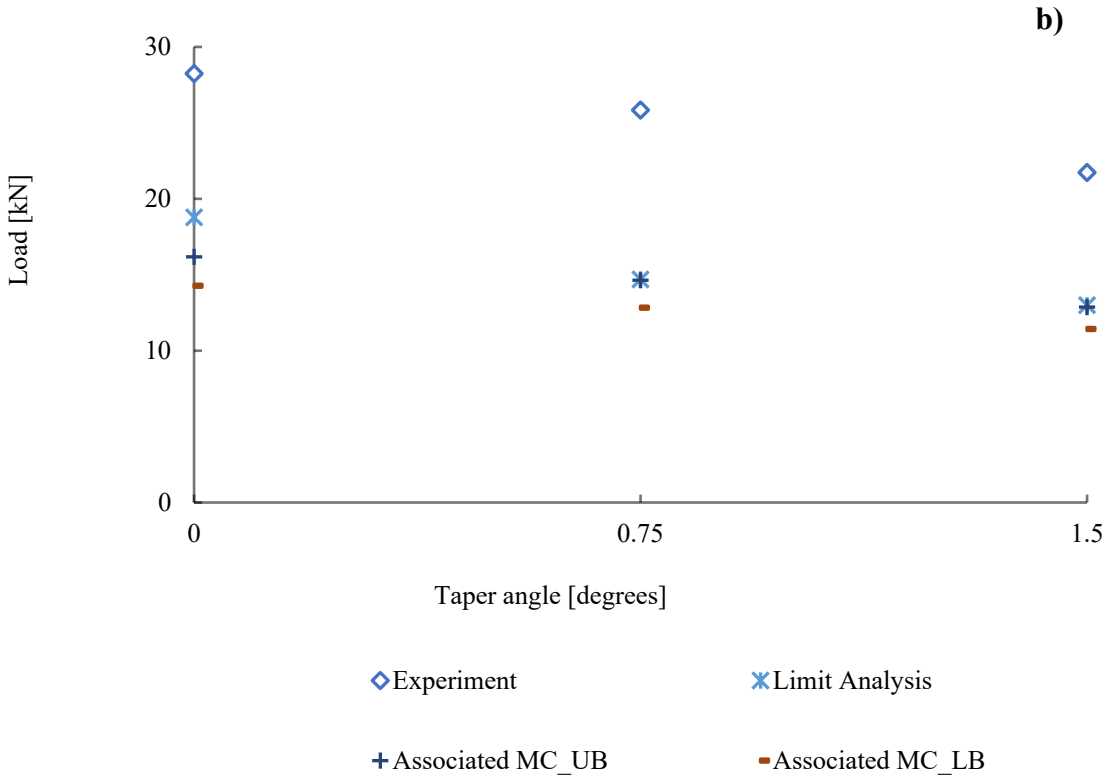

Figure 7.9: Comparison of total loads from numerical and experimental analysis (model scale) for a) non-associated flow rule b) associated flow rule

The LA results predicted higher load values than FEM models. However, the highest LA prediction fells below the experimental values, which shows the influence of installation effects. The MC-associated flow rule provided the upper bound for load predictions, showing higher values than MC non-associated and HMC models. Quite similar values of upper-bound solutions for the Mohr-Coulomb model with FEM and LA are obtained. FEM provides detailed predictions of failure load and deformation mechanisms, while LA focuses on failure mechanisms and collapse loads.

7.4.2 Estimation of installation effect

To further investigate the impact of installation, relative installation effects were calculated by comparing experimental ultimate loads with numerical results, as shown in Equation (7.1)

$$\text{Relative Installation Effect (\%)} = \frac{Experimental\ value - Numerical\ solution}{Experimental\ value}\ x\ 100 \quad (7.1)$$

$$Numerical\ solution = \frac{Upper\ bound\ value + Lower\ bound\ value}{2} \quad (7.2)$$

Figure 7.10 illustrates the relative installation effects of walls with their respective taper angles. The results indicate that the relative installation effects vary significantly depending on the analysis method and taper angle. The MC-non-associated model consistently predicts the highest relative installation effects, close to 74–76% for all taper angles. The Hardening Mohr-Coulomb (HMC) model also yields high estimates, ranging from 66% for the straight pile to around 72% for the tapered piles. These are followed closely by the MC-associated model, which gives moderate installation effects between 46–48%.

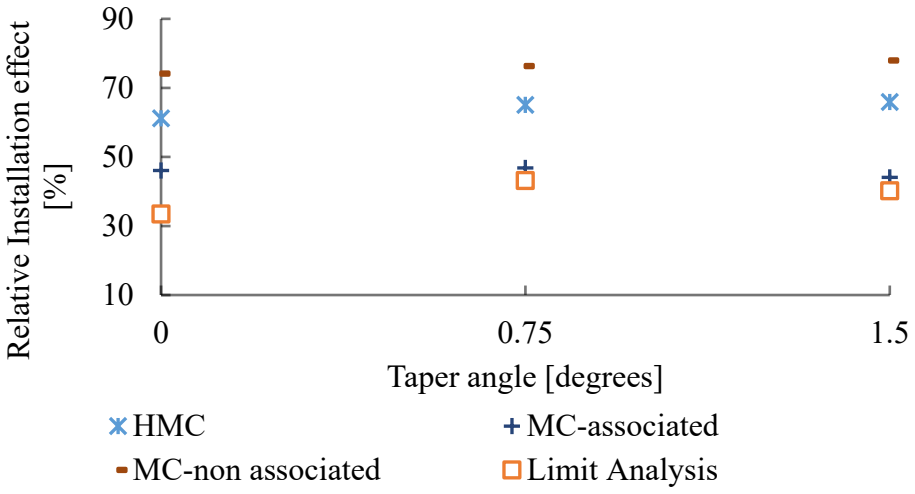

Figure 7.10: Relative installation effects (%) as a function of taper angle

In contrast, the limit analysis method provides the lowest relative installation effects, ranging from about 32% for the straight pile to 42% for the tapered pile. The relative installation effect tends to increase with taper angle. These variations emphasize that taper geometry and the choice of analysis method significantly influence the estimated installation effects on load-bearing performance. This finding is consistent with previous studies, such as (Broere and Van Tol, 2006; Phuong et al., 2016), which reported notable differences in numerically predicted load capacities when installation effects are omitted.

7.5 Summary

Limit Analysis (LA) and FEM using the Mohr-Coulomb (MC) model with associated flow rule provided comparable failure load predictions but underestimated experimental values. Finite Element Method (FEM) analyses, using both Mohr-Coulomb (MC) and Hardening Mohr-Coulomb (HMC) models predicted failure load. At the same time, LA provided valuable insights into failure mechanisms and collapse loads of walls.

The HMC model showed the best performance to simulate bored pile behavior among all numerical approaches. This is likely due to its ability to represent nonlinear stress-strain behavior, stiffness degradation, and density-dependent strength in the sand, making it more suitable for simulating pile-soil interaction under varying stress paths. The relative installation effect estimated using the HMC model was approximately 65.5% for the straight pile (0° taper), 68.5% for the 0.75° tapered pile, and 69.5% for the 1.5° tapered pile, showing a slight increase with taper angle. These values are higher than those obtained from the Limit Analysis and MC-associated models, but they reflect the model's sensitivity to stress path and soil densification during pile installation.

The result shows the significant impact of taper geometry. The difference between experimental values and numerical predictions are primarily attributed to installation-induced effects, such as soil densification, lateral stress increase, and stress redistribution, which were not considered in numerical analyses. While these effects were approximated through constitutive modeling in the HMC formulation, complementary studies using the Discrete Element Method (Ezzeddine, 2024) explicitly captured these mechanisms at the grain scale, including contact force evolution, local friction mobilization, and porosity changes during pile jacking.

CHAPTER EIGHT

8. Conclusion and recommendations

8.1 Conclusions

The study aimed to investigate the behavior of tapered piles during installation and loading in the sand, focusing on stress redistribution, soil deformation, and load transfer mechanisms under plane-strain conditions. The following sections summarize the key findings of this study.

Stress mobilization in the soil mass and along the wall interface

The installation of model walls results in a significant increase in horizontal stress within the soil mass and a change in normal stress at the wall surface. This stress mobilization depends on the model wall shape and penetration depth. Maximum horizontal stress in the soil mass typically occurs just before the wall base reaches each sensor level. Once the model wall passes the sensor level, the stress decreases with depth and stabilizes. However, in the case of tapered walls, a significant re-mobilization of stress is observed after the wall passes the sensor level, particularly for models with higher taper angles. The maximum horizontal stress at the wall is higher at the middle depth of the wall than near the base of the wall. Additionally, horizontal stress is higher near the wall and diminishes with increasing distance from the wall face, reflecting the localized nature of stress transfer during installation.

Normal contact stress measurements along the wall surface show that tapered walls mobilize higher normal stress than straight walls. A similar trend of stress mobilization is also observed during static loading. Tapered walls need lower installation effort than standard-shaped one. However, the tapered walls in dense sand exhibit lower bearing capacity (compression mode) in comparison to the standard pile.

Larger normal stress induced at the pile surface during monotonic penetration of the tapered wall results in higher shaft friction, but this does not balance the reduced wall base capacity due to the smaller breadth of the tapered wall base. Consequently, it results in slightly lower overall bearing capacity (10% lower for T1 wall and 20% lower for T2 pile) of tapered walls in dense sand.

The estimated lateral stress coefficient K increased significantly in tapered walls. Moreover, the taper coefficient K_t, which quantifies the influence of geometry on shaft friction, increases with taper angle. Both K and K_t show peak values at mid-depth and lower values near the top and bottom of the wall. The estimated shaft friction for the tapered wall is more than two times higher than for standard piles. While higher shaft friction is observed for tapered piles, their smaller base area results in lower total compression force in comparison with the standard pile. The proper evaluation of installation effects needs rigorous physical modelling of the whole process of wall insertion.

Soil displacement and strain field

PIV analysis of displacement and strain fields during wall installation reveals distinct patterns of soil response for different wall types and penetration depths. The soil zone affected by the installation is larger for tapered walls than for straight walls. Near the soil surface, horizontal displacements are greater for tapered walls but diminish more significantly near the wall tip than in the straight model.

Vertical displacement patterns show upward soil movement near the surface and downward movement near the wall base for all wall types, with the largest vertical displacements occurring near the base of the straight wall (S-wall). Analysis of soil particle trajectories indicates that the maximum downward movement of soil elements adjacent to the wall occurs when the model base reaches the corresponding sensor depth.

Volumetric strains show that installation of tapered walls densifies the nearby soil in approximately 1~2B zone (where B = wall breadth), and slightly loosens up the soil in the range of 4~8B from

the model wall. However, the range of the loosened-up zone (dilation zone) in the case of tapered walls is much smaller than for the straight one. This suggests better soil improvement around tapered walls than standard ones.

Insights from numerical analysis

Numerical analysis of wish-in-place walls using both Finite Element Method (FEM) and Limit Analysis offered additional insights into the load-bearing capacity and failure mechanisms of tapered walls. It is observed that the taper angle has a significant influence on the load-settlement behavior and failure modes of the walls. The significant difference is observed when compared with experimental values. These differences are primarily attributed to the absence of installation-induced effects in the numerical models. Moreover, the magnitude of the difference increases with larger taper angles, emphasizing the importance of accounting for installation effects in numerical simulations.

In summary, the combined results from stress measurements, displacement, strain field analyses, and numerical simulations show that the tapered pile has distinct behavior from the straight pile during installation and loading. These effects are more pronounced in the case of tapered walls due to their geometry, which induces greater soil disturbance, enhanced stress mobilization, and localized densification. Tapered walls generate larger contact stresses, influence a broader soil zone, and exhibit distinct displacement and strain patterns compared to straight walls. Numerical models that exclude installation effects underestimate the load-bearing capacity of tapered walls, especially at higher taper angles. Overall, the study highlights the importance of accounting for installation-induced effects when evaluating the performance of tapered piles. The analysis was performed for walls in plane strain conditions. These conclusions can also be used to describe the behavior of tapered piles qualitatively.

8.2 Recommendations for further study

The following recommendations are proposed for future research.

1. The piles studied had a relatively low slenderness ratio (L/D = 14), which limited the contribution of shaft resistance to load-bearing capacity. The application of longer piles with higher surface roughness could substantially increase the contribution of shaft friction to the overall bearing capacity of the models. As a result, the bearing capacity of tapered piles with a rough surface in dense sand would be higher than for the straight ones. Further analysis is necessary to confirm this hypothesis.
2. The numerical analyses in this study were based on wish-in-place conditions and did not simulate the installation process, leading to discrepancies with experimental results. Future research should incorporate installation-induced effects using advanced numerical methods such as large-deformation finite element analysis or meshless approaches.
3. Further investigation is recommended to investigate the effect of varying boundary conditions, different embedment depths, soil density, and layered soil profiles on the performance of tapered piles.

Bibliography

Al Heib, M., Emeriault, F., & Nghiem, H.-L. (2020). On the use of 1g physical models for ground movements and soil-structure interaction problems. *Journal of Rock Mechanics and Geotechnical Engineering*, *12*(1), 197–211. https://doi.org/10.1016/j.jrmge.2019.07.006

Alhassani, A. (2021). Analysis of Under-reamed Piles Subjected to Different Types of Load in Clayey Soil. *International Journal of Engineering*, *34*, 1940–1948. https://doi.org/10.5829/ije.2021.34.08b.15

Allard, M.-A. (1990). *Soil stress field around driven piles* [PhD thesis]. California Institute of Technology.

Andria-Ntoanina, I., Canou, J., & Dupla, J. (2010). Caractérisation mécanique du sable de Fontainebleau NE34 à l'appareil triaxial sous cisaillement monotone. *Laboratoire Navier–Géotechnique. CERMES, ENPC/LCPC*.

Anusic, I., Lehane, B. M., Eiksund, G. R., & Liingaard, M. A. (2019a). Evaluation of installation effects on set-up of field displacement piles in sand. *Canadian Geotechnical Journal*, *56*(4), 461–472. https://doi.org/10.1139/cgj-2017-0730

Anusic, I., Lehane, B. M., Eiksund, G. R., & Liingaard, M. A. (2019b). Influence of installation method on static lateral response of displacement piles in sand. *Géotechnique Letters*, *9*(3), 193–197. https://doi.org/10.1680/jgele.18.00191

Aoki, N., & Velloso, D. A. (1975). An approximate method to estimate the bearing capacity of piles. *Proc., 5th Pan-American Conf. of Soil Mechanics and Foundation Engineering*, *1*, 367–376.

API, R. (2014). 2GEO, Geotechnical and Foundation Design Considerations. 2011. *Washington, DC, USA: API*.

Arshad, M. I., Tehrani, F. S., Prezzi, M., & Salgado, R. (2014). Experimental study of cone penetration in silica sand using digital image correlation. *Géotechnique*, *64*(7), 551–569. https://doi.org/10.1680/geot.13.P.179

Balachowski, L. (2006). Penetration Resistance of Lubiatowo Sand in Calibration Chamber Tests. *Archives of Hydro-Engineering and Environmental Mechanics*, *53*, 311–329.

Bałachowski, L. (2006). Scale effect in shaft friction from the direct shear interface tests. *Archives of Civil and Mechanical Engineering*, *6*(3), 13–28. https://doi.org/10.1016/S1644-9665(12)60238-6

Bałachowski, L. (2007). Size Effect in Centrifuge Cone Penetration Tests. *Archives of Hydro-Engineering and Environmental Mechanics*, *54*(3), 161–181.

Balachowski, L. (2008). *Physical modeling in sands in a wide range of stress level: Application to the calibration of CPTU and DMT tests.*

Bałachowski, L., & Kurek, N. (2008). Influence of boundary conditions in calibration chamber. *Archives of Civil Engineering*, *Vol. 54*(nr 4), 653–668.

Bekki, H., Tali, B., Canou, J., & Dupla, J.-C. (2024). Effect of cyclic loading at a large number of cycles on the bearing capacity of piles in sand. *Acta Geotechnica*, *19*(2), 591–604. https://doi.org/10.1007/s11440-023-02093-y

Beroya-Eitner, M. A., Machaček, J., Viggiani, G., Dastider, A. G., Thorel, L., Korre, E., Agalianos, A., Jafarian, Y., Zwanenburg, C., Lenart, S., Wang, H., Zachert, H., & Stanier, S. (2022). *GEOLAB Material Properties Database* (Version 1.0) [Dataset]. Zenodo. https://doi.org/10.5281/ZENODO.7462287

Bhandari, T., Deb, D., & Sai Reddy, C. (2023). *Global Unstructured Digital Image Correlation for determining strains around circular opening*.

Black, J. A. (2012). *CENTRIFUGE MODELLING OF PRESS-IN PILING INSTALLATION*. Proceedings of the International Press-in Association 4th Workshop. Singapore.

Blanc, M., & Thorel, L. (2016). Effects of cyclic axial loading sequences on piles in sand. *Géotechnique Letters*, *6*(2), 163–167. https://doi.org/10.1680/jgele.15.00155

Boccalini, F., Chen, Z., Omidvar, M., & Iskander, M. (2015). A Study of Plane Strain Pile Jacking and Driving in Granular Media. *IFCEE 2015*, 738–747. https://doi.org/10.1061/9780784479087.066

Bolton, M., & Lau, C. (1988). Scale effects arising from particle size. *Centrifuge 88: Proceedings of the International Conference on Geotechnical Centrifuge Modelling*, *1*, 127–131.

Boulon, M. (1989). Basic features of soil structure interface behaviour. *Computers and Geotechnics*, *7*(1–2), 115–131. https://doi.org/10.1016/0266-352X(89)90010-4

Bowles, J. E., & Guo, Y. (1996). *Foundation analysis and design* (Vol. 5). McGraw-hill New York.

Broere, W., & Van Tol, A. F. (2006). Modelling the bearing capacity of displacement piles in sand. *Proceedings of the Institution of Civil Engineers - Geotechnical Engineering*, *159*(3), 195–206. https://doi.org/10.1680/geng.2006.159.3.195

Burali d'Arezzo, F., Haigh, S., Talesnick, M., & Ishihara, Y. (2015). Measuring horizontal stresses during jacked pile installation. *Proceedings of the Institution of Civil Engineers - Geotechnical Engineering*, *168*(4), 306–318. https://doi.org/10.1680/geng.14.00069

Cao, Z., Qiang Kong, G.-, Hang, Z., & Z.-Z, G. (2015). *Model test on installation effect of tapered piles in transparent soils*. *05*. https://doi.org/10.16285/j.rsm.2015.05.018

Cerfontaine, B., Brown, M., Ciantia, M., Huisman, M., & Ottolini, M. (2023). Silent piling for offshore jacket foundations in sand: DEM and centrifuge modelling. *Symposium on Energy Geotechnics 2023*, 1–2. https://doi.org/10.59490/seg.2023.614

Chen, Z. (Chris), Li, K., Omidvar, M., & Iskander, M. (2017). Guidelines for DIC in geotechnical engineering research. *International Journal of Physical Modelling in Geotechnics*, *17*(1), 3–22. https://doi.org/10.1680/jphmg.15.00040

Choi, Y. S., Basu, D., Prezzi, M., & Salgado, R. (2015). Study on laterally loaded piles with rectangular and circular cross sections. *Geomechanics and Geoengineering*, *10*(2), 139–152. https://doi.org/10.1080/17486025.2014.902119

Christin, J., Le Kouby, A., Reiffsteck, P., & Rocher-Lacoste, F. (2013). *Timber pile load test instrumented with removable extensometers*. *1716*, 8.

Ciantia, M. O., O'Sullivan, C., & Jardine, R. J. (2019). Pile penetration in crushable soils: Insights from micromechanical modelling. *Proceedings of the XVII European Conference on Soil Mechanics and Geotechnical Engineering*, *Geotechnical Engineering, foundation of the future*, 5247–5266. https://doi.org/10.32075/17ECSMGE-2019-1111

Coduto, D. P., Kitch, W. A., & Yeung, M. R. (2016). *Geotechnical Engineering: Principles and Practices*. Pearson.

Coyle, H. M., & Castello, R. R. (1981). New Design Correlations for Piles in Sand. *Journal of the Geotechnical Engineering Division*, *107*(7), 965–986. https://doi.org/10.1061/AJGEB6.0001172

Craig, W. H. (1985). INSTALLATION STUDIES FOR MODEL PILES. *Publication of: Balkema (AA)*. https://trid.trb.org/View/278771

Craig, W. H. (1994). Geotechnical centrifuges: Past, present and future. In *Geotechnical Centrifuge Technology*. CRC Press.

Das, B. M. (2007). *Principles of Foundation Engineering* (6th ed.). Thomson.

Das, B. M., & Sivakugan, N. (2019). *Principles of Foundation Engineering* (9th, SI Edition ed.). Cengage Learning. https://pdfcoffee.com/principles-of-foundation-engineering-7th-edition-si-units-ed-pdf-free.html

Doreau-Malioche, J., Galvis-Castro, A., Tovar-Valencia, R., Viggiani, G., Combe, G., Prezzi, M., & Salgado, R. (2019). Characterising processes at sand-pile interface using digital image analysis and X-ray CT. *Géotechnique Letters*, *9*(4), 254–262. https://doi.org/10.1680/jgele.18.00232

El Haffar, I., Blanc, M., & Thorel, L. (2017). Impact of pile installation method on the axial capacity in sand. *Géotechnique Letters*, *7*(3), 260–265. https://doi.org/10.1680/jgele.17.00036

El Naggar, M. H., & Wei, J. Q. (1999). Axial capacity of tapered piles established from model tests. *Canadian Geotechnical Journal*, *36*(6), 1185–1194. https://doi.org/10.1139/t99-076

Ezzeddine, A. (2024). *Behavior of granular material under cyclic stress* [PhD thesis]. Nantes Université.

Fahmy, A., & El Naggar, M. H. (2017). Axial Performance of Helical Tapered Piles in Sand. *Geotechnical and Geological Engineering*, *35*(4), 1549–1576. https://doi.org/10.1007/s10706-017-0192-1

Fan, S., Bienen, B., & Randolph, M. F. (2021). Centrifuge study on effect of installation method on lateral response of monopiles in sand. *International Journal of Physical Modelling in Geotechnics*, *21*(1), 40–52. https://doi.org/10.1680/jphmg.19.00013

Fang, K., Miao, M., Tang, H., Jia, S., Dong, A., An, P., & Zhang, B. (2023). Insights into the deformation and failure characteristic of a slope due to excavation through multi-field monitoring: A model test. *Acta Geotechnica*, *18*(2), 1001–1024. https://doi.org/10.1007/s11440-022-01627-0

Fioravante, V. (2002). On the Shaft Friction Modelling of Non-Displacement Piles in Sand. *Soils and Foundations*, *42*(2), 23–33. https://doi.org/10.3208/sandf.42.2_23

Foray, P. (1991). Scale and boundary effects on calibration chamber pile tests. *Proceedings of the First International Symposium on Calibration Chamber Testing*, 147–160.

Foray, P., Balachowski, L., & Colliat, J.-L. (1998). Bearing capacity of model piles driven into dense overconsolidated sands. *Canadian Geotechnical Journal*, *35*(2), 374–385. https://doi.org/10.1139/t97-082

Foray, P., Balachowski, L., & Rault, G. (1998). Scale effect in shaft friction due to the localisation of deformations. *International Conference Centrifuge 98*, 211–216.

Fu, S., Yang, Z. X., Jardine, R. J., & Guo, N. (2023). Large-Deformation Finite-Element Simulation of Deformation and Strain Fields Resulting from Closed-End Displacement Pile Installation in Sand. *Journal of Geotechnical and Geoenvironmental Engineering*, *149*(6), 04023038. https://doi.org/10.1061/JGGEFK.GTENG-10480

Garnier, J., Gaudin, C., Springman, S. M., Culligan, P. J., Goodings, D., Konig, D., Kutter, B., Phillips, R., Randolph, M. F., & Thorel, L. (2007). Catalogue of scaling laws and similitude questions in geotechnical centrifuge modelling. *International Journal of Physical Modelling in Geotechnics*, *7*(3), 01–23. https://doi.org/10.1680/ijpmg.2007.070301

Gavin, K. G., & Lehane, B. M. (2003). The shaft capacity of pipe piles in sand. *Canadian Geotechnical Journal*, *40*(1), 36–45. https://doi.org/10.1139/t02-093

Gavin, K., & Lehane, B. (2007). Base load – displacement response of piles in sand. *Canadian Geotechnical Journal*, *44*(9), 1053–1063. https://doi.org/10.1139/T07-048

Geolab. (2021). *Geolab – Science for enhancing Europe's Critical Infrastructure*. https://project-geolab.eu/

Gers-CG. (2023). *Centrif-UGE*. https://cg.univ-gustave-eiffel.fr/en/translate-to-english-equipements/translate-to-english-centrif-uge

Gui, M., Bolton, M., Garnier, J., Corte, J., Bagge, G., Laue, J., & Renzi, R. (1998). Guidelines for cone penetration tests in sand, in Centrifuge. *International Conference Centrifuge 98*, 211–216.

Gui, M.-W., & Muhunthan, B. (2006). Bearing capacity of foundations on sand using the method of slip line. *Journal of Marine Science and Technology*, *14*, 1–14. https://doi.org/10.51400/2709-6998.2074

Haque, Md. N., Abu-Farsakh, M. Y., & Tsai, C. (2016). Field Investigation to Evaluate the Effects of Pile Installation Sequence on Pile Setup Behavior for Instrumented Test Piles. *Geotechnical Testing Journal*, *39*(5), 20140259. https://doi.org/10.1520/GTJ20140259

Henke, S., & Grabe, J. (2008). Numerical investigation of soil plugging inside open-ended piles with respect to the installation method. *Acta Geotechnica*, *3*(3), 215–223. https://doi.org/10.1007/s11440-008-0079-7

Herrera, J. E. O. (2021). *Ground Movements and Vibrations Caused by Impact Pile Driving of Prestressed Concrete Piles in Central Florida*. https://doi.org/10.13140/RG.2.2.35008.05122

Horvath, J. S., & Trochalides, T. (2004). A Half Century of Tapered-Pile Usage at the John F. Kennedy International Airport. *International Conference on Case Histories in Geotechnical Engineering*. Fifth International Conference on Case Histories in Geotechnical Engineering, New York.

Horvath, J. S., Trochalides, T., Burns, A., & Merjan, S. (2004). A New Type of Tapered Steel Pipe Pile for Transportation Applications. *Geotechnical Engineering for Transportation Projects*, 1299–1308. https://doi.org/10.1061/40744(154)119

Hyodo, M., Wu, Y., Aramaki, N., & Nakata, Y. (2017). Undrained monotonic and cyclic shear response and particle crushing of silica sand at low and high pressures. *Canadian Geotechnical Journal*, *54*(2), 207–218. https://doi.org/10.1139/cgj-2016-0212

Ibrahim, A., & Karkush, M. (2023). The Efficiency of Belled Piles in Multi-Layers Soils Subjected to Axial Compression and Pullout Loads: Review. *Journal of Engineering*, *29*, 166–183. https://doi.org/10.31026/j.eng.2023.09.12

Ismael, N. F. (2010). Behavior of Step Tapered Bored Piles in Sand under Static Lateral Loading. *Journal of Geotechnical and Geoenvironmental Engineering*, *136*(5), 669–676. https://doi.org/10.1061/(ASCE)GT.1943-5606.0000265

Jardine, R. J., Zhu, B. T., Foray, P., & Yang, Z. X. (2013a). Interpretation of stress measurements made around closed-ended displacement piles in sand. *Géotechnique*, *63*(8), 613–627. https://doi.org/10.1680/geot.9.P.138

Jardine, R. J., Zhu, B. T., Foray, P., & Yang, Z. X. (2013b). Measurement of stresses around closed-ended displacement piles in sand. *Géotechnique*, *63*(1), 1–17. https://doi.org/10.1680/geot.9.P.137

Kabeta, W. F. (2023). Effects of full displacement pile installation on the stress and deformation state of surrounding soil: Review. *Archives of Civil Engineering*. https://doi.org/10.24425/ace.2022.143048

Khan, M. K., El Naggar, M. H., & Elkasabgy, M. (2008). Compression testing and analysis of drilled concrete tapered piles in cohesive-frictional soil. *Canadian Geotechnical Journal*, *45*(3), 377–392. https://doi.org/10.1139/T07-107

Kido, R., Sawamura, Y., Kimura, K., & Kimura, M. (2021). Investigation of soil deformation characteristics during pullout of a ribbed reinforcement using X-ray micro CT. *Soils and Foundations*, *61*(3), 642–657. https://doi.org/10.1016/j.sandf.2021.01.013

Kido, R., Suezawa, R., Sawamura, Y., & Kimura, M. (2022). Experimental investigation of bearing mechanism of closed- and open-ended piles supported by thin bearing layer using X-ray micro CT. *Soils and Foundations*, *62*(4), 101179. https://doi.org/10.1016/j.sandf.2022.101179

King, L., Bouazza, A., Maksimenko, A., Gates, W. P., & Dubsky, S. (2019). Measurement of three-dimensional displacement field in piled embankments using synchrotron X-ray tomography. *Canadian Geotechnical Journal*, *56*(6), 885–892. https://doi.org/10.1139/cgj-2018-0159

Klinkvort, R. T., Hededal, O., & Springman, S. M. (2013). Scaling issues in centrifuge modelling of monopiles. *International Journal of Physical Modelling in Geotechnics*, *13*(2), 38–49. https://doi.org/10.1680/ijpmg.12.00010

Kluger, M. O., Kreiter, S., Stähler, F. T., Goodarzi, M., Stanski, T., & Mörz, T. (2021). Cone penetration tests in dry and saturated Ticino sand. *Bulletin of Engineering Geology and the Environment*, *80*(5), 4079–4088. https://doi.org/10.1007/s10064-021-02156-y

Kodikara, J. K., & Moore, I. D. (1993). Axial Response of Tapered Piles in Cohesive Frictional Ground. *Journal of Geotechnical Engineering*, *119*(4), 675–693. https://doi.org/10.1061/(ASCE)0733-9410(1993)119:4(675)

Kodsy, A., & Iskander, M. (2022). Insights into Plugging of Pipe Piles Based on Pile Dimensions. *Applied Sciences*, *12*(5), 2711. https://doi.org/10.3390/app12052711

Krasinski, A. (2015). The Analysis of Soil Resistance During Screw Displacement Pile Installation. *Studia Geotechnica et Mechanica*, *36*(3), 49–56. https://doi.org/10.2478/sgem-2014-0026

Lee, & Do. (2021). Effects of the Installation Method, Loading Condition, and Failure Mechanism on the Behavior of Suction Piles under Monotonic Horizontal Loading. *Journal of Marine Science and Engineering*, *9*(12), 1333. https://doi.org/10.3390/jmse9121333

Lee, J., Paik, K., Kim, D., & Hwang, S. (2009). Estimation of Axial Load Capacity for Bored Tapered Piles Using CPT Results in Sand. *Journal of Geotechnical and Geoenvironmental Engineering*, *135*(9), 1285–1294. https://doi.org/10.1061/(ASCE)GT.1943-5606.0000036

Lee, L. M., Kassim, A., & Gofar, N. (2011). Performances of two instrumented laboratory models for the study of rainfall infiltration into unsaturated soils. *Engineering Geology*, *117*(1–2), 78–89. https://doi.org/10.1016/j.enggeo.2010.10.007

Lehane, B. M., & White, D. J. (2005). Lateral stress changes and shaft friction for model displacement piles in sand. *Canadian Geotechnical Journal*, *42*(4), 1039–1052. https://doi.org/10.1139/t05-023

Leśniewska, D., Pietrzak, M., & Tejchman-Konarzewski, A. (2014). *Photo-elastic and DIC techniques to study development of dilatant and compaction shear bands within granular materials*. MOST Wiedzy - portal z wiedzą dla Ciebie. https://mostwiedzy.pl/pl/publication/photo-elastic-and-dic-techniques-to-study-development-of-dilatant-and-compaction-shear-bands-within-,130099-1

Li, Chen, & Ding. (2022). Consolidation of soil induced by pile installation considering disturbance effect. *Revista Internacional de Métodos Numéricos Para Cálculo y Diseño En Ingeniería*, *38*(1). https://doi.org/10.23967/j.rimni.2022.03.008

Li, Z.-S., Blanc, M., & Thorel, L. (2022). Dataset for centrifuge modelling of laterally monotonic loaded monopiles in saturated dense sand. *Data in Brief*, *42*, 108312. https://doi.org/10.1016/j.dib.2022.108312

Liu, C., Tang, X., Wei, H., Wang, P., & Zhao, H. (2020). Model Tests of Jacked-Pile Penetration into Sand Using Transparent Soil and Incremental Particle Image Velocimetry. *KSCE Journal of Civil Engineering*, *24*(4), 1128–1145. https://doi.org/10.1007/s12205-020-1643-4

Liu, J., Guo, Z., & Han, B. (2019). Load Transfer of Offshore Open-Ended Pipe Piles Considering the Effect of Soil Plugging. *Journal of Marine Science and Engineering*, *7*(9), 313. https://doi.org/10.3390/jmse7090313

Liu, W. (2010). *Axisymmetric centrifuge modelling of deep penetration in sand* [PhD thesis]. University of Cambridge.

Loukidis, D., & Salgado, R. (2008). Analysis of the shaft resistance of non-displacement piles in sand. *Géotechnique*, *58*(4), 283–296. https://doi.org/10.1680/geot.2008.58.4.283

Lu, Y., Liu, H., Zheng, C., & Ding, X. (2017). Experimental Study on the Behavior of X-Section Pile Subjected to Cyclic Axial Load in Sand. *Shock and Vibration*, *2017*, 1–9. https://doi.org/10.1155/2017/2431813

Lunne, T. (1991). *Practical use of CPT correlations in sand based on calibration chamber test*.

Lunne, T., Robertson, P. K., & Powell, J. M. M. (1997). *Cone penetration testing in geotechnical practice*. Taylor & Francis Group.

Manandhar, S., & Yasufuku, N. (2012). Analytical Model for the End-Bearing Capacity of Tapered Piles Using Cavity Expansion Theory. *Advances in Civil Engineering*, *2012*, 1–9. https://doi.org/10.1155/2012/749540

Meng, Z., Chen, J.-J., Zhang, L., Wang, J.-H., & Yao, J.-M. (2015). Field Tests to Investigate the Installation Effects of Drilled Displacement Piles with Screw-Shaped Shaft in Clay. *Journal of Geotechnical and Geoenvironmental Engineering*, *141*(12), 06015010. https://doi.org/10.1061/(ASCE)GT.1943-5606.0001371

Meyerhof, G. G. (1976). Bearing Capacity and Settlement of Pile Foundations. *Journal of the Geotechnical Engineering Division*, *102*(3), 197–228. https://doi.org/10.1061/AJGEB6.0000243

Naggar, M. H. E., & Sakr, M. (2000). Evaluation of axial performance of tapered piles from centrifuge tests. *Canadian Geotechnical Journal*, *37*(6), 1295–1308. https://doi.org/10.1139/t00-049

Naggar, M. H., & Sakr, M. (2002). Cyclic response of axially loaded tapered piles. *International Journal of Physical Modelling in Geotechnics*, *2*(4), 01–12. https://doi.org/10.1680/ijpmg.2002.020401

Nasrollahzadeh, E., & Hataf, N. (2022). Experimental and numerical study on the bearing capacity of single and groups of tapered and cylindrical piles in sand. *International Journal of Geotechnical Engineering*, *16*(4), 426–437. https://doi.org/10.1080/19386362.2019.1651042

Neely, W. J. (1990). Bearing Capacity of Expanded-Base Piles in Sand. *Journal of Geotechnical Engineering*, *116*(1), 73–87. https://doi.org/10.1061/(ASCE)0733-9410(1990)116:1(73)

Nguyen, C. D., Benahmed, N., Andò, E., Sibille, L., & Philippe, P. (2019). Experimental investigation of microstructural changes in soils eroded by suffusion using X-ray tomography. *Acta Geotechnica*, *14*(3), 749–765. https://doi.org/10.1007/s11440-019-00787-w

OPTUM Engineering. (2020). *OPTUM G2 User Manual*. https://www.optumengineering.com/

Otani, J., Mukunoki, T., & Obara, Y. (2000). Application of X-Ray CT Method for Characterization of Failure in Soils. *Soils and Foundations*, *40*(2), 111–118. https://doi.org/10.3208/sandf.40.2_111

Paik, K., Lee, J., & Kim, D. (2013). Calculation of the axial bearing capacity of tapered bored piles. *Proceedings of the Institution of Civil Engineers - Geotechnical Engineering*, *166*(5), 502–514. https://doi.org/10.1680/geng.10.00127

Paik, Lee, & Kim. (2007). Axial Behavior of Non-Displacement Tapered Piles in Sand. *Journal of the Korean Geotechnical Society*, *23*(8), 35–45. https://doi.org/10.7843/KGS.2007.23.8.35

Paik, & Salgado. (2004). Effect of Pile Installation Method on Pipe Pile Behavior in Sands. *Geotechnical Testing Journal*, *27*(1), 78–88. https://doi.org/10.1520/GTJ11268J

Paik, Salgado, Lee, & Kim. (2003). Behavior of Open- and Closed-Ended Piles Driven Into Sands. *Journal of Geotechnical and Geoenvironmental Engineering*, *129*(4), 296–306. https://doi.org/10.1061/(ASCE)1090-0241(2003)129:4(296)

Peiffer, H., Van Impe, W., Cortvrindt, G., & Bottiau, m. (1993). *Evaluation of the influence of pile execution parameters on the soil condition around the pile shaft of a PSC-pile* (Vol. 1, pp. 217–220). BAPII.

Perko, H. A. (2009). *Helical Piles: A Practical Guide to Design and Installation* (1st ed.). Wiley. https://doi.org/10.1002/9780470549063

Phuong, N. T. V., Tol, A. F. van, Elkadi, A. S. K., & Rohe, A. (2016). Numerical investigation of pile installation effects in sand using material point method. *Computers and Geotechnics*, *73*, 58–71. https://doi.org/10.1016/j.compgeo.2015.11.012

Poulos, H. G., & Mattes, N. S. (1969). The Behaviour Of Axially Loaded End-Bearing Piles. *Géotechnique*, *19*(2), 285–300. https://doi.org/10.1680/geot.1969.19.2.285

Raffel, M., Willert, C. E., Scarano, F., Kähler, C. J., Wereley, S. T., & Kompenhans, J. (2018). *Particle Image Velocimetry: A Practical Guide*. Springer International Publishing. https://doi.org/10.1007/978-3-319-68852-7

Randolph, M. F., Carter, J. P., & Wroth, C. P. (1979). Driven piles in clay—The effects of installation and subsequent consolidation. *Géotechnique*, *29*(4), 361–393. https://doi.org/10.1680/geot.1979.29.4.361

Robinsky, E. I., & Morrison, C. F. (1964). Sand Displacement and Compaction around Model Friction Piles. *Canadian Geotechnical Journal*, *1*(2), 81–93. https://doi.org/10.1139/t64-002

Robinsky, E. I., Sagar, W. L., & Morrison, C. F. (1964). Effect of Shape and Volume on the Capacity of Model Piles in Sand. *Canadian Geotechnical Journal*, *1*(4), 189–204. https://doi.org/10.1139/t64-015

Rockhill, D. J., Bolton, M. D., & White, D. (2003). Ground-borne vibrations due to press-in piling operations. *Proceedings of the International Conference Organised by British Geotechnical Association*, *1*, 743–756.

Rybnikov, A. M. (1990). Experimental investigations of bearing capacity of bored-cast-in-place tapered piles. *Soil Mechanics and Foundation Engineering*, *27*(2), 48–52. https://doi.org/10.1007/BF02306100

Sakr, M., & El Naggar, M. (2003). Centrifuge Modeling of Tapered Piles in Sand. *Geotechnical Testing Journal*, *26*(1), 22–35. https://doi.org/10.1520/GTJ11106J

Sakr, M., Naggar, M. H. E., & Nehdi, M. (2004). Load transfer of fibre-reinforced polymer (FRP) composite tapered piles in dense sand. *Canadian Geotechnical Journal*, *41*(1), 70–88. https://doi.org/10.1139/t03-067

Salah, S. S., Azzam ,Waseim Ragab, & and Nasr, A. M. (2025). Response of X shaped pile in clay soil subjected to torsional and inclined compression loads. *Water Science*, *39*(1), 58–72. https://doi.org/10.1080/23570008.2024.2439589

Samyukta, P., & Babu, kV. (2022). *A STUDY ON PERFORMANCE OF PILES BASED ON METHODS OF INSTALLATION*.

Schiavon, J. A., Tsuha, C. D. H. C., & Thorel, L. (2020). *Study on the installation effect of helical piles in very dense sand*. 4th European Conference on Physical Modelling in Geotechnics - ECPMG, Lulea / Sweden.

Schlager, T., & Moormann, C. (2022). Inflight installation of a jacked pile group for modelling installation effects. *ISSMGE*. https://doi.org/10.53243/ECPMG2024-90

Schofield, A. N. (1980). Cambridge Geotechnical Centrifuge Operations. *Géotechnique*, *30*(3), 227–268. https://doi.org/10.1680/geot.1980.30.3.227

Shabanpour, & Ghazavi. (2022). Centrifuge tests on axially loaded tapered piles with different cross-sections under compressive and tensile loading. *Canadian Geotechnical Journal*, *59*(7), 1205–1214. https://doi.org/10.1139/cgj-2020-0732

Shafaghat, A., & Khabbaz, H. (2022). Recent advances and past discoveries on tapered pile foundations: A review. *Geomechanics and Geoengineering*, *17*(2), 455–484. https://doi.org/10.1080/17486025.2020.1794057

Shi, B., Murakami, Y., Wu, Z., Chen, J., & Inyang, H. (1999). Monitoring of internal failure evolution in soils using computerization X-ray tomography. *Engineering Geology*, *54*(3–4), 321–328. https://doi.org/10.1016/S0013-7952(99)00080-0

Shublaq, E. W. (1992). Soil Disturbance Due to Installation of Model Piles and Pile Groups. *Soils and Foundations*, *32*(4), 17–26. https://doi.org/10.3208/sandf1972.32.4_17

Sokolov, N., Mikhailov, B., & Viktorova, S. (2021). Foundation with increased load bearing base capacity. *E3S Web of Conferences*, *274*, 03015. https://doi.org/10.1051/e3sconf/202127403015

Stanier, S. A., Blaber, J., Take, W. A., & White, D. J. (2016). Improved image-based deformation measurement for geotechnical applications. *Canadian Geotechnical Journal*, *53*(5), 727–739. https://doi.org/10.1139/cgj-2015-0253

Stuedlein, A. W., Gianella, T. N., & Canivan, G. (2016). Densification of Granular Soils Using Conventional and Drained Timber Displacement Piles. *Journal of Geotechnical and Geoenvironmental Engineering*, *142*(12), 04016075. https://doi.org/10.1061/(ASCE)GT.1943-5606.0001554

Suits, L. D., Sheahan, T. C., Paik, K., Lee, J., & Kim, D. (2011). Axial Response and Bearing Capacity of Tapered Piles in Sandy Soil. *Geotechnical Testing Journal*, *34*(2), 102761. https://doi.org/10.1520/GTJ102761

Suits, L., Sheahan, T., Sakr, M., & El Naggar, M. H. (2003). Centrifuge Modeling of Tapered Piles in Sand. *Geotechnical Testing Journal - GEOTECH TESTING J*, *26*. https://doi.org/10.1520/GTJ11106J

Takano, D., Lenoir, N., Otani, J., & Hall, S. A. (2015). Localised deformation in a wide-grained sand under triaxial compression revealed by X-ray tomography and digital image correlation. *Soils and Foundations*, *55*(4), 906–915. https://doi.org/10.1016/j.sandf.2015.06.020

Talesnick, M., & Omer, I. (2024). Measurement of stresses and strains around a pushed-in model pile or cone penetrometer. *International Journal of Physical Modelling in Geotechnics*, *24*(4), 161–171. https://doi.org/10.1680/jphmg.22.00056

Tavasoli, O., & Ghazavi, M. (2020). Effect of tapered and semi-tapered geometry on the offshore piles driving performance. *Ocean Engineering*, *201*, 107147. https://doi.org/10.1016/j.oceaneng.2020.107147

Tavenas, F. A. (1971). Load Tests Results on Friction Piles in Sand. *Canadian Geotechnical Journal*, *8*(1), 7–22. https://doi.org/10.1139/t71-002

Taylor, R. N. (1995). *Geotechnical Centrifuge Technology*.

Tehrani, F. S., Arshad, M. I., Prezzi, M., & Salgado, R. (2018). Physical Modeling of Cone Penetration in Layered Sand. *Journal of Geotechnical and Geoenvironmental Engineering*, *144*(1), 04017101. https://doi.org/10.1061/(ASCE)GT.1943-5606.0001809

Tovar-Valencia, R. D., Galvis-Castro, A., Salgado, R., & Prezzi, M. (2021). Effect of Base Geometry on the Resistance of Model Piles in Sand. *Journal of Geotechnical and Geoenvironmental Engineering*, *147*(3), 04020180. https://doi.org/10.1061/(ASCE)GT.1943-5606.0002472

Tovar-Valencia, R. D., Galvis-Castro, A., Salgado, R., Prezzi, M., & Fridman, D. (2023). Experimental measurement of particle crushing around model piles jacked in a calibration chamber. *Acta Geotechnica*, *18*(3), 1331–1351. https://doi.org/10.1007/s11440-022-01681-8

Tsai, C.-C., Lin, C.-Y., Dashti, S., & Kirkwood, P. (2021). Influence of centrifuge container boundaries and loading characteristics on evaluation of dynamic properties in dry sand. *Soil Dynamics and Earthquake Engineering*, *142*, 106567. https://doi.org/10.1016/j.soildyn.2020.106567

Tsuha, C. de H. C., Aoki, N., Rault, G., Thorel, L., & Garnier, J. (2010). Physical modelling of helical screw piles in sand. *Phys Model Geotech*, *1*, 2841–2846.

Vesic, A. S., & Clough, G. W. (1968). Behavior of granular materials under high stresses. *Journal of Soil Mechanics & Foundations Div*. https://trid.trb.org/View/126933

Watanabe, Y., Lenoir, N., Otani, J., & Nakai, T. (2012). Displacement in sand under triaxial compression by tracking soil particles on X-ray CT data. *Soils and Foundations*, *52*(2), 312–320. https://doi.org/10.1016/j.sandf.2012.02.008

Wei, J., & El Naggar, M. H. (1998). Experimental study of axial behaviour of tapered piles. *Canadian Geotechnical Journal*, *35*(4), 641–654. https://doi.org/10.1139/t98-033

White, D. (2002). *An investigation into the behaviour of pressed-in piles* [PhD thesis]. University of Cambridge.

White, D., & Bolton, M. (2002). Observing friction fatigue on a jacked pile. *Centrifuge and Constitutive Modelling: Two Extremes*, 347–354.

White, D., & Bolton, M. (2004). Displacement and strain paths during plane-strain model pile installation in sand. *Géotechnique*, *54*(6), 375–397. https://doi.org/10.1680/geot.2004.54.6.375

White, D. J., & Lehane, B. M. (2004). Friction fatigue on displacement piles in sand. *Géotechnique*, *54*(10), 645–658. https://doi.org/10.1680/geot.2004.54.10.645

White, D. J., Take, W. A., & Bolton, M. D. (2003). Soil deformation measurement using particle image velocimetry (PIV) and photogrammetry. *Géotechnique*, *53*(7), 619–631. https://doi.org/10.1680/geot.2003.53.7.619

White, D., & Take, W. (2002). *GeoPIV: particle image velocimetry (PIV) software for use in geotechnical testing. University of Cambridge Department of Engineering, Cambridge*. UK. Technical Report CUED/D-SOILS/TR322.

Wiesenthal, P., & Henke, S. (2025). Concept on plug development in jacked open-ended piles in clay considering total stresses. *Acta Geotechnica*, *20*(3), 1019–1033. https://doi.org/10.1007/s11440-024-02455-0

Xiao, J., & Zhao, X. (2019). Performance of a pile foundation in soft soil. *Proceedings of the Institution of Civil Engineers - Geotechnical Engineering*, *172*(2), 189–201. https://doi.org/10.1680/jgeen.17.00172

Yamamuro, J. A., Bopp, P. A., & Lade, P. V. (1996). One-Dimensional Compression of Sands at High Pressures. *Journal of Geotechnical Engineering*, *122*(2), 147–154. https://doi.org/10.1061/(ASCE)0733-9410(1996)122:2(147)

Yang, Z. X., Gao, Y. Y., Jardine, R. J., Guo, W. B., & Wang, D. (2020). Large Deformation Finite-Element Simulation of Displacement-Pile Installation Experiments in Sand. *Journal of Geotechnical and Geoenvironmental Engineering*, *146*(6), 04020044. https://doi.org/10.1061/(ASCE)GT.1943-5606.0002271

Yang, Z. X., Jardine, R. J., Zhu, B. T., Foray, P., & Tsuha, C. H. C. (2010). Sand grain crushing and interface shearing during displacement pile installation in sand. *Géotechnique*, *60*(6), 469–482. https://doi.org/10.1680/geot.2010.60.6.469

Yang, Z. X., Jardine, R. J., Zhu, B. T., & Rimoy, S. (2014). Stresses Developed around Displacement Piles Penetration in Sand. *Journal of Geotechnical and Geoenvironmental Engineering*, *140*(3), 04013027. https://doi.org/10.1061/(ASCE)GT.1943-5606.0001022

Yaseen Sharif, Mike Brown, Scott Robinson, Benjamin Cerfontaine, Marius Ottolini, Wouter Sonnema, & Marco Huisman. (2022). Centrifuge testing of silent piling concept using the push-in method. *ISSMGE*. https://doi.org/10.53243/ECPMG2024-107

Yu, K., Wang, L., Duan, Y., Zhang, M., Dong, Y., Jia, W., & Hu, F. (2021). Soil pore characteristics, morphology, and soil hydraulic conductivity following land subsidence

caused by extraction of deep confined groundwater in Xi'an, China: Quantitative analysis based on X-ray micro-computed tomography. *Soil and Tillage Research*, *211*, 105018. https://doi.org/10.1016/j.still.2021.105018

Zarrabi, M., & Eslami, A. (2016). Behavior of Piles under Different Installation Effects by Physical Modeling. *International Journal of Geomechanics*, *16*(5), 04016014. https://doi.org/10.1061/(ASCE)GM.1943-5622.0000643

Zhang, Y. D., Tan, T. S., & Leung, C. F. (2005). Application of particle imaging velocimetry (PIV) in centrifuge testing of uniform clay. *International Journal of Physical Modelling in Geotechnics*, *5*(1), 15–26. https://doi.org/10.1680/ijpmg.2005.050102

Zhuang, P.-Z., & Yu, H.-S. (2018). Size Effects in Cone Penetration Tests in Sand. In W. Wu & H.-S. Yu (Eds.), *Proceedings of China-Europe Conference on Geotechnical Engineering* (pp. 283–287). Springer International Publishing. https://doi.org/10.1007/978-3-319-97112-4_64

Zil'berberg, S. D., & Sherstnev, A. D. (1990). Construction of compaction tapered pile foundations (from the experience of the "Vladspetsstroi" trust). *Soil Mechanics and Foundation Engineering*, *27*(3), 96–101. https://doi.org/10.1007/BF02306664

Appendixes

Appendix A: Details of stress sensor used for this study

Five stress sensors were embedded in the soil mass, and three stress sensors were installed on the wall to measure the stress within the soil and at the soil-wall interface, as discussed in Chapter 5. Additionally, a load sensor was used to measure the axial force. Table A-1 provides detailed specifications of these sensors.

Table A.1: Specifications of Stress and Load Sensors

Sensor Type	Sensor designation	Place of location	Manufacturer reference
Load sensor	F34	Wall head	FN3070
Stress sensor	0A	On the wall	BEC-A-500KP
Stress sensor	0B	On the wall	BEC-A-500KP
Stress sensor	0C	On the wall	BEC-A-500KP
Stress sensor	1B	In the soil mass	BEC-A-200KP
Stress sensor	2B	In the soil mass	BEC-A-200KP
Stress sensor	1C	In the soil mass	BE-5KD
Stress sensor	2C	In the soil mass	BE-5KD
Stress sensor	3C	In the soil mass	BEC-A-200KP

Appendix B: Results of sensors calibration

All soil sensors are calibrated calibrated to verify its accuracy and linearity prior to test. The calibration was performed under controlled conditions, and the output readings were recorded for a range of known input values. The resulting calibration for all sensors are shown in the following figures.

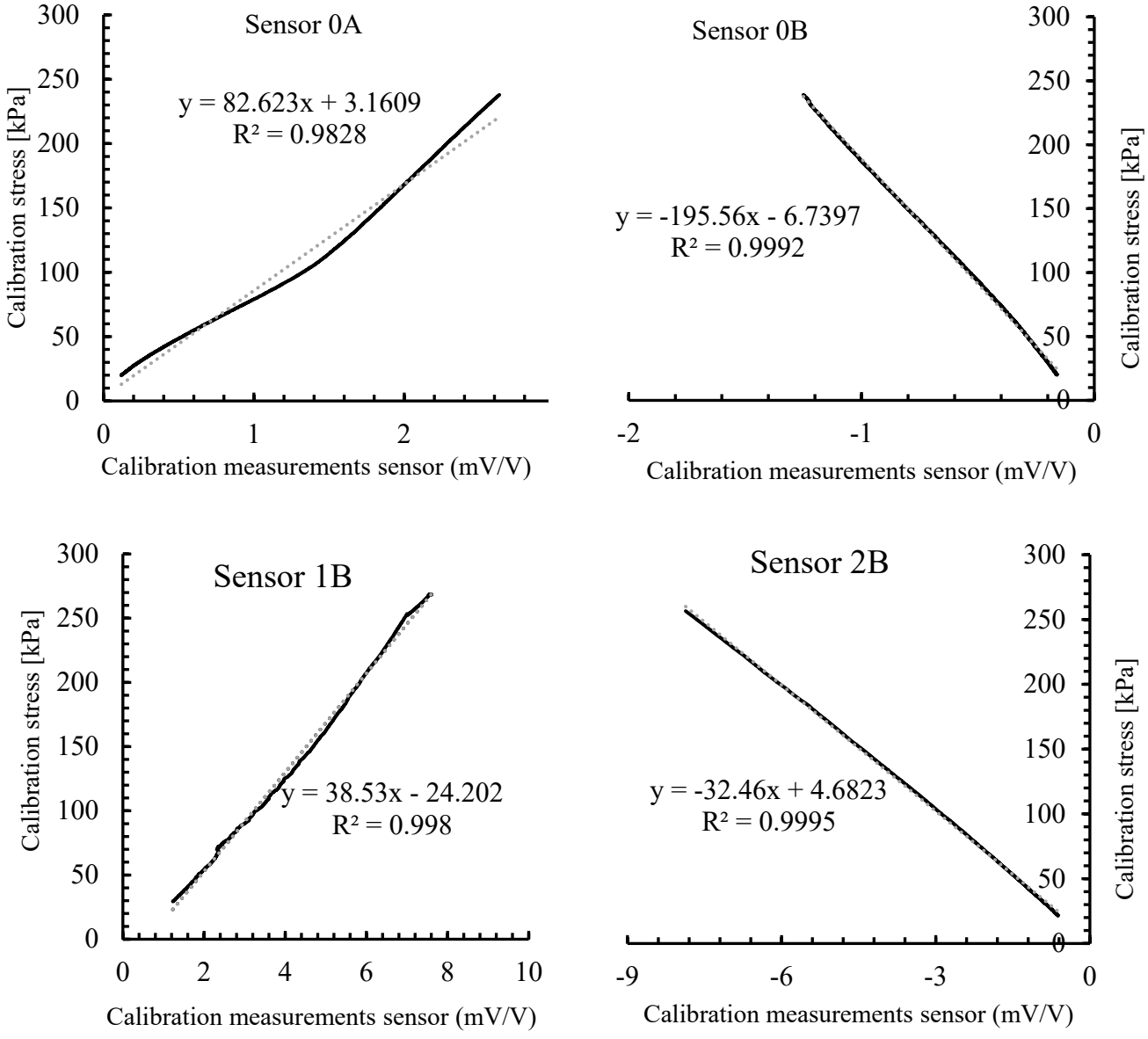

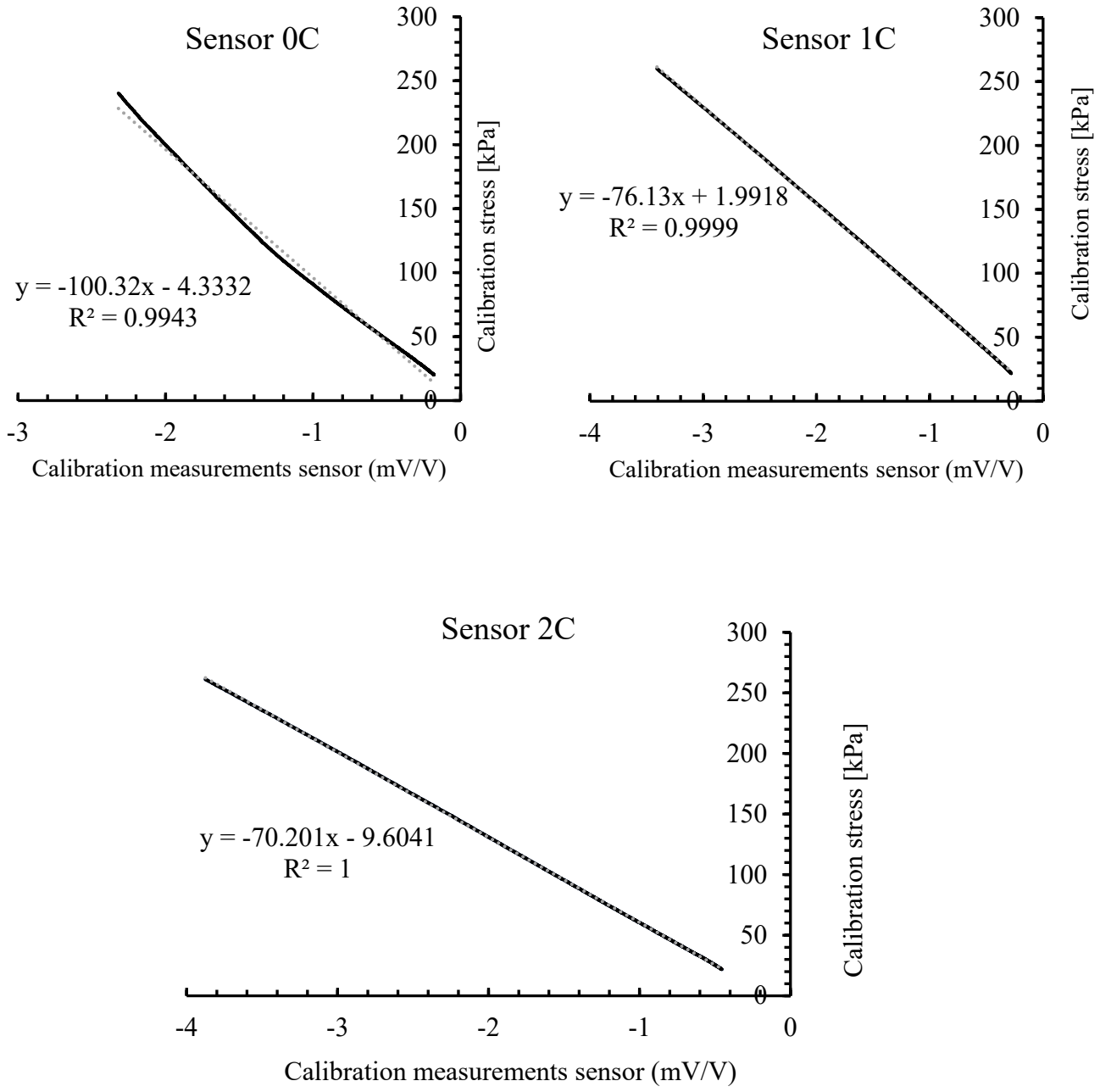

Figure B.1: Calibrations of stress sensors

Appendix C: Image-based analysis using PIV

This appendix provides supplementary information on the image-based analysis conducted using Particle Image Velocimetry (PIV) to capture soil deformation patterns during pile installation. While the results and interpretations are presented in Chapter 6, this section presents the typical image, mesh configuration, and procedural steps used during the analysis. Figure C-1 shows a typical image from S Wall used in the PIV analysis. One can see shallow failure mechanism at the beginning of wall penetration. Figure C-2 shows typical mesh taken during analysis of S Wall using OPTUM G2.

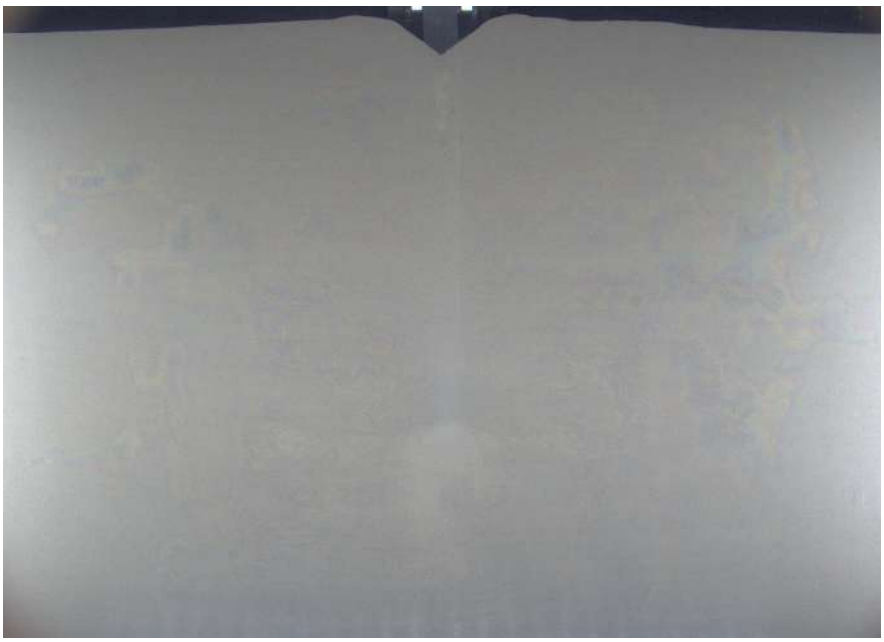

Figure C.1: Typical image taken using camera for PIV analysis

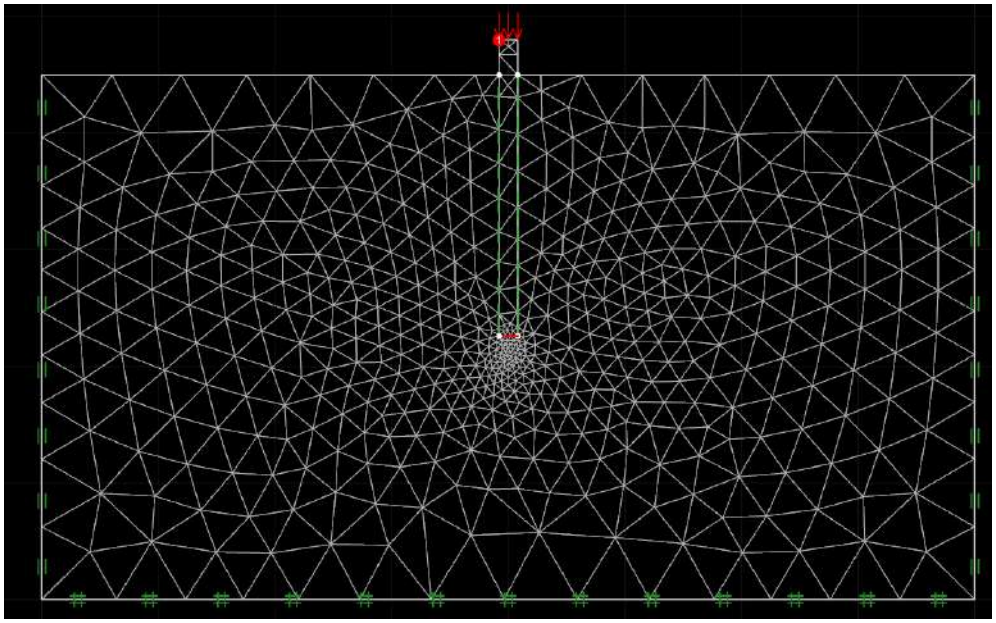

(a)

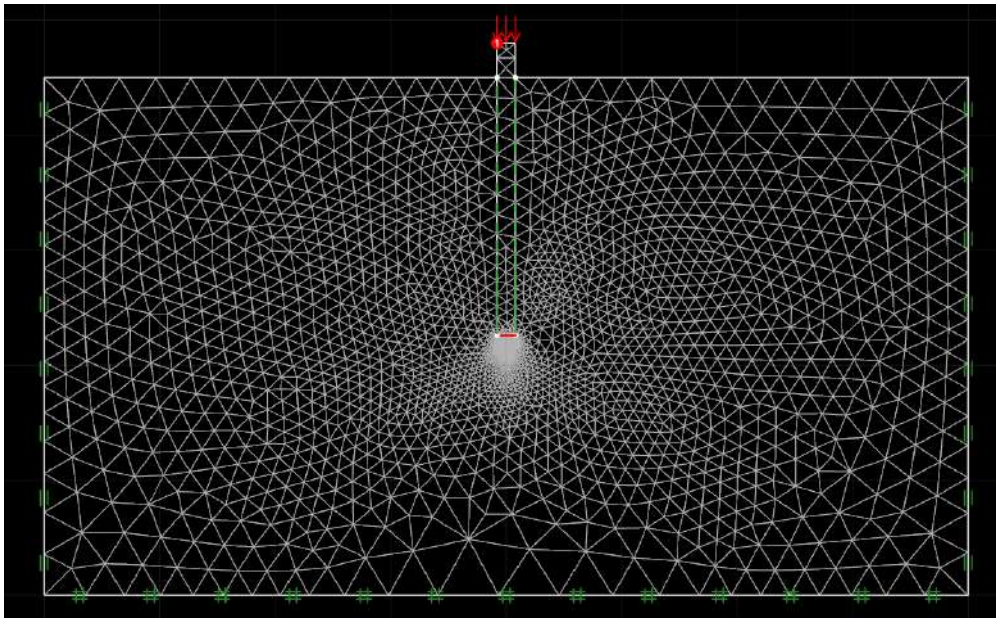

(b)

Figure C.2: Typical mesh taken during analysis of S Wall using OPTUM G2 a) for 1000 elements and b) 4000 elements